QUADRATURE ERROR COMPENSATION AND ITS EFFECTS ON THE PERFORMANCE OF FULLY DECOUPLED MEMS GYROSCOPES

A THESIS SUBMITTED TO
THE GRADUATE SCHOOL OF NATURAL AND APPLIED SCIENCES
OF
MIDDLE EAST TECHNICAL UNIVERSITY

BY

ERDİNÇ TATAR

IN PARTIAL FULFILLMENT OF THE REQUIREMENTS
FOR
THE DEGREE OF MASTER OF SCIENCE
IN
ELECTRICAL AND ELECTRONICS ENGINEERING

SEPTEMBER 2010

Approval of the thesis:

QUADRATURE ERROR COMPENSATION AND ITS EFFECTS ON THE PERFORMANCE OF FULLY DECOUPLED MEMS GYROSCOPES

submitted by **ERDİNÇ TATAR** in partial fulfillment of the requirements for the degree of **Master of Science in Electrical and Electronics Engineering Department, Middle East Technical University** by,

Prof. Dr. Canan Özgen _____
Dean, Graduate School of **Natural and Applied Sciences**

Prof. Dr. İsmet Erkmen _____
Head of Department, **Electrical and Electronics Eng.**

Prof. Dr. Tayfun Akın _____
Supervisor, **Electrical and Electronics Eng. Dept., METU**

Examining Committee Members

Prof. Dr. Cengiz Beşikçi _____
Electrical and Electronics Eng. Dept., METU

Prof. Dr. Tayfun Akın _____
Electrical and Electronics Eng. Dept., METU

Assoc. Prof. Dr. Haluk Külah _____
Electrical and Electronics Eng. Dept., METU

Dr. Said Emre Alper _____
MEMS Center, METU

Dr. Ayşe Pınar Koyaz _____
SAGE, TÜBİTAK

Date: 16.09.2010

I hereby declare that all information in this document has been obtained and presented in accordance with academic rules and ethical conduct. I also declare that, as required by these rules and conduct, I have fully cited and referenced all referenced material and results that are not original to this work.

Name, Surname: Erdinç TATAR

Signature:

ABSTRACT

QUADRATURE ERROR COMPENSATION AND ITS EFFECTS ON THE PERFORMANCE OF FULLY DECOUPLED MEMS GYROSCOPES

Tatar, Erdinç

M.Sc., Department of Electrical and Electronics Engineering

Supervisor: Prof. Dr. Tayfun Akın

September 2010, 150 pages

This thesis, for the first time in the literature, presents the effect of quadrature error compensation on the performance of a fully decoupled MEMS gyroscope and provides experimental data on the sources of quadrature error. Dedicated quadrature error cancellation electrodes operating with only differential DC potentials and generating a force in phase with drive displacement to cancel the quadrature motion in a fully decoupled gyroscope are designed. FEM simulations are used to understand the sources of quadrature error and spring imbalances are found to be the main source of quadrature error. Gyroscopes with intentionally placed spring imperfections are fabricated with SOG based SOI process. SOG process is replaced with SOG based SOI process which provides higher yield and process uniformity. Contact resistance problem is solved during process optimization. As the next stage fully closed loop control modules are designed for drive amplitude control, sense force feedback and quadrature cancellation.

These modules are connected on a printed circuit board (PCB) with vacuum sealed sensor module and tests are performed.

Tests show that the designed circuit with quadrature cancellation operates as expected. Test results illustrate the performance is improved up to 7.8 times for bias instability, up to 10 times for angle random walk (ARW) and up to 800 times for output offset with quadrature cancellation. The actual performance improvement is higher since some sensors cannot be operated without quadrature cancellation and they are not included in performance improvement calculations. With quadrature cancellation the gyroscopes are operated close to their theoretical white noise limits. The best obtained performance is bias instability of 0.39^0/hr and ARW of $0.014^0/\sqrt{}$hr with theoretical ARW limit of $0.012^0/\sqrt{}$hr. The minimum bandwidth is 70Hz but typically varies between 80Hz-100Hz. The gyroscopes have a measured range of $\pm100^0$/sec but at least $\pm150^0$/sec is possible.

The measurements show that gyroscopes having spring imperfections have absolutely higher quadrature error than standard gyroscopes consistent with FEM simulations. So, it is found that spring design is significant to reduce the quadrature error.

To conclude, quadrature error cancellation improves the gyroscope performance up to theoretical ARW limit showing that quadrature error is the major error source of gyroscopes. In the path to sub degree per hour gyroscopes, quadrature error should absolutely be compensated.

Keywords: MEMS Gyroscope, Quadrature Error, Quadrature Error Compensation Techniques, MEMS Fabrication.

ÖZ

OFSET HATASININ GİDERİLMESİ VE BUNUN TAMAMIYLA ETKİLEŞİMSİZ DÖNÜÖLÇER PERFORMANSINA ETKİLERİ

Tatar, Erdinç

Yüksek Lisans, Elektrik ve Elektronik Mühendisliği Bölümü

Tez Yöneticisi: Prof. Dr. Tayfun Akın

Eylül 2010, 150 sayfa

Bu tez literatürde ilk defa ofset hatasının giderilmesinin tamamıyla etkileşimsiz dönüölçer performansına etkisine ve ofset hatasının kaynaklarına dair deneysel veri sunmaktadır. Tamamıyla etkileşimsiz bir dönüölçerde ofset hatasının giderilmesi için sadece diferansiyel DC potansiyellerle çalışan ve sürüş hareketiyle aynı fazda kuvvet üreten özel ofset giderme parmak yapısı tasarlanmıştır. Ofset hatasının kaynaklarını anlamak için dönüölçere bilerek hatalar yerleştirilmiş ve sonlu eleman analizi ile ofset hatasının miktarı hesaplanmıştır. Yaylardaki dengesizlikler ofset hatasının en önemli kaynağı olarak bulunmuş ve bilerek yay hatası yerleştirielen dönüölçerler SOG tabanlı SOI üretim yöntemiyle üretilmiştir. SOG üretim tekniği daha yüksek verimli ve daha düzenli üretim imkanı sunan SOI üretim tekniği ile değiştirilmiştir. Üretim sonrasında oluşan kontak direnci sorunu çözülmüştür. Bir sonraki adımda sürüş genlik kontrol, algılama modu güç geri besleme ve ofset giderme modüllerinden oluşan tamamıyla

kapalı döngü bir sistem tasarlanmıştır. Bu modüller bir baskı devre üzerinde vakum paketlenmiş duyarga modülü ile birleştirilip testler gerçekleştirilmiştir.

Testler ofset giderme özelliği olan devrenin beklendiği gibi çalıştığını göstermiştir. Test sonuçları ofset giderme devresi ile birlikte sabit kayma kararsızlığında 7.8 kata kadar, açısal rasgele kaymasında (ARK) 10 kata kadar ve çıkış ofsetinde 800 kata kadar gelişme olduğunu göstermiştir. Asıl performans artış miktarı daha da fazladır çünkü bazı duyargalar ofset giderme devresi olamadan çalıştırılamamakta ve o duyargalar performans artış hesabına katılmamıştır. Ofset giderme devresi ile duyargalar teorik beyaz gürültü performanslarına yakın çalıştırılmışlardır. En iyi elde edilen sonuç sabit kayma kararsızlığı olarak 0.39^0/saat ve ARK olarak 0.014^0/√saat'tir ve bu duyarga için teorik ARK sınırı 0.012^0/√saat'tir. En düşük çalışma bandı 70Hz ve tipik olarak 80Hz-100Hz arasında değişmektedir. Dönüölçerlerin çalışma aralığı $\pm 100^0$/sn olarak ölçülmüştür fakat en az $\pm 150^0$/sn'ye çıkabilecekleri öngörülmektedir.

Ölçüm sonuçları sonlu eleman analizleri ile tutarlı olarak yaylarında hata olan duyargaların diğer normal duyargalara göre çok daha fazla ofset hatasının olduğunu göstermektedir. Ofset hatasının azaltılması için yay tasarımı önemli olduğu sonucuna varılmıştır.

Sonuç olarak, ofset hatsının giderilmesi dönüölçer performansını teorik beyaz gürültü limitine kadar getirmiştir ve buna dayanarak ofset hatasının 1^0/saatin altına giden performans yolunda dönüölçer için en önemli hata kaynağı olduğu sonucuna varılmıştır. Bu hatann kesinlikle giderilmesi gerekmektedir.

Anahtar kelimeler: MEMS Dönüölçer, Ofset Hatası, Ofset Hatası Giderme Teknikleri, MEMS üretimi.

To my grandmother, Ruba and my family

ACKNOWLEDGEMENTS

First of all I would like to thank my thesis advisor Prof. Dr. Tayfun Akın for his help, guidance and support during my graduate studies. Starting research career in his MEMS group is invaluable for me.

I should not forget to thank Dr. Said Emre Aper for his guidance and friendly attitude during gyroscope discussions. Without his guidance and help, this study could not exist.

Special thanks to M. Mert Torunbalcı, my perfect fabrication partner, for his helps during gyroscope fabrication and endless discussions about life. I would also express my gratitude to Burak Eminoğlu, my perfect readout partner, for his discussions on gyroscope control electronics and his interesting ideas about the world. I would like to thank other inertial sensors group members especially Dr. İlker Ender Ocak for his helps during fabrication and writing of this thesis. Moreover, I would like to thank all members of the METU-MEMS VLSI research group for providing a nice research environment. I am very grateful to METU-MEMS center stuff for their helps during gyroscope fabrication especially Orhan Şevket Akar.

I am very grateful to my fiancée Ruba İzzet for her patience and support during my studies, my brother Fikret Tatar and my sister Şeyma Tatar for their helps throughout my life.

Last but not least, my special thanks go to my parents for their endless support, love and encouragement throughout my whole life.

TABLE OF CONTENTS

LIST OF FIGURES

FIGURES

LIST OF TABLES

TABLES

CHAPTER 1

INTRODUCTION

Every day airbags save lives of people in all around the world during car accidents. The car understands the accident with its smart little sensors, called accelerometers and initiates its airbag to protect passengers and driver. These are all the results of commercialization of MEMS accelerometers in 90s. Since they are small, cheap and can be fabricated in millions these smart sensors can be placed in standard cars. MEMS or Micro Electro Mechanical Systems uses standard IC fabrication techniques to fabricate mechanical systems. The main advantage of MEMS technology is it occupies very little area compared to its conventional counterparts and it can be fabricated thousands on a single wafer which makes it cheaper. MEMS technology started with standard IC fabrication techniques but later developed its own processes for special applications such as plating, molding and wafer bonding [1]. Today commercial MEMS sensors; inkjet heads, pressure and flow sensors, inertial sensors, MOEMS, BioMEMS and RF MEMS find application area in printers, mobile phones, digital cameras, game consoles, blood pressure monitoring, airbags, inertial measurement units and so on. Total revenue of MEMS market in the world is expected to be $6.54 billion by 2010, and annual compound growth rate of 10.7% is expected in the time period 2009-2014, hitting $9.8 billion in 2014 by iSuppli [2]. Inertial sensors namely accelerometers and gyroscopes constitute the 16% of the total revenue in 2007, 70% is dominated by automotive industry [3].

MEMS accelerometers commercialized before MEMS gyroscopes, due to their relatively simple structure. MEMS accelerometer research is kind of a mature research

topic but the research on micromachined gyroscopes is still continuing. Gyroscopes are used for platform stabilization, image stabilization in hand cameras, car roll over detection, ESP in cars and so on. The performance of commercialized MEMS gyroscopes is sufficient for automotive applications, but not sufficient for navigation applications yet. Currently the hot topic is gyrocompassing which requires angle random walk of $0.001^0/\sqrt{hr}$ and bias instability of $0.005^0/hr$ [4]. Gyrocompass refers to the term; a compass that can find true north by using sensitive gyroscopes. Gyrocompasses using ring laser gyros or fiber optic gyros are available but they are bulky and expensive. MEMS gyros can replace these with the advantage of low cost and smaller size.

In the path to the highest gyroscope performance, design considerations not taken into account before comes into play. The error sources that were not taken into account previously plays significant role in the limits. Today gyroscope design came to a limit and extreme care in mechanical design and readout electronics should be paid. The error sources that limit the gyroscope should be well identified. This thesis concentrates on one of the main error sources that limits the gyroscope performance, so called quadrature error. Quadrature error mainly occurs due to fabrication imperfections and defined as the direct coupling of drive motion into detection mode of the gyroscope. This error is the main obstacle in gyroscope performance in its path to sub degree per hour bias instability and ARW. This study for the first time shows the performance enhancement with quadrature error compensation and provides experimental data on the sources of quadrature error in a fully decoupled gyro. A complete closed loop control mechanism containing drive, sense, and quadrature compensation control electronics with special quadrature error cancellation electrodes operating by only DC potentials were designed and verified in the content of this thesis.

The organization of this chapter is as follows, Section 1.1 explains the basic operation principle of vibratory rate gyroscopes and performance parameters that are used to evaluate the performance of the gyroscopes. Section 1.2 gives a brief overview of micromachined gyroscopes within historical order. Then Section 1.3 gives information about the previous gyroscope studies at METU. Section 1.4 provides information about

the gyroscope studied in this wok. Section 1.5 explains the quadrature error and cancellation techniques. Finally Section 1.6 presents the research objectives and thesis organization.

1.1 Operation Principles of Vibratory Rate Gyroscopes and Performance Parameters

The operation of vibratory rate gyroscopes is based on Coriolis force which was found by French Scientist Gaspard-Gustave Coriolis. A detailed description of Coriolis force will be given in Section 2.1. Figure 1.1 shows a conceptual gyroscope structure. For the Coriolis force to act on the gyroscope the gyroscope is vibrated along drive axis either by electrostatic force or by other means. In the presence of an applied rate in the sensitive axis of gyroscope, sense mode of the gyroscope detects Coriolis force. All the MEMS and mechanical gyroscopes' operation is based on Coriolis force, however their mechanical design may be different depending on designer's considerations.

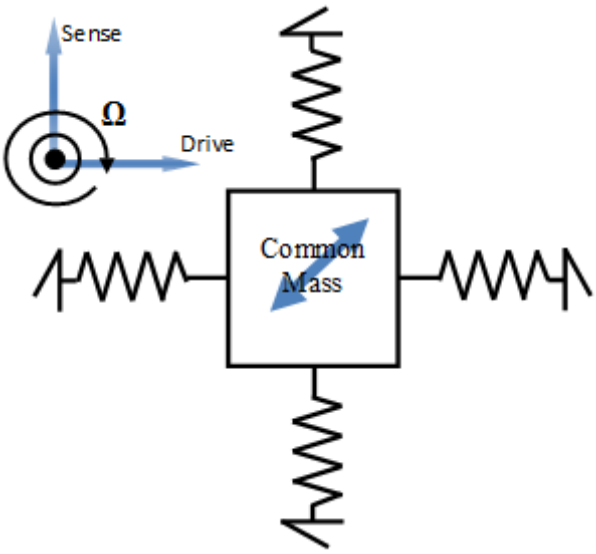

Figure 1.1: A conceptual gyroscope structure

Figure 1.1 is just for showing the conceptual operation of the gyroscope, actual designs are more complicated to decouple the modes, increase sensitivity and suppress unwanted motions but the operation principle is always the same.

There are a number of terms used to evaluate the performance of the gyroscopes [5]. These are summarized below,

Angle Random Walk: Specifies the white noise coming from Brownian motion of the mechanical sensor and thermal noise of electronics. The unit for this error is typically degrees per square root of hour [$^0/\sqrt{hr}$].

Bias Instability (Bias Drift): The random variation in bias as computed over specified finite sample time and averaging time intervals. Characterizes 1/f noise of the gyroscope, unit is degrees per hour [^{0}/hr].

Scale Factor: The ratio of a change in output to a change in the input intended to be measured. The unit is generally milivolts per one degree per one second [mV/^{0}/sec] for gyroscopes. Linearity of scale factor is another parameter that stands for the scale factor change for the applied rates.

Full Scale Range: Maximum angular rate gyroscope can measure reliably. The unit is $\pm^0$/sec.

G-survivability: Max shock that gyroscope can tolerate and continue operation without any damage. The unit is g's.

Bandwidth: The maximum frequency of the input that the gyroscope output can follow without any loss in gain. The 3dB drop frequency in gain is taken as the bandwidth. The unit is Hz.

Depending on the summarized performance parameters, the gyroscopes are classified in three grades [6]. Table 1.1 shows the requirements of these grades.

Table 1.1: Performance requirements of three Grades [6]

Parameter	Rate Grade	Tactical Grade	Inertial Grade
Angle Random Walk, $^0/\sqrt{hr}$	>0.5	0.5-0.05	<0.001
Bias Instability, $^0/hr$	10-1000	0.1-10	<0.01
Scale Factor Accuracy, %	0.1-1	0.01-0.1	<0.001
Full Scale Range, $^0/sec$	50-10000	>500	>400
Max. Shock in 1 msec, g's	10^3	10^3-10^4	10^3
Bandwidth, Hz	>70	~100	~100

1.2 Brief Overview of the Micromachined Gyroscopes

The history of the micromachined gyroscopes started in 1980's with quartz gyroscopes, but they were not compatible with IC fabrication technology [6]. The first silicon micromachined gyroscope was introduced by the Charles Stark Draper Laboratory in 1991 [7] and they improved the process in 1993 [8]. Their improved process was based on silicon on glass (SOG) and dissolved wafer process. The improved gyroscope has angle random walk (ARW) of $0.72^0/\sqrt{hr}$, bias instability of $55^0/hr$, and 60Hz bandwidth. These performance results were the best of those times.

During the early 90s, bulk micromachining and metal electroforming were mostly used to form large masses. Draper's gyros and University of Michigan's electroformed ring gyro which achieved a resolution of $0.5^0/sec$ in 10 Hz bandwidth [9] are examples of these. In mid-90's surface micromachined gyroscopes enabled fabricating the mechanical sensor element and readout on the same chip area. This was achieved with UC Berkeley and Analog Device's iMEMS process [10] showing noise floor of $0.2^0/sec/\sqrt{Hz}$. Analog Devices put into the market commercial gyroscope with this process in 2002 bias instability of $50^0/hr$ and $0.015^0/sec$ resolution [11] and the gyroscope is still in the market. Another approach combining readout and mechanical gyro came from Carnegie Mellon University in 2003, they fabricated the gyro with post CMOS processing with DRIE and achieved noise floor of $0.02^0/sec/\sqrt{Hz}$ at 5Hz bandwidth [12]. The main purpose was increasing the mass to suppress Brownian noise

of the sensor which is advantageous compared to standard surface micromachining. University of California, Irvine on the other hand focused on mechanical design of gyroscopes and fabricated 3-DOF gyroscope system, with noise floor of $0.64^0/\sec\sqrt{Hz}$ over 50Hz bandwidth at atmosphere [13] in 2006. Robert Bosch GmbH, commercial leader in gyroscope market, fabricated a gyroscope for automotive applications with bias instability of $1.35^0/hr$ and ARW of $0.147^0/\sqrt{hr}$ [14] in 2007. Georgia Institute of Technology uses mode matching to achieve sub degree per hour gyroscopes [15]-[16], but they are poor in the sense that bandwidth is limited with a few Hz under match conditions. They fabricate the gyro on SOI wafer and achieved to have bias instability of $0.16^0/hr$ and ARW of $0.003^0/hr$ with automatic CMOS mode matching [16] in 2009. Thales Avionics in 2009 presented a new mode matched gyroscope with ARW of $0.01^0/\sqrt{hr}$ and bias instability of $<0.1^0/hr$ and the controller system is fully digital [17]. The state of the art, highest performance MEMS gyroscope is reported by Draper Laboratories in 2010, the developed gyroscope has bias instability of $0.03^0/hr$ and ARW of $0.002^0/hr$ and the gyroscope is fabricated with Draper Lab's silicon on glass process. The current trend in gyro control is implementing the controller in digital domain rather than analog signal processing [4], [17], [18], [19].

Today most of the gyroscopes are tuning fork type to cancel out the common acceleration. This is because, besides measuring rate the gyroscope sense mode is also sensitive to the acceleration, and the acceleration is canceled by tuning fork structure. In tuning fork two ideal gyroscopes are used but they are displaced in opposite direction and their sense mode output is read differentially. With this way the Coriolis acceleration is doubled whereas the common acceleration term is canceled.

1.3 Previous Gyroscope Studies at METU

The gyroscope studies in METU were initiated in 1998 with surface micromachined gyroscopes fabricated with a standard three layer polysilicon surface micromachining process (MUMPS) [20], [21]. The sensitivity of the sensor was low due to large parasitic capacitances and it was shown with calculations that the sensor can sense angular rates as small as $1.6^0/s$ under vacuum. Figure 1.2 shows the polysilicon

gyroscope developed at METU [21]. The structure was poor in the sense that it had stress related problems due to thin structural layer and large parasitic capacitances due to conducting substrate. Then the process was switched and gyroscopes was fabricated on insulating substrate. Gyroscope prototypes with Dissolved Wafer Silicon Micromachining (DWSM), Nickel Electroforming, Silicon on Insulator Micromachining (SOI MUMPS process) and Silicon on Glass Micromachining (SOG) were fabricated and tested [22]-[24]. Figure 1.3 [25] shows the improved mechanical structure which was designed, fabricated and achieved to have ARW of 35^0/hr/√hz at vacuum and ARW of 90^0/hr/√Hz at atmosphere in 2006 [26]-[27]. A different mechanical structure that keeps the phases of the drive mode oscillating masses exactly opposite was designed and achieved bias instability of 200^0/hr and ARW of 5.47^0/√hr in 2007 [28].

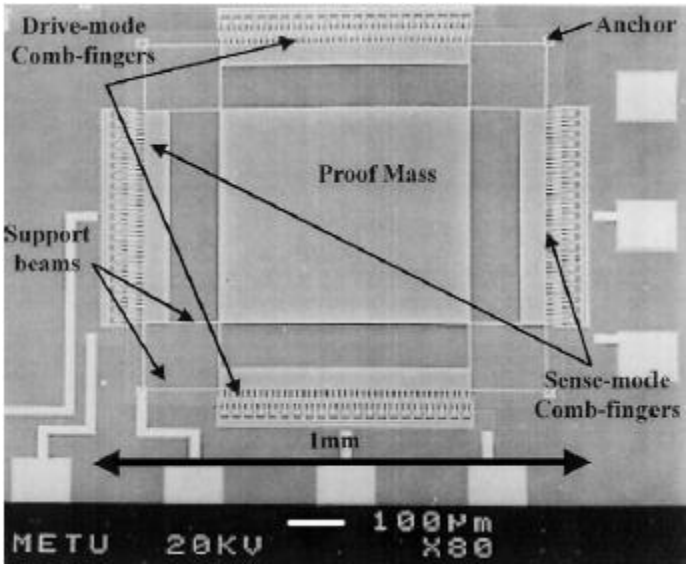

Figure 1.2: Surface micromachined polysilicon decoupled gyroscope developed at METU [21]

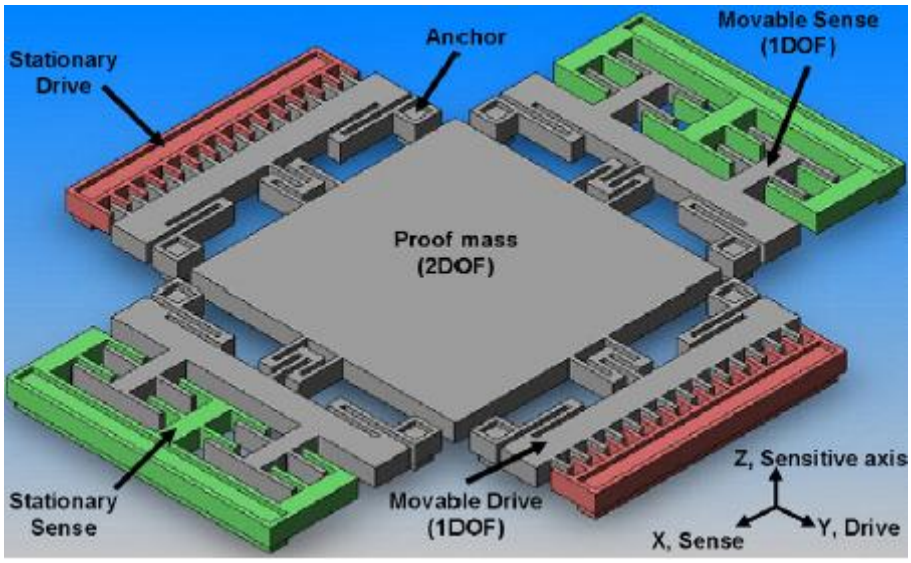

Figure 1.3: Improved decoupled gyroscope [25]

The basics of current readout technique, i.e. converting the output current of the sensor into voltage by transimpedance amplifier (previously unity gain buffer was used), was established in [29] and gyroscope performance was increased to bias instability of 14.3^0/hr and ARW of $0.115^0/\sqrt{}$hr. Later a 2 degree of freedom (DoF) sense mode gyroscope designed and fabricated to achieve wide bandwidth without sacrificing mechanical and electrical sensitivity achieving bandwidth of 1kHz, bias instability of 131^0/hr and angular random walk of $1.15^0/\sqrt{}$hr in 2009 [30]. With fully decoupled gyroscope structure bias instability of 2.99^0/hr and $0.03^0/\sqrt{}$hr reported in 2009 [31]. That work focused on driving the gyroscope with different signal shapes (sine wave drive and square wave drive) with closed and open loop sense systems.

1.4 Gyroscope Studied in This Thesis

Figure 1.4 shows the improved fully decoupled MEMS gyroscope studied in this research. Different from previous gyroscope studies in METU, the new gyroscope structure contains quadrature cancellation electrodes (Q+ and Q-) for the first time.

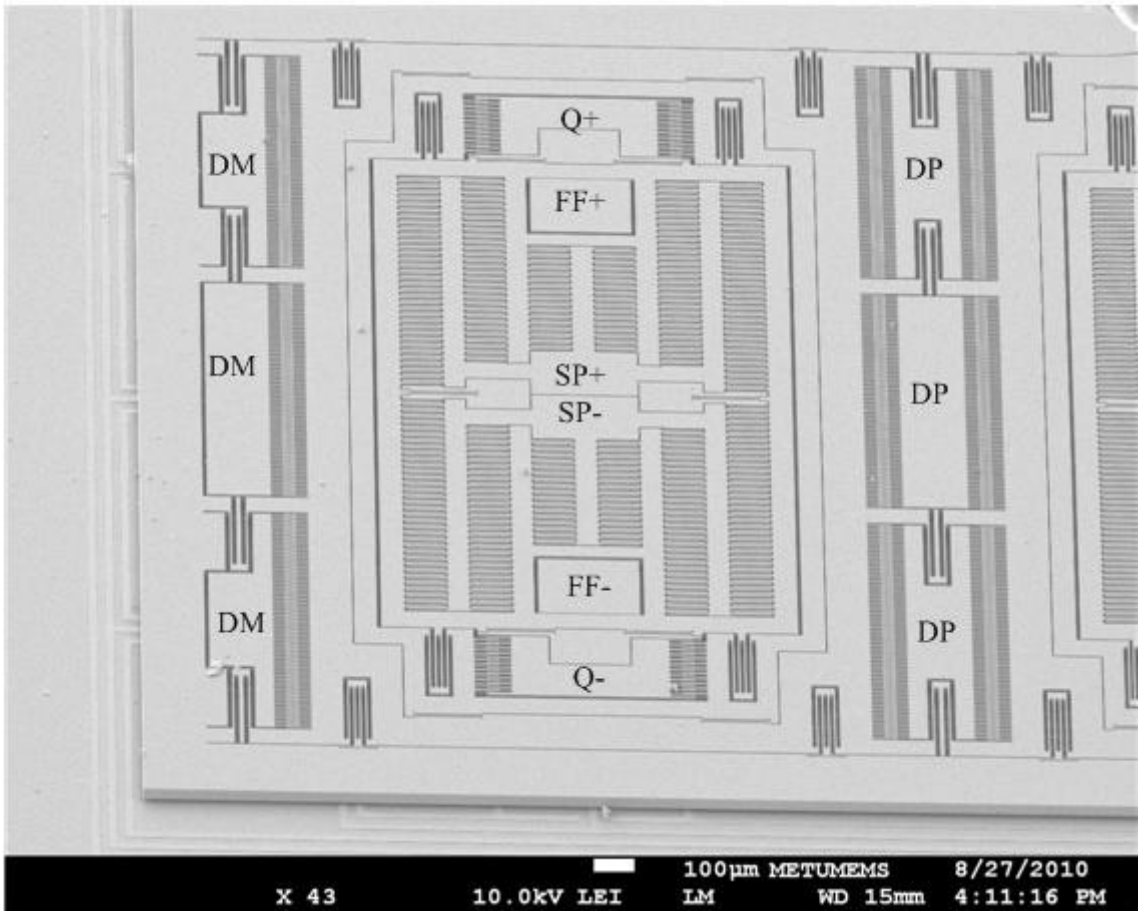

Figure 1.4: SEM image of the fully decoupled gyroscope studied in this work

The gyroscope developed in this study is fabricated with SOG based SOI process. First the glass wafer with recesses and interconnect metallization is formed. Second structural layer is formed on SOI wafer with DRIE different from SOG process, in SOG process [29] device layer was formed after anodic bonding. Processed glass and silicon wafers are anodically bonded and finally handle and oxide layers of the SOI wafer are removed. Oxide layer of the SOI wafer is used as an etch stop layer during structural layer formation and dissolving the handle part of the SOI. The advantage of this process is more stable DRIE process compared to SOG process in which 100µm thick silicon wafer is used and DRIE is performed on bonded glass wafer.

The main research goal of this thesis is to see the effects of quadrature error compensation on gyroscope performance, to apply quadrature cancellation on fully decoupled gyroscope structure and to give experimental data on the sources of

quadrature error. Quadrature error was not previously studied in METU, with fully decoupled gyroscope structure it was minimized at mechanical design stage. In the content of this thesis quadrature cancellation electrodes operating with only DC potentials are designed and placed in the layout. As the next stage closed loop control electronics for drive, sense and quadrature cancellation are designed and implemented. In addition to these, gyroscopes with intentionally placed errors are simulated, designed, fabricated and tested to obtain experimental data on the sources of quadrature error.

1.5 Overview of Quadrature Error and Its Cancellation

Quadrature error can be defined as direct coupling of drive displacement into sense mode of the gyroscope and leads to diagonal elements in spring matrix. It is known till the first gyroscopes in 90s. Different from Coriolis signal which is proportional with the drive velocity, quadrature signal is proportional with drive displacement. There is 90^0 phase difference between Coriolis and quadrature signal; this is useful from electronics point of view in the sense that these two signals can be separated from each other by phase sensitive demodulation.

At the earlier stages of gyro this error was not recognized as a significant error or that was not the parameter limiting the overall performance. But later on late 90s methods to cancel this error were emerged. Phase sensitive demodulation is a technique to suppress this error but the mechanical quadrature signal can be as large as 500^0/sec whereas the rate to be detected is in the order of ^{0}/hr, even a small phase error which is practically inevitable causes offsets at the output. If it was only an offset, then it would not constitute a problem, in that case the offset could be canceled by electronics. The main problem with quadrature error is its stability throughout the time. Since the large quadrature signal (amplitude and phase) changes with time the output offset also varies. There is no choice rather than minimizing or canceling this error to operate the gyroscope at theoretical limits.

The sources of this error are not exactly known but the process imperfections are recognized as the main source [10]. On the design stage every structure is drawn to be perfectly orthogonal to each other but microfabrication tolerances are poor compared to

their dimensions, for example a 4μm beam width cannot be defined better than ±0.1μm tolerance. As a result the fabricated device does not have perfectly orthogonal drive and sense modes. Some portion of the drive displacement couples into sense. Figure 1.5 shows an idea about the ideal and actual gyroscope

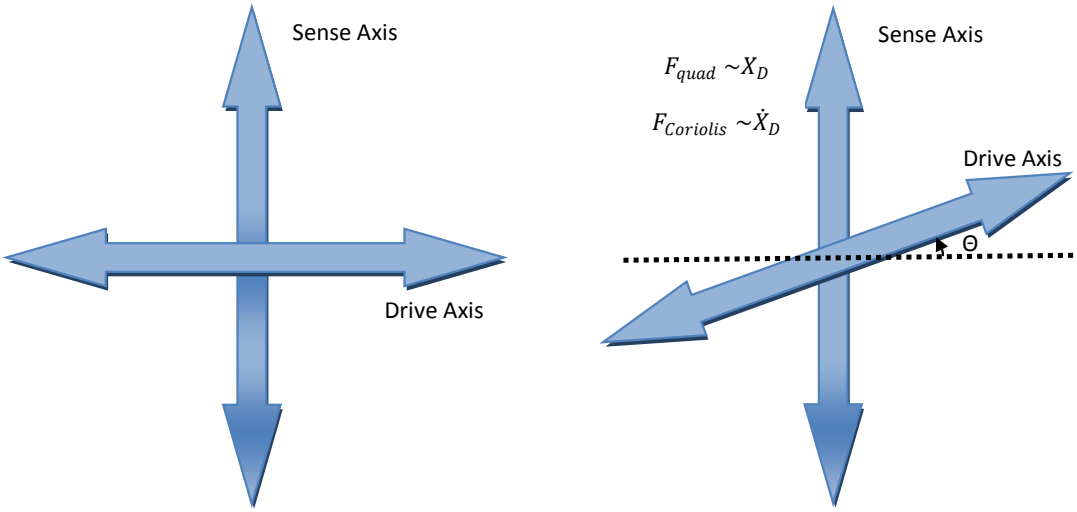

i. ideal gyroscope ii. actual gyroscope

Figure 1.5: Conceptual figures on quadrature error

Different ways developed to suppress this error. These techniques are explained in the next sections.

1.5.1 Mechanical Quadrature Suppression

This approach is shown in Analog Devices' gyro [11]. This technique suppresses mechanical quadrature signal by improving the selectivity of springs with the aid of mechanical levers [32]-[33]. A view of mechanical levers is shown in Figure 1.6. The movable parts of the gyro are suspended through mechanical levers of A and B. Their stiffness is 500 times greater in the undesired axis but they provide minimal longitudinal stress during displacement. Since compensation is made only on mask level, this is a practical solution. The burden on readout electronics is also reduced since no quadrature cancellation circuitry is required. Elimination of quadrature circuit saves die area and smaller gyro chips are possible. Complete elimination of quadrature signal is not possible with this technique; always some portion of quadrature signal is left. This

approach suppresses the quadrature error up to a certain level and the performance is limited with 50^0/hr bias instability.

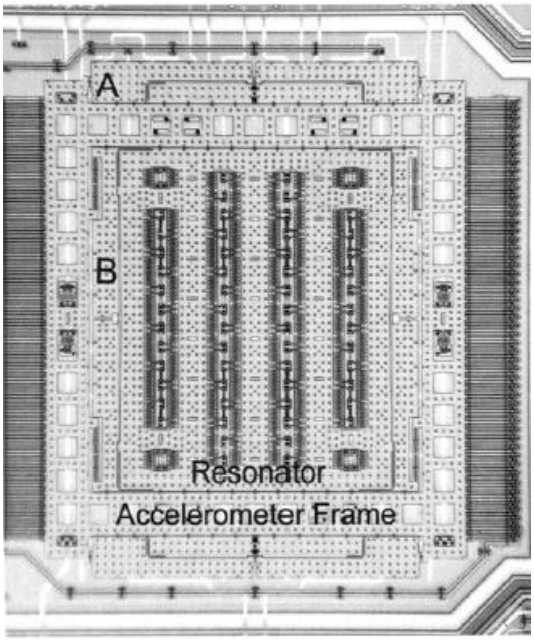

Figure 1.6: Analog Devices' gyro with mechanical levers [11], A and B show the mechanical levers

1.5.2 Electronic Quadrature Suppression

Quadrature signal can also be canceled by injecting a signal with the same amplitude but with opposite phase to the sense channel. Cancellation can be done before converting the current into voltage, in other words charge can be pumped to the preamplifier of the sense channel [34]. For effective quadrature suppression both the amplitude and phase of the feedback signal is important. Amplitude control can be achieved but phase control may bring tight operating conditions on electronics [35]. An algorithm for electronic quadrature cancellation is given in Figure 1.7. The main advantage is it can be applied with any sensor; no modification on sensor design is required. Additional electronics and tight phase control on feedback is the drawback of this technique.

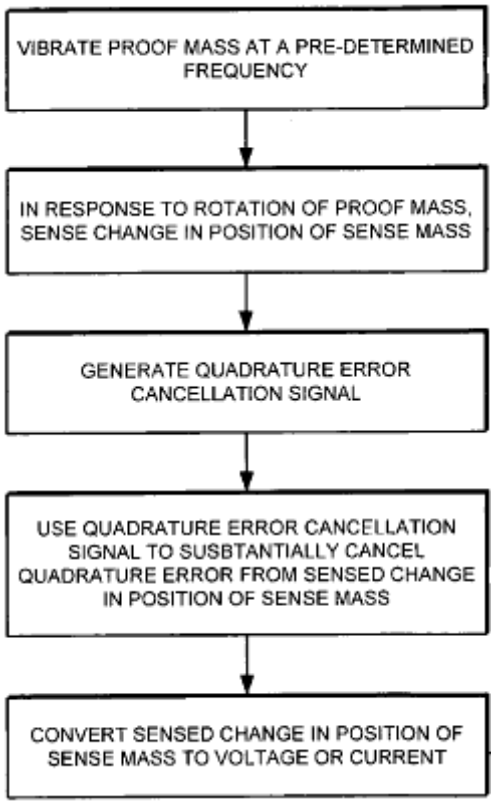

Figure 1.7: Algorithm for electronic quadrature compensation [34]

1.5.3 Electrostatic Quadrature Suppression

Electrostatic quadrature suppression is achieved by applying DC voltages to properly placed electrodes on the gyroscope layout [36], [37], [39]-[42]. Basics of this technique were established by William A. Clark [36]. By only applying DC potentials to specially designed set of fingers and with a proper feedback mechanical quadrature error is eliminated at its source. For coupled gyroscopes that use a single proof mass for both drive and sense modes as in [36], applied DC reorients proof mass so that drive and sense modes are exactly orthogonal to each other. Quadrature cancellation with DC which is implemented by Honeywell can be found in [37]. Photographs of proof mass with respect to applied quadrature potentials can be found in [38]. [39] also shows an example of quadrature cancellation with DC torque voltages.

Among the quadrature suppression methods electrostatic quadrature suppression method is the most effective technique. This is due to its superior characteristics over the other

two methods. Mechanical quadrature suppression can cancel the error up to certain level, i.e. still residual error remains, it improves the performance but for higher performance quadrature signal should completely be removed. Electronic quadrature suppression requires tight phase control on electronics which is impractical. Electrostatic technique completely removes quadrature error. The error is eliminated at its source before coming to sense preamplifier stage. The highest performance gyroscopes reported in the literature makes use of electrostatic quadrature cancellation [16], [17].

Today gyroscope performance came to a limit that the error sources should be well identified to further increase the performance. Quadrature error is one of the main sources and can form the limiting factor for the overall accuracy of the gyroscope system [44].

1.6 Research Objectives and Thesis Organization

The main goal of this study is to experimentally identify the effect of quadrature error cancellation on the performance of fully decoupled MEMS gyroscope and to get experimental data on the sources of quadrature error. The specific objectives of this research can be listed as follows:

1. Design of quadrature cancellation electrodes for the fully decoupled gyroscope structure. The electrodes should be designed such that they will get drive displacement and generate a force in phase with drive displacement by using differential DC voltages to stop the unwanted quadrature motion. Mathematical modeling of drive, sense modes and quadrature error are needed. Modeling of quadrature error should be done using sense mode dynamics since the generated force will be applied on that mode. In order to investigate the sources of quadrature error a technique to characterize the different sources' contribution to quadrature error should be found.
2. Development of a new SOG based SOI gyro process that will solve the problems of previous SOG process. SOG process has problems with device layer formation. Device layer is formed after anodic bonding of silicon and glass

wafers. Due to that overheating problems encountered which results in finger destruction and widening of capacitive gaps. The new developed SOG based SOI process should solve these problems. Contact resistance is another problem, the measured contact resistances are well above the expected values. A process solution to high contact resistances should be found.

3. Design and implementation of a fully closed loop control electronics. The electronics should consist of drive amplitude control module, sense force feedback module and quadrature cancellation module. Closed loop control will result in a robust system that is not affected by environmental changes compared to open loop system. Then the fabricated gyroscopes should be connected with the designed fully closed loop electronics on a PCB to test the thesis' arguments.

The organization of the thesis and the contents of the following chapters are as follows.

Chapter 2 deals with mathematical modeling of vibratory MEMS gyroscopes. After introducing the governing equations and mechanical structure of the gyroscope, the design of quadrature cancellation electrodes for the fully decoupled gyroscope structure and modeling of quadrature error are provided. Finally FEM simulations for modal analysis and modeling the sources of quadrature error are given.

Chapter 3 explains the fully closed loop control electronics design for drive amplitude control, sense force feedback and quadrature cancellation. The design procedures are given and the systems are simulated in SIMULINK design environment. Noise performance of closed loop electronics is provided with mechanical noise of the gyro sensor.

Chapter 4 presents the details of developed SOG based SOI process for gyroscope fabrication and compares it with the SOG process. Problems of SOG process and the solutions obtained with the new SOG based SOI process are explained.

Chapter 5 gives the test results of SOI gyroscopes combined with the fully closed loop designed control electronics. The performances of the gyroscopes with and without

quadrature cancellation are provided to observe the effect of quadrature cancellation. Then experimental data on the sources of quadrature error is given using the gyros with intentionally placed errors. The performances of SOI and SOG gyroscopes are compared to see the effect of quadrature compensation and process improvement.

Finally, Chapter 6 summarizes the conducted work and presents the drawn conclusions. Probable suggested future research topics are also provided.

CHAPTER 2

VIBRATORY GYROSCOPE THEORY, MODELLING AND DESIGN

This chapter provides the vibratory gyroscope theory and introduces the modeling of quadrature error. Section 2.1 describes the Coriolis force with equations then Section 2.2 derives the equations for drive and sense mode dynamics. Section 2.3 explains the gyroscope design. Section 2.4 and 2.5 presents the capacitive actuation and sensing mechanisms, respectively. Section 2.6 provides information about electrostatic spring effect which is used to tune the resonance frequency of the sense mode. Section 2.7 presents the design of quadrature cancellation electrodes for the fully decoupled gyroscope and modeling of quadrature error. Section 2.8 explains the FEM simulations used for modal analysis and quadrature error modeling. Finally Section 2.9 provides the summary of this chapter.

2.1 Description of Coriolis Force

The operation of vibratory gyroscopes is based on Coriolis force. Figure 2.1 shows an inertial frame to visualize Coriolis force. Assuming the object is moving in positive x direction and a rotation of Ω is applied around the z axis, then a fictitious force in the direction that is perpendicular to both the velocity and axis of rotation is exerted on the object.

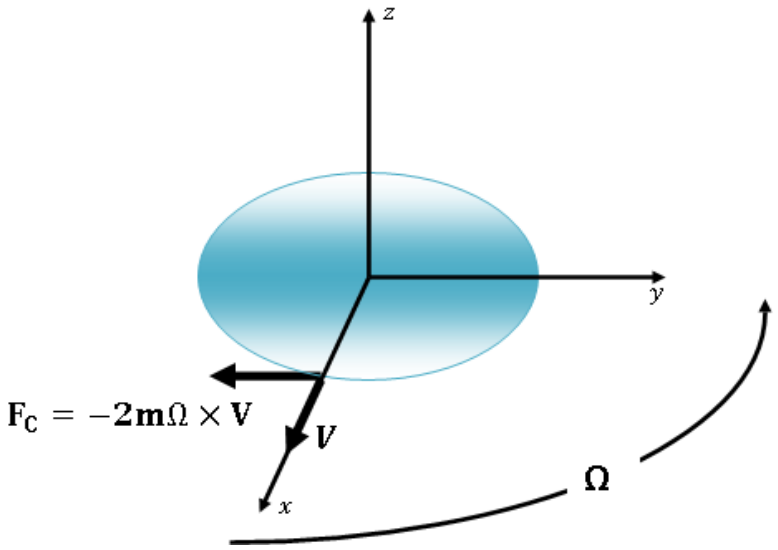

Figure 2.1: Inertial frame showing Coriolis force

The fictitious force is called as Coriolis force and can be expressed as [45]

$$F_C = -2m\Omega \times \dot{X} \qquad 2.1$$

where m is the mass of the object, $\dot{X}$ is the velocity of the object and Ω is the applied rotation rate. Equation 2.1 implies that in order to detect Coriolis force, the mass should have a velocity otherwise Coriolis force is zero. That's why gyroscopes operate under dynamic conditions; there must be a vibrating mass (drive mode of the gyroscope) for the Coriolis force to be exerted.

2.2 Mechanical Model of the Gyroscope

In the mechanical design, the gyroscope can be designed as either coupled or decoupled. In the coupled design, there is only one mass used for drive and sense. In other words while drive motion sense mode also moves and vice versa. However in decoupled design, modes are separated from each other so that while one mode moves the other is not affected. Figure 2.2 and Figure 2.3 shows different gyroscope structures. Figure 2.2 (a) shows a coupled gyroscope, Figure 2.2 (b) decoupled gyroscope and Figure 2.3 fully decoupled gyroscope. In addition to Figure 2.2 and Figure 2.3, different structures can

also be designed. For example drive can be decoupled from proof mass and sense frame [22].

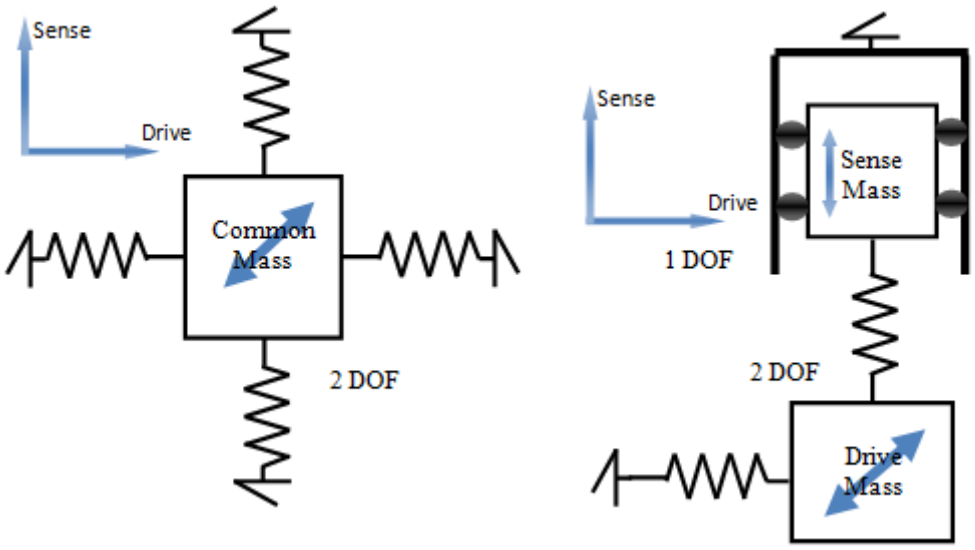

(a) (b)

Figure 2.2: (a) Coupled gyroscope (b) Sense mode decoupled gyroscope

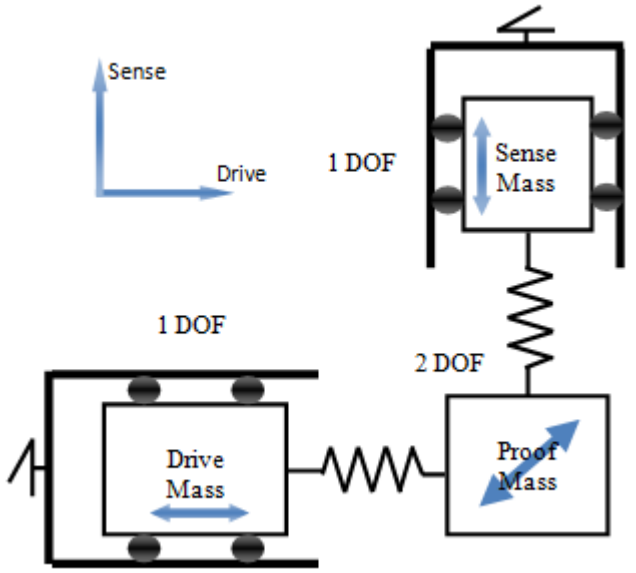

Figure 2.3: A fully decoupled gyroscope structure

The advantage of decoupling is the reduction of crosstalk between drive and sense modes of the gyroscope. This crosstalk is known as quadrature error which is a major

error source in MEMS gyroscopes. This error should be compensated and this study provides a complete work on this topic. For fully decoupled gyroscope design a coupling mass (proof mass) is required, as shown Figure 2.3. Decoupling the modes is achieved through dedicated suspension systems and springs. The drawback of decoupling is the loss in sensitivity to rate. Referring to Figure 2.3, Coriolis force acts on proof mass however the Coriolis acceleration acts both on proof mass and sense mass. As a result the sensitivity to rate is reduced by $\frac{m_{proof\ mass}}{m_{proof\ mass}+m_{sense}}$. Coupled gyroscopes have higher mechanical crosstalk between modes since they are directly connected to each other; as a result their quadrature signal is higher. The advantage is $\frac{m_{proof\ mass}}{m_{proof\ mass}+m_{sense}}$ ratio is unity providing no loss in sensitivity to rate. Cross talk and sensitivity are two important tradeoffs in gyroscope design.

The gyroscope studied in this thesis is fully decoupled similar to Figure 2.3 and Figure 2.4 shows the simplified model of the gyroscope. Basically the gyroscope consists of two gyroscopes driven differentially to cancel out the common acceleration and has three frames. These can be summarized from outer to inner as drive, proof mass and sense frame respectively. Drive and sense frames have 1 degree of freedom (DOF) motion capability however proof mass frame has 2 DOF motion capability. Proof mass frame establishes the Coriolis coupling between drive and sense modes. In response to an applied rate sense modes move differentially like drive mode and the rate is converted into information by differential reading. Note that drive modes have mechanical connection between them, however sense modes are mechanically separated from each other. This will result in two separate sense resonance peaks due to process imperfections as it will be shown in Chapter 5.

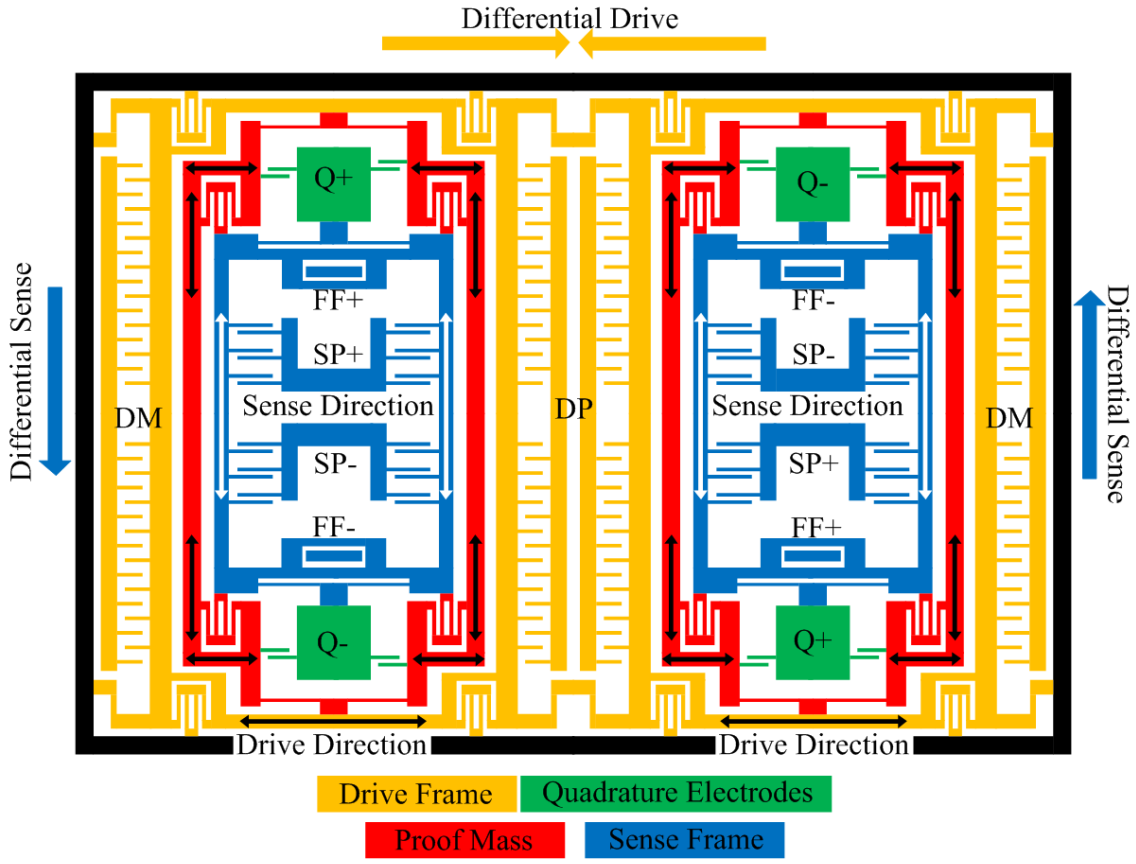

Figure 2.4: Simplified model of the gyroscope studied in this work

2.2.1 Drive Mode Dynamics

The Coriolis force acting on the gyroscope is directly related with drive displacement X. For a stable gyroscope, drive displacement should be well modeled and kept constant over the working period. Drive mode resonator is modeled as a second order spring damper mass system. For a second order system, force displacement relation can be written as,

$$f_D(t) = m_D \frac{\partial^2 x(t)}{\partial t^2} + b_D \frac{\partial x(t)}{\partial t} + k_D x(t) \qquad 2.2$$

In Equation 2.2, f_D is the force acting on drive resonator, m_D is the drive resonator mass, $x(t)$ is the drive displacement, b_D is the damping factor of the drive mode, and k_D is the spring constant of the drive mode. By taking Laplace Transform of equation 2.2 and rearranging the terms,

$$\frac{X_D(s)}{F_D(s)} = \frac{1}{m_D(s^2 + \frac{b_D}{m_D}s + \frac{k_D}{m_D})} \quad 2.3$$

For a second order system with mechanical resonance frequency w_D and quality factor Q_D,

$$w_D^2 = \frac{k_D}{m_D} \quad 2.4$$

$$Q_D = \frac{\sqrt{k_D m_D}}{b_D} \quad 2.5$$

Using equation 2.4 and 2.5, equation 2.3 becomes,

$$\frac{X_D(s)}{F_D(s)} = \frac{1}{m_D(s^2 + \frac{w_D}{Q_D}s + w_D^2)} \quad 2.6$$

Under resonance condition; i.e. $s = jw_D$ when the frequency of the actuation force is equal to the mechanical resonance frequency of the system,

$$\frac{X_D(jw)}{F_D(jw)} = \frac{1}{m_D \frac{w_D^2}{Q_D}} = \frac{1}{j}\frac{Q_D}{k_D} \quad 2.7$$

Equation 2.7 states that at resonance there is 90^0 phase difference between the applied force and displacement. Also increasing quality factor provides a larger displacement for constant applied force. Drive mode of the gyroscope is operated at resonance to get maximum displacement with minimum applied force.

2.2.2 Coriolis Coupling and Sense Mode Dynamics

Sense mode mechanics of the gyroscope is modeled as a second order spring-mass-damper system as drive mode mechanics and Equation 2.2 is also valid for sense mode with subscripts "S". For open loop operation, sense mode is used to detect the induced Coriolis force, no external electrical force is applied as in drive mode. When a rate is applied to the gyroscope in its sensitive axis, a fictitious force perpendicular to drive mode is exerted on drive and proof mass frames since they displace together. Due to mechanical design shown in Figure 2.4, drive frame cannot displace in the sense

direction however the proof mass can. As a result proof mass starts to vibrate with sense mode in the sense direction. It is important here to note that the Coriolis force frequency is equal to the drive mode frequency. The vibration that starts on the sense mode is an amplitude modulated signal at the drive mode resonance frequency.

Force exerted on the sense mode is only due to Coriolis coupling. Consider the most general case when applied angular rate is sinusoidal. Then the relation between sense mode displacement and induced Coriolis force by using Equation 2.1 can be written as,

$$-2m_{PM}\Omega_Z \frac{\partial x(t)}{\partial t} - m_{PM}\frac{\partial \Omega_z(t)}{\partial t}x(t) = m_S \frac{\partial^2 y(t)}{\partial t^2} + b_S \frac{\partial y(t)}{\partial t} + k_S y(t) \qquad 2.8$$

In equation 2.8, m_{PM} stands for the mass of proof mass frame, Ω_Z stands for the applied rate and m_S stands for the total mass of proof mass and sense frames. Assuming sinusoidal drive displacement and sinusoidal rate,

$$x(t) = X_0 cos\ (w_D t) \qquad 2.9$$

$$\Omega_z(t) = \Omega_z cos\ (w_z t) \qquad 2.10$$

where w_z is the frequency of applied rate. Then left hand side of Equation 2.8 can be written as

$$LHS = m_{PM}X_0\Omega_z \left\{ \left(w_D + \frac{w_z}{2}\right) sin(w_D + w_z)\, t + \left(w_D - \frac{w_z}{2}\right) sin(w_D - w_z)\, t \right\} \qquad 2.11$$

Equation 2.11 states that with a time varying angular rate applied to sense mode, sense mode is actually excited by two forces at two frequencies centered around w_D.

Before finding the final response, first find the response to a single complex waveform. Note that the response to a complex waveform is obtained by taking the real part of the complex response.

Assume,

$$LHS = Ae^{jw_t t} \qquad 2.12$$

Then the solution of Equation 2.8 can be found as,

$$Y = \frac{1}{m_s\left[(w_s^2 - w_t^2) + j\frac{w_s}{Q_s}w_t\right]}A \qquad 2.13$$

Rearranging Equation 2.11 in the form of Equation 2.12,

$$LHS = m_{PM}X_0\Omega_z Im\left\{\left(w_D + \frac{w_z}{2}\right)e^{j(w_D+w_z)t} + \left(w_D - \frac{w_z}{2}\right)e^{e^{j(w_D-w_z)t}}\right\} \qquad 2.14$$

Considering the general solution given in Equation 2.13, the solution of Equation 2.8 at two frequencies can be found as

$$Y(w_D + w_z) = \frac{\frac{m_{PM}}{m_S}X_0\Omega_z\left(w_D + \frac{w_z}{2}\right)}{(w_s^2 - (w_D + w_z)^2) + j\frac{w_S}{Q_S}(w_D + w_z)} \qquad 2.15$$

$$Y(w_D - w_z) = \frac{\frac{m_{PM}}{m_S}X_0\Omega_z\left(w_D - \frac{w_z}{2}\right)}{(w_s^2 - (w_D - w_z)^2) + j\frac{w_S}{Q_S}(w_D - w_z)} \qquad 2.16$$

Equations 2.15 and 2.16 can be simplified with certain assumptions. First it is feasible to assume that $w_D \gg w_z$ (drive frequency is much larger than the frequency of rotaion). Sense mode output mainly depends on whether the gyroscope is operating under match or mismatch conditions.

For match condition $w_D \cong w_S$

$$Y(w_D + w_z) + Y(w_D - w_z) \cong \frac{2X_0\Omega_z Q_S}{jw_D}\frac{m_{PM}}{m_S} \qquad 2.17$$

As seen in Equation 2.17, sense mode displacement is amplified by the quality factor. Sensitivity of the gyroscope is significantly improved at match condition, noting that gyroscope is operated under vacuum conditions; i.e. quality factor is in the order of few thousands. For constant rate $w_z = 0$, denominator of equations 2.15 and 2.16 becomes,

$$Den. \cong 2w_D\Delta w + j\frac{w_S w_D}{Q_S} \qquad 2.18$$

where Δw is the frequency difference between drive and sense resonance frequencies.

Under matched condition

$$\frac{f_S}{Q_S} \gg 2\Delta f \tag{2.19}$$

With typical values of $f_S = 13kHz, Q_S = 3000$, Δf should be smaller than 0.2Hz. For matched operation, Δf is named as response bandwidth and under match conditions it is very small. Matching the frequencies with 0.1Hz-0.2Hz sensitivity requires additional care and called as mode matching. In the literature there are specific studies for mode matching [46]. These types of gyroscopes generally have bandwidths less than a few hertz and target the gyro compassing application.

The second case is the mismatch mode which requires

$$2\Delta f \gg \frac{f_S}{Q_S} \tag{2.20}$$

Then sense displacement can be found as,

$$Y(w_D + w_Z) + Y(w_D - w_Z) = \frac{X_0 \Omega}{\Delta w} \frac{m_{PM}}{m_S} \tag{2.21}$$

Under mismatch conditions sense displacement is lower compared to match conditions since it is not amplified by quality factor. But generally this mode is preferred. This is because under mismatch conditions gyroscope is more stable and have a wide bandwidth. For the typical values stated for Equation 2.19, 20Hz separation is enough to operate gyroscope under mismatch conditions. The gyroscope studied in the scope of this thesis was designed to operate in mismatch mode for a wide bandwidth and stable operation. At the design stage sense mode resonance frequency is set to 1.5kHz-2kHz higher than drive resonance frequency. During operation, with electrostatic spring effect (will be explained in the following chapters), the frequency split is reduced to 200-500Hz.

2.3 Design of Fully Decoupled MEMS Gyroscope and Model Parameters

There are several parameters to be considered at the design stage of MEMS gyroscopes. Drive and sense resonance frequencies are one of the important parameters. In order to get rid of environmental noise and vibrations the resonance frequencies of drive and sense modes are set between 10kHz-20kHz. Spring design and mass estimation come into play at this point. Spring design, mass and damping factor estimation are discussed in the following sections.

2.3.1 Spring Design and Spring Constant Estimation

Spring constant and the mass of the system determine the resonance frequency of the gyroscope. Different spring structures used in the drive and sense modes of the gyroscope. Springs providing high linearity are preferred in the drive mode since it moves in the order of μm and drive mode springs occupy larger area compared to springs of the sense mode. Sense mode displacement is in the order of angstroms and the spring behavior is linear in that range. So springs occupying less area are preferred in the sense mode. A detailed analysis on spring design and spring constant estimation can be found in [22].

2.3.2 Mass and Damping Factor Estimation

Total mass of the system can be found by using the basic expression;

$$m = dV \tag{2.22}$$

where d is the density and V is the volume. Density of the structure material is specified by the manufacturer and volume can be found by the known methods. Then total mass is found simply by multiplying those numbers.

Damping factor estimation is difficult since there are many parameters to consider like the viscosity of air at different pressures. Damping factor of the gyroscope is obtained by electrical resonance tests after vacuum packaging.

2.4 Actuation Using Parallel Plate Capacitor

The fully decoupled gyroscope studied in this thesis is a capacitive sensor. For actuation and detection capacitors are used in which electrostatic forces come into play. It is important to note that electrostatic forces always pull the capacitor plates towards each other. In actual operation pulling less can act as pushing. Figure 2.5 shows a typical parallel plate capacitor to explain the capacitive force generation.

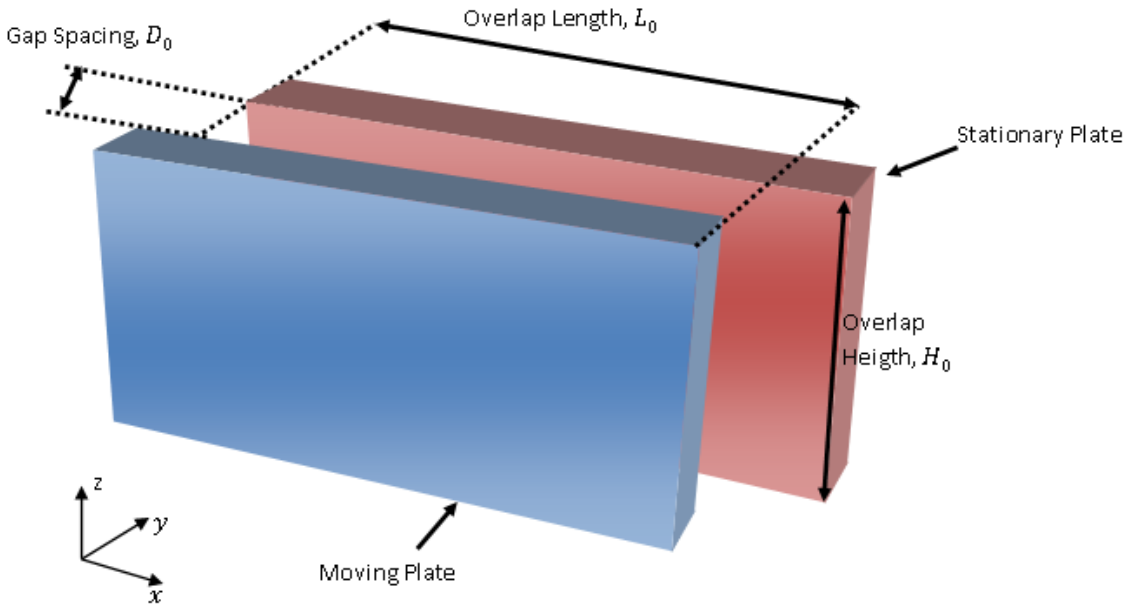

Figure 2.5: Parallel plate capacitor

Assuming the moving plate moves in positive x, y, and z directions. The parallel plate capacitor in Figure 2.5 can be expressed as,

$$C = \alpha\varepsilon_0 \frac{L(x)H(z)}{D(y)} \tag{2.23}$$

$$L(x) = L_0 + x \tag{2.24}$$

$$D(y) = D_0 - y \tag{2.25}$$

$$H(z) = H_0 + z \tag{2.26}$$

In equation 2.23, α is the correction factor for fringing fields and ε_0 is the permittivity of free space. The energy stored in a capacitor is expressed as,

$$E = \frac{1}{2}CV^2 \tag{2.27}$$

where V is the potential difference between capacitor plates. Force acing on the capacitor plates can be found by taking the partial derivative of stored energy in the desired direction as in Equation 2.28 - 2.30.

$$F_x = \frac{\partial E}{\partial x} = \frac{1}{2}\alpha\varepsilon_0\frac{H_0}{D_0}V^2 \tag{2.28}$$

$$F_y = \frac{\partial E}{\partial y} = \frac{1}{2}\alpha\varepsilon_0\frac{H_0 L_0}{(D_0 - y)^2}V^2 \tag{2.29}$$

$$F_z = \frac{\partial E}{\partial z} = \frac{1}{2}\alpha\varepsilon_0\frac{L_0}{D_0}V^2 \tag{2.30}$$

The generated electrostatic force does not depend on position for x and z directions however it has a quadratic position dependence for y direction. This is due to the fact that in x and z directions the rate of change of capacitance is constant, however it changes with position in y direction. The force and sensitivity along y direction is higher compared to other directions, but worse linearity is the tradeoff. For small displacements $y \ll D_0$ force expression can be assumed as constant and this is exactly the case for the sense mode of the gyroscopes. The displacement in the sense mode due to applied rate is in the order of angstroms which is much smaller than the gap. Sensitivity is a major concern in the sense mode since it determines the minimum detectable rate. Varying gap type capacitors offering higher sensitivity are used in the sense mode. However for the drive mode, where the major concern is the linearity, varying overlap area capacitors which assure constant force are used.

In Equations 2.28-2.30 besides displacement another parameter to be examined is the applied potential V. All the movable parts in the gyroscope are kept at proof mass potential, while AC excitation signals are applied from fixed parts. So force can be expressed as

$$F_r = \frac{1}{2}\frac{\partial C}{\partial r}(V_{PM} - V_{AC} sin\,(wt))^2 \qquad 2.31$$

where V_{PM} is the applied proof mass potential and V_{AC} is the amplitude of the applied AC signal. Equation 2.31 can be expanded as,

$$F_r = \frac{1}{2}\frac{\partial C}{\partial r}\{V_{PM}^2 - 2V_{PM}V_{AC}\, sin(wt) + (V_{AC} sin(wt))^2\} \qquad 2.32$$

Equation 2.32 can be rearranged to yield

$$F = \tfrac{1}{2}\tfrac{\partial C}{\partial r}\Big\{\underbrace{V_{PM}^2 + \tfrac{V_{AC}^2}{2}}_{\text{DC}} - \underbrace{2V_{PM}V_{AC}\, sin(wt)}_{\text{AC @ } w} + \underbrace{\tfrac{1}{2}V_{AC}^2 cos\,(2wt)}_{\text{AC @ } 2w}\Big\} \qquad 2.33$$

Equation 2.33 has force components at three different frequencies; one at DC, one at frequency w and one at frequency $2w$. The gyroscope is operated at vacuum and can be considered as a high Q bandpass filter with typical quality factors of 40000 to 50000 for the drive mode. The force components at DC and $2w$ are rejected by the sensor element due to filter characteristics. The component at w drives the gyroscope.

Sense fingers consist of varying gap type capacitors. Figure 2.6 shows the conceptual view of varying gap type fingers.

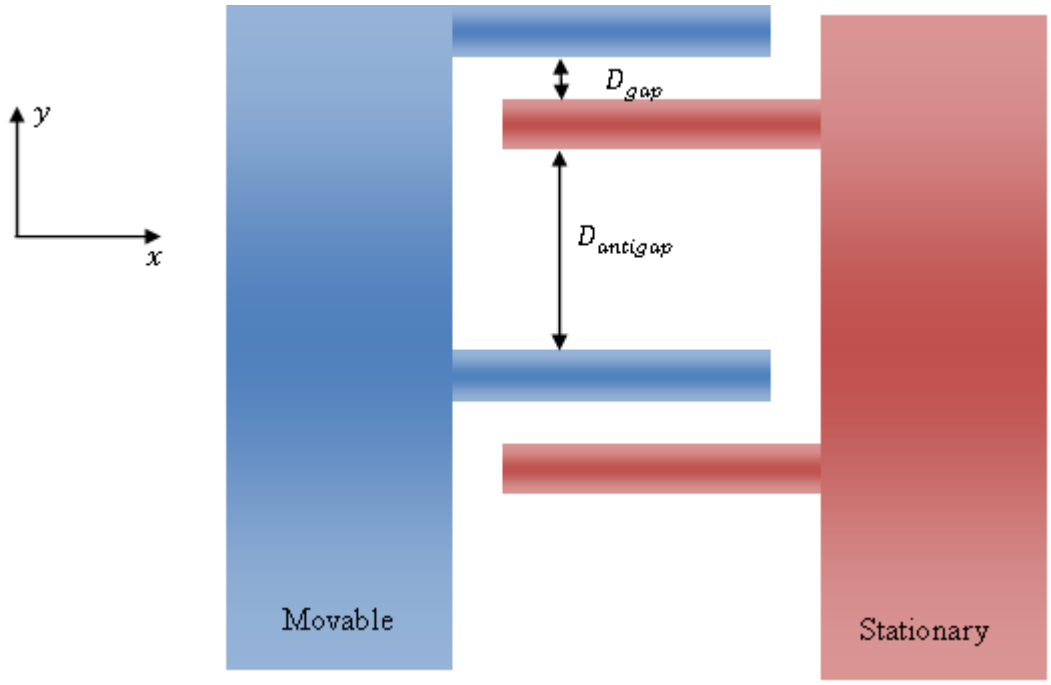

Figure 2.6: Actual view of sense fingers

There are actually two unequal capacitors in Figure 2.6, due to gap and antigap. During operation they change in opposite directions, this should be taken into account during calculations. The net force acting on a single movable finger is found by simple subtraction as follows,

$$F_y = -\frac{1}{2}\alpha\varepsilon_0 H_0 L_0 \left\{\frac{1}{(D_{gap}-y)^2} - \frac{1}{(D_{antigap}-y)^2}\right\} V^2 \qquad 2.34$$

It is straightforward that the calculated forces are only for one capacitor, to find the total force on a set of drive or sense fingers, the expression in Equation 2.34 should be multiplied with the number of fingers.

2.5 Detection Using Parallel Plate Capacitor

Actuation using parallel plate capacitor is examined in section 2.4. The displacement of the drive and sense modes should also be detected and converted into voltage. The signal obtained from drive mode is the carrier signal that is used in all the modulation and demodulation steps in signal processing. The output of the sense signal gives rate

information. Mechanical displacement is first converted into current by capacitors then current is processed by the readout circuitry.

Definition of current through a capacitor,

$$I_{out} = \frac{dQ}{dt} = \frac{d(CV)}{dt} = C\frac{dV}{dt} + V\frac{dC}{dt} \quad 2.35$$

The applied potential $V = V_{PM}$ since the potential between detection electrodes and movable parts is equal to proof mass potential. So the output current can be written as,

$$I_{out} = V_{PM}\frac{dC}{dt} = V_{PM}\frac{\partial C}{\partial X}\frac{\partial X}{\partial t} = V_{PM}\frac{\partial C}{\partial X}jwX(jw) \quad 2.36$$

since drive and sense displacement are sinusoidal. $\frac{\partial C}{\partial x}$ and other parameters are obtained by tests in Equation 2.36.

2.6 Electrostatic Spring Effect

The varying gap type fingers used in the sense mode of the gyroscope inherently have additional features. If the expression given in equation 2.29 is once more differentiated with respect to displacement y the resultant expression has unit in N/m. This indicates the unit of spring constant.

$$\delta k_{electrostatic} = \frac{\partial^2 E}{\partial y^2} = \alpha\varepsilon_0\frac{H_0 L_0}{(D_0 - y)^3}V^2 \quad 2.37$$

The expression in Equation 2.37 indicates that the voltage applied on a varying gap capacitor acts to soften the spring constant in sense direction. For the varying overlap area type fingers such an effect cannot be found, because taking once more derivative of Equations 2.28 and 2.30 results in zero. Electrostatic spring effect is very useful for gyroscope operation. Resonance frequencies of the drive and sense modes are quite critical in operation and mainly defined by springs. Spring widths cannot be defined exactly, for example $\pm$0.2µm tolerance on 4µm spring width affects the resonance frequencies by 10% which is a considerable error. At this point electrostatic spring

effect enables the designer to tune the frequency of sense mode by adjusting the DC potential applied to proof mass. The frequency of sense mode then can be found as

$$w_S = \sqrt{\frac{k_S - \delta k_{electrostatic}}{m_S}} \tag{2.38}$$

Critical point in Equation 2.38 is the pull in voltage when $k_S = \delta k_{electrostatic}$. It is obvious that there is a limit for proof mass voltage it can be increased up to a certain limit. For the differential capacitive configuration used in the sense mode of the gyroscope given in Figure 2.4, pull in voltage can be found by equating sense mode spring constant to electrostatic spring constant. Taking into account both gap and antigap pullin voltage can be found by,

$$\alpha\varepsilon_0 \frac{H_0 L_0}{{D_{gap}}^3} V_{pullin}^2 + \alpha\varepsilon_0 \frac{H_0 L_0}{{D_{antigap}}^3} V_{pullin}^2 = k_S \tag{2.39}$$

$$V_{pullin} = \sqrt{\frac{k_S D_{gap}^3 D_{antigap}^3}{\alpha\varepsilon_0 H_0 L_0 \left(D_{antigap}^3 + D_{gap}^3\right)}} \tag{2.40}$$

2.7 Quadrature Error

Quadrature error which is defined as the direct coupling of drive motion into sense mode, is one of the major error sources in MEMS gyroscopes. Quadrature error occurs due to poor microfabrication tolerances. Different from Coriolis signal which depends on drive mode velocity, quadrature signal directly depends on the drive mode displacement itself. Phase sensitive demodulation may be a choice to eliminate this error, but as it will be shown in Section 3.3.2.1 it is not an efficient technique to suppress this error. Since, the amplitude of quadrature signal may be much larger than amplitude of Coriolis signal and small phase errors result in large errors at the output. Today gyroscope performance came to a limit in which error sources should be well identified and quadrature error is one of the mechanisms limiting performance.

2.7.1 Design of Quadrature Cancellation Electrodes for the Fully Decoupled Gyroscope

Different techniques to cancel quadrature error were explained in Section 1.5 and electrostatic quadrature suppression is found to be the best. Figure 2.7 shows the configuration for electrostatic quadrature suppression [36].

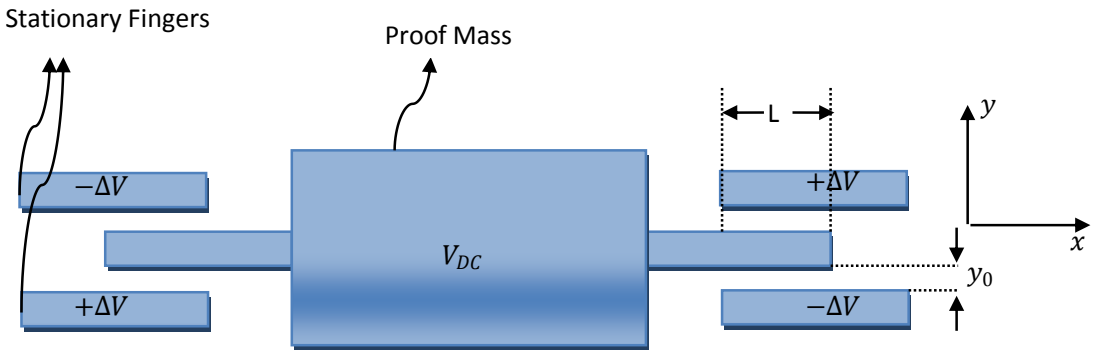

Figure 2.7: Configuration for electrostatic quadrature suppression [36]

Considering Figure 2.7, assume proof mass displaces in the drive direction (positive x direction) for an amount of X, and a small amount of y in positive y direction. Total force acting on proof mass in y direction can be found by;

$$F = \frac{1}{2}\frac{\partial C}{\partial y}V^2 \tag{2.41}$$

There are four capacitors formed between proof mass and stationary fingers in Figure 2.7, so the force acting on the proof mass for a device thickness of h;

$$F = \frac{1}{2}\frac{\varepsilon(L-X)h}{(y_0-y)^2}(V_{DC}+\Delta V)^2 - \frac{1}{2}\frac{\varepsilon(L-X)h}{(y_0+y)^2}(V_{DC}-\Delta V)^2 + \frac{1}{2}\frac{\varepsilon(L+X)h}{(y_0-y)^2}(V_{DC}-\Delta V)^2 - \frac{1}{2}\frac{\varepsilon(L+X)h}{(y_0+y)^2}(V_{DC}+\Delta V)^2 \tag{2.42}$$

For small $y \ll y_0$,

$$F = \frac{1}{2}\frac{\varepsilon(L-X)h}{y_0^2}(V_{DC}+\Delta V)^2 - \frac{1}{2}\frac{\varepsilon(L-X)h}{y_0^2}(V_{DC}-\Delta V)^2 + \frac{1}{2}\frac{\varepsilon(L+X)h}{y_0^2}(V_{DC}-\Delta V)^2 - \frac{1}{2}\frac{\varepsilon(L+X)h}{y_0^2}(V_{DC}+\Delta V)^2 \quad (2.43)$$

Then total force acting on the proof mass in y direction is found as;

$$F = -\frac{4V_{DC}\Delta V\varepsilon Xh}{y_0^2} \quad (2.44)$$

Negative sign indicates that in response to a displacement in positive y direction, the configuration given in Figure 2.7 generates a force to stop this movement. Equation 2.44 includes drive displacement X, which is sinusoidal meaning that a sinusoidal force in the sense axis is generated automatically by only applying DC potentials $\pm\Delta V$. Since the applied force directly includes drive displacement no phase error is introduced to the system. A similar analysis can be found in [36]. The result found in Equation 2.44 is the main principle of electrostatic quadrature cancellation in MEMS gyroscopes. Inherent demodulation due to drive displacement makes it the most effective quadrature cancellation mechanism. Suppression of quadrature error requires a force exactly in phase with drive displacement and configuration given in Figure 2.7 is the ideal and simplest mechanism for that.

The result found in equation 2.44 is for a coupled gyro, i.e. proof mass is directly connected to drive and sense electrodes, while drive motion sense mode also moves without any applied rate. MEMS gyroscope developed at METU is a fully decoupled gyroscope, i.e. ideally no portion of the drive motion couples into sense mode and vice versa. This is established through dedicated suspension systems and three frames, namely; drive, proof mass and, sense frame. Drive and sense frames have only 1 DOF motion capability however proof mass has 2 DOF motion capability. Proof mass frame is used to couple Coriolis force to sense frame. To achieve quadrature cancellation in the fully decoupled gyroscope a new set of quadrature electrodes was designed. Figure 2.8 shows simplified half view of the fully decoupled gyroscope developed at METU.

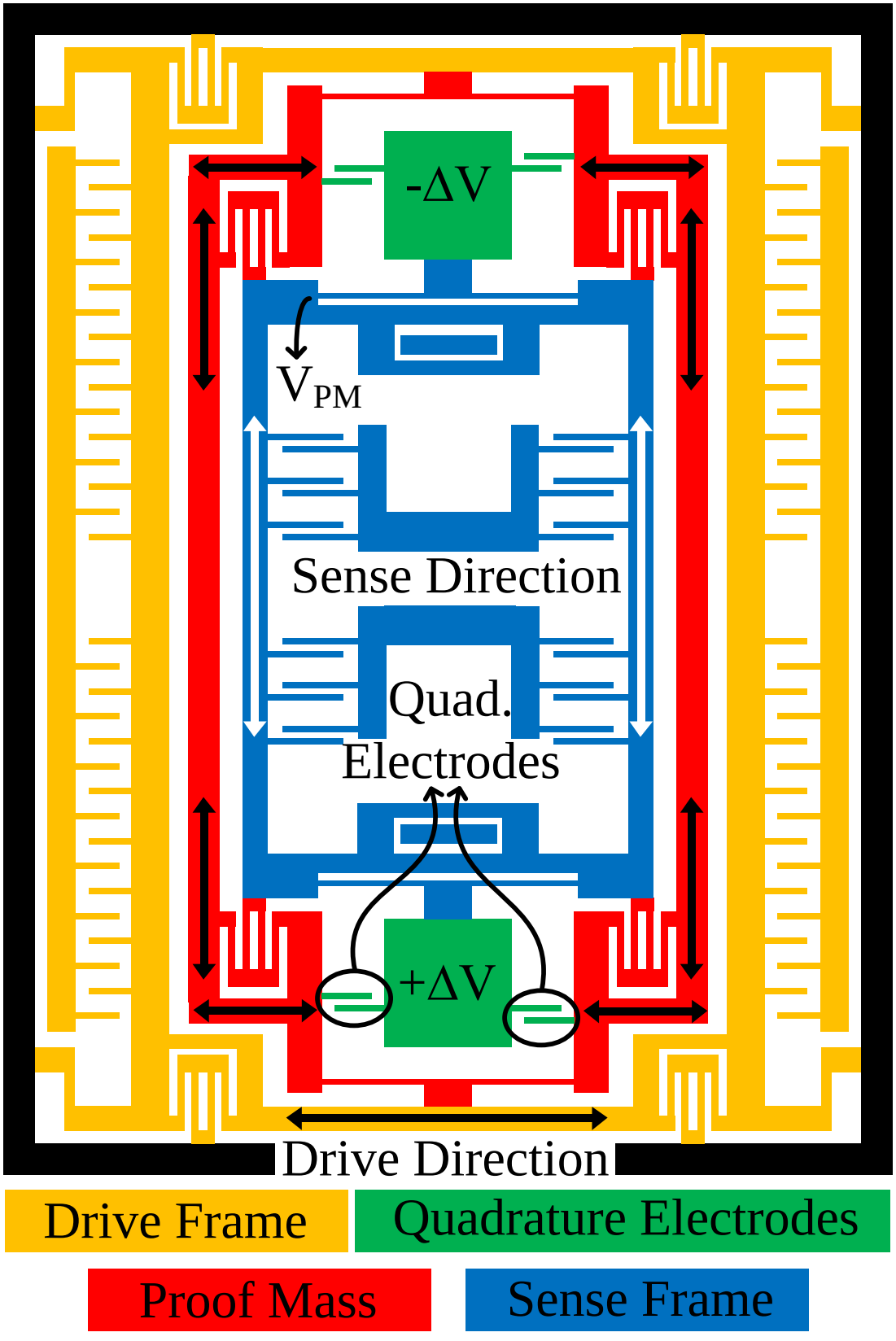

Figure 2.8: Simplified half view of the fully decoupled gyroscope developed at METU

To illustrate the gyroscope better only half of the whole system is shown. The actual system consists of two gyros to cancel out the common acceleration as given in Figure 2.4. Quadrature cancellation electrodes are placed on proof mass, since the quadrature cancellation mechanism needs drive displacement and applies the force in sense direction. Differential quadrature potentials $\pm\Delta V$ applied through two anchors and fingers are placed so that a similar structure to Figure 2.7 is obtained. To better illustrate the adopted mechanism, Figure 2.9 shows the conceptual configuration applied to the fully decoupled gyroscope.

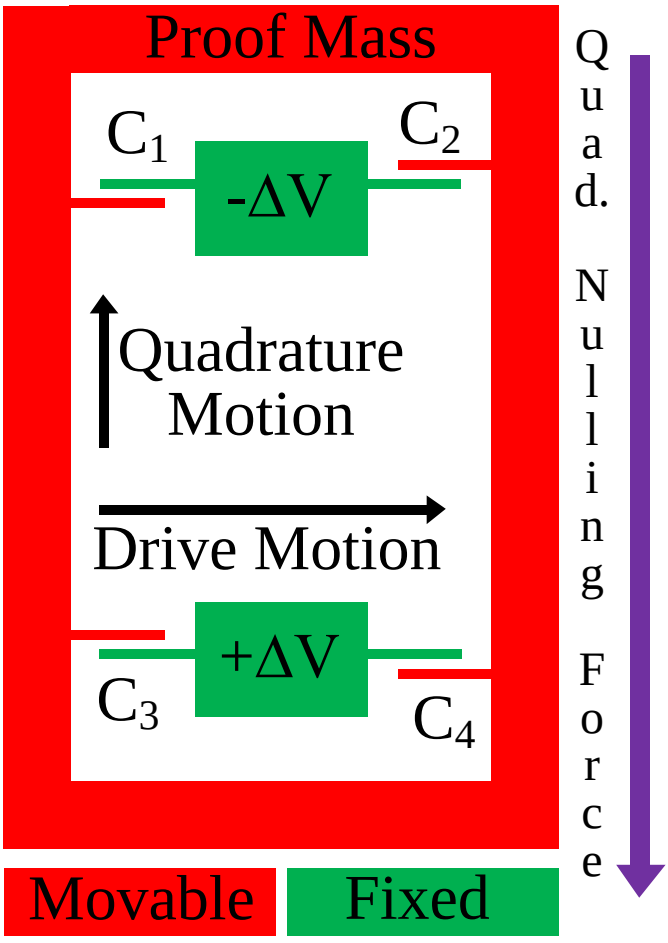

Figure 2.9: Conceptual configuration to cancel quadrature error

Referring to Figure 2.9, for the given drive and sense motion directions, the capacitive configuration generates a force in negative sense (y) direction to stop the unwanted quadrature motion.

When a similar analysis is carried out on the fully decoupled gyroscope given in Figure 2.9, the net force acting on the proof mass and sense frame in response to an unwanted displacement in positive y direction is

$$F = -n\frac{4V_{PM}\Delta V\varepsilon Xh}{y_0^2} \qquad 2.45$$

In equation 2.45 n stands for the number of quadrature electrode finger sets. In Figure 2.8 and Figure 2.9 only one set of quadrature fingers is shown. Normally the fingers are placed as much as possible to cancel maximum amount of quadrature signal.

2.7.2 Modeling the Quadrature Error

The force acting on the sense frame is found in Equation 2.45, but this force acts on sense mode dynamics which should be modeled. Quadrature error occurs in both the proof mass and sense frame, and the force that will cancel the error should act on both of the frames. For that reason in the below analysis by sense mass (m_S) the total mass of proof mass frame and sense frame is meant.

Assuming the quadrature force is acting on sense mode dynamics, force displacement relation is,

$$F_Q = m_S\ddot{y} + b\dot{y} + ky \qquad 2.46$$

Then by taking the Laplace transform of equation 2.46,

$$F_Q(s) = Y(s)(m_S s^2 + bs + k) \qquad 2.47$$

Then,

$$\frac{Y(s)}{F_Q(s)} = \frac{1}{m_S(s^2 + \frac{w_S}{Q_S}s + w_S^2)} \qquad 2.48$$

The operation frequency of the gyroscope is the drive resonance frequency ($s = jw_D$),

$$\frac{Y(jw)}{F_Q(jw)} = \frac{1}{m_S(-w_D^2 + j\frac{w_S w_D}{Q_S} + w_S^2)} \quad 2.49$$

$$\frac{Y(jw)}{F_Q(jw)} = \frac{1}{m_S[\Delta w(w_S + w_D) + j\frac{w_S w_D}{Q_S}]} \quad 2.50$$

Noting that gyroscope operates at vacuum, sense mode quality factor $Q_S \cong 3000$, drive and sense resonance frequencies around 13kHz, mismatch $\Delta w = 200{\sim}500\,Hz$, $\Delta w \gg \frac{w_S}{Q_S}$ and $(w_S + w_D) \cong 2w_D > w_D$. Under these conditions imaginary term in equation 2.50 can be ignored. However it should be known that neglecting the imaginary term brings an amount of phase error.

$$\frac{Y(jw)}{F_Q(jw)} = \frac{1}{m_S(w_S^2 - w_D^2)} = \frac{1}{m_S(\frac{k_S}{m_S} - w_D^2)} \quad 2.51$$

$$\frac{Y(jw)}{F_Q(jw)} = \frac{1}{k_S - m_S w_D^2} \quad 2.52$$

For static conditions second term of the denominator in Equation 2.52 is zero and the equation becomes what we know as $F = kY$, but the situation here is different. It may be easy to see this by a mechanical engineer, however takes some time to understand by an electrical engineer. The second term in the denominator of Equation 2.52 decreases the spring constant of the sense mode and increases the maximum amount of quadrature displacement that can be canceled for constant quadrature force. The maximum amount of quadrature that can be canceled mainly depends on sensor parameters. As the drive and sense resonance frequencies come closer to each other maximum amount of quadrature motion that can be canceled increases. In such a situation quadrature displacement also increases, since sensor sensitivity and coupling from drive to sense mode increases.

To find how much quadrature displacement is canceled Equation 2.45 should be placed inside Equation 2.52. In that situation;

$$n\frac{4V_{PM}\Delta V\varepsilon Xh}{y_0^2} = Y(k_S - m_S w_D^2) \quad 2.53$$

Or more simply,

$$n\frac{4V_{PM}\Delta V\varepsilon Xh}{y_0^2} = Yk_{effective} \quad 2.54$$

The limiting parameter of applied quadrature force in Equation 2.54 is the applied quadrature potential ΔV, in practical implementation it is the output of a PI controller. PI controller is implemented with an OPAMP, in that case maximum quadrature displacement that can be canceled is limited with the OPAMP's supply voltages. To cancel higher quadrature displacements a high voltage OPAMP can be used but the key point in OPAMP selection is the 1/f or flicker noise. Since only DC is applied to quadrature electrodes flicker noise of this potential is important for bias instability and ARW of the gyroscope.

2.8 FEM Simulations

FEM simulations shows the designer higher order effects that he/she didn't take into account while designing the gyro. Coventor, an FEM simulator optimized for MEMS devices was used for FEM simulations in this study.

2.8.1 Modal Analysis

Modal analysis finds and shows the whole resonance frequencies of the analyzed object in all directions. Resonance frequencies of drive and sense modes are quite critical for the operation of gyroscope. For that reason modal simulation is significant in gyroscope design. In addition to drive and sense modes, modal analysis finds the out of plane modes which may deteriorate the performance and difficult to obtain with hand calculation. For safe gyroscope operation the nearest undesired mode should be located at a frequency at least twice the highest desired frequency.

FEM simulations are quite useful but there are points to be taken into account seriously. FEM simulations are based on meshing; i.e. the object is divided into sub divisions and

each division is taken as a single element by the software. Software then combines these single elements and gives the whole result. Choosing the dimensions of single element is the major concern. The smaller the dimensions the more exact solutions are obtained, however decreasing mesh dimensions increases the burden on software and simulation time increases. After some point simulator cannot handle the problem. Optimum mesh dimensions should be found. In order to be sure about the results the simulation should be carried out at least twice with meshing dimensions x and $x/\sqrt{2}$ respectively. Then the results should be checked whether they are consistent with each other or not. If the results converge each other, higher mesh dimension can be used since it results in shorter time. If not mesh dimensions should be divided by √2 and simulation should be repeated again. This algorithm should be followed until two consecutive results converge each other.

The gyroscope studied in this thesis has structural layer thickness of 35µm. While choosing the structural layer thickness, modal simulations run for different structural layer thicknesses. The previously used thickness was 100µm, simulations run with the mask of that process and the results were compared. Table 2.1 provides modal analysis results for different structural layer thicknesses.

Table 2.1: Modal analysis results for different structural layer thicknesses

Thickness	100µm	25µm	30µm	35µm	40µm
Mode	Frequency (Hz)				
1	13759.93066	13430.7041	13459.76758	13488.27148	13515.87305
2	15413.55859	15049.20703	15081.07617	15112.42383	15142.82813
3	22736.19531	21711.03516	22232.39063	22286.54883	22339.23242
4	22736.79492	22178.15039	22232.94727	22287.10938	22339.79492
5	34470.46875	22178.70117	25868.83984	29979.375	34038.87109
6	36198.30859	24341.51367	28827.47656	33198.26172	34241.11328
7	58716.06641	24526.66797	29050.27539	33460.34375	35950.41797
8	58719.47656	27564.16016	32776.59766	34219.92578	37455.03125
9	77686	27580.78516	32791.27734	35928.10156	37758.41406
10	78490.76563	28834.6543	34198.48438	37913.63281	42965.375
		Drive resonance frequencies			
		Sense resonance frequencies			

Modal simulations run for the first 10 modes. First the convergence test was performed with different mesh sizes. In Table 2.1 there are two frequencies for drive and sense modes. This is due to the fact that the gyroscope is differential; i.e. two gyroscopes are connected to assure common acceleration cancellation. Due to differential gyroscopes two modes for drive and sense modes are found one with in phase and one with opposite phase. With differential excitation only one of these modes will be active during operation. As seen in Table 2.1 as structural layer thickness increases the nearest undesired mode goes away from the desired modes. For 25µm thickness, there is one undesired mode in between desired (drive & sense) modes which makes it impractical for gyroscope operation since there is a chance of exciting that mode. Simulation results show that thicker structural layer thickness is better but limit on thickness comes from process conditions. From process point of view, aspect ratio and stable process conditions are important. Taking into account both the process conditions and modal analysis results 35µm was chosen as structural layer thickness. Figure 2.10, Figure 2.11 and Figure 2.12 provides drive, sense and one undesired mode respectively.

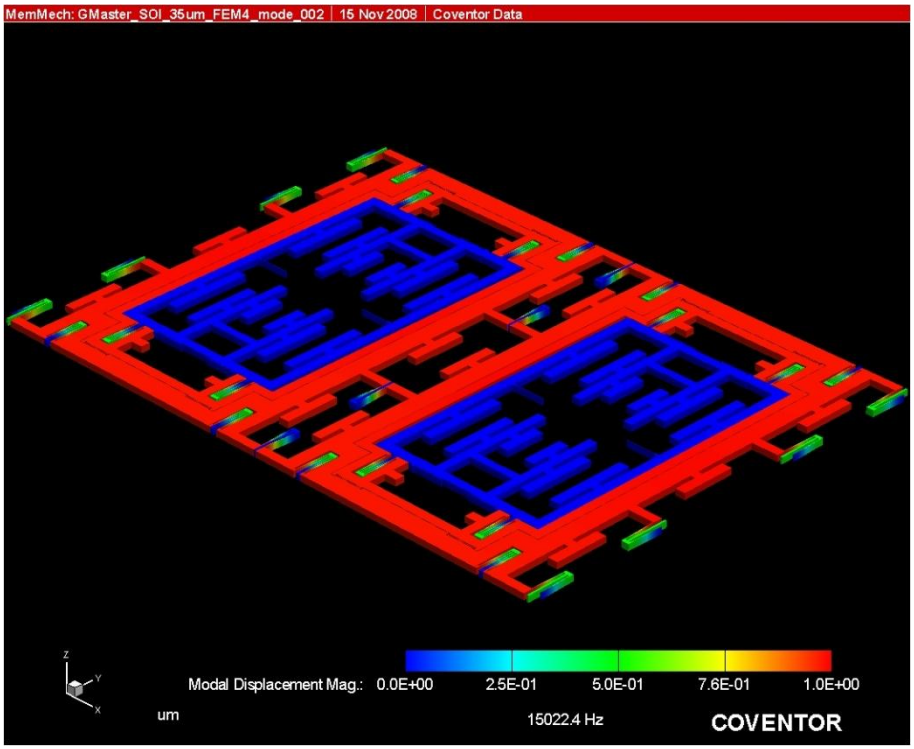

Figure 2.10: Drive mode

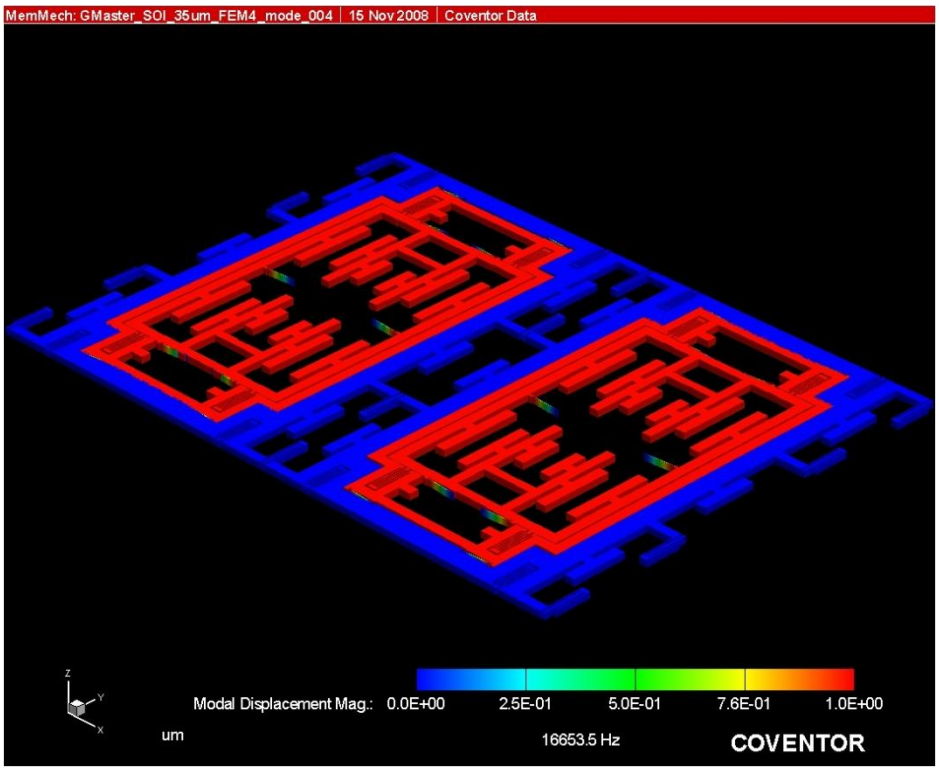

Figure 2.11: Sense mode

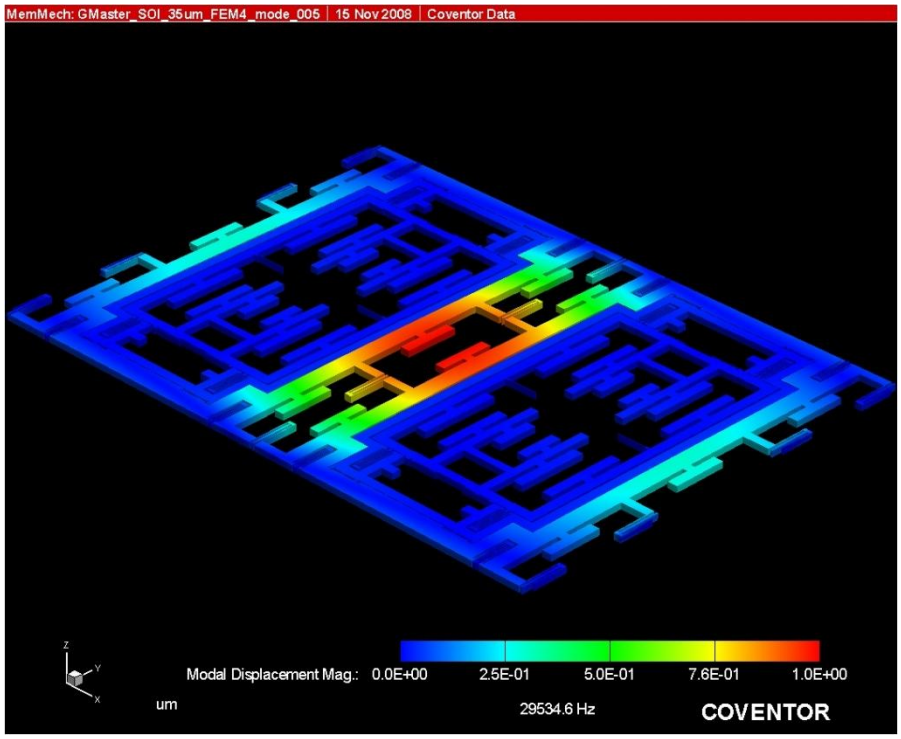

Figure 2.12: Undesired mode at 29.5kHz

Figure 2.12 shows an unwanted mode, as observed the gyroscope has an out of plane mode, behaves strange. To ensure proper operation this mode is kept enough far away from drive and sense modes. Drive resonance frequency is around 15kHz, sense resonance frequency is around 16kHz and the nearest undesired mode is at 29.5kHz. Note that fingers are not placed in modal simulations. If placed with proper mesh dimensions the simulator cannot handle the problem. Equal masses in place of fingers are placed and simulations are run at that condition.

In standard FEM simulations full gyroscope with fingers cannot be simulated as mentioned. Coventor has another simulation module called Architect. In Architect 3-D model is formed by connecting the modules that is present in its own library. However a mask is required for standard FEM simulations in Coventor. Generally mask is ready and it does not take long time to form 3-D model. Forming 3-D model in Architect takes long time since the coordinate of every component is needed, but the simulation time is very short. The Architect can handle the same problem in 30 seconds however the same problem is solved in 5 minutes in standard FEM. The key point behind fast simulation is the components used in Architect. Architect knows whether that component is rigid or not so it does not deal with the rigidity of the component. If not rigid the flexibility in each direction is also known. But in standard FEM, the simulator has to check rigidity and flexibility in all directions. It is possible to simulate the entire gyroscope with drive and sense fingers in Architect. Figure 2.13 shows full gyroscope module with drive and sense fingers.

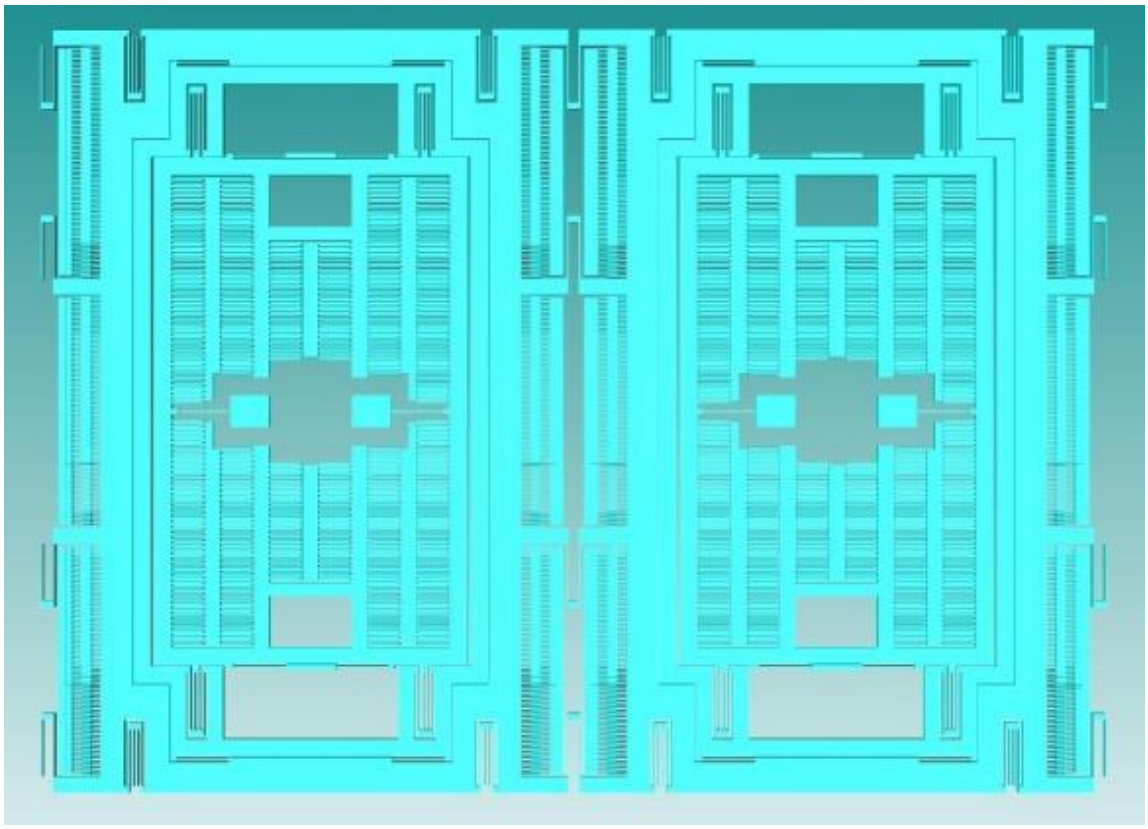

Figure 2.13: Complete gyroscope module formed in Coventor Architect

Problems faced with complete gyroscope module shown in Figure 2.13 and only one gyroscope (half of the view in Figure 2.13) was simulated. The frequency response (modal analysis) results were close to the standard FEM simulations. The advantage is the short simulation time and parameters (spring lengths, spring widths, number of fingers etc…) can be swept easily. As the next step the gyroscope can be combined with electronics and a complete model can be formed in Coventor Architect. Forming the first model takes long time but it may be quite useful if used properly. To show the accuracy of the Architect, Table 2.2 shows the resonance frequencies of drive and sense modes calculated with different sources.

Table 2.2: Comparison of calculated resonance frequencies with different sources

	Architect	**FEM**	**Hand Calculation**
Drive Res. Freq. (Hz)	15371	15022	15468
Sense Res. Freq. (Hz)	16598	16671	16579

Depending on Table 2.2 sense frequencies are very consistent with each other but there is small mismatch for drive frequencies. Assuming that FEM gives the most accurate result there is 2% difference between Architect and FEM. 2% difference is a reliable value for modal simulations. These results verify that Architect is a reliable simulation tool and can be used in gyroscope simulation. Hand calculation results are also close to FEM results, but the deviation is higher compared to Architect results.

2.8.2 FEM Analysis on the Sources of Quadrature Error

It is difficult to find the sources of quadrature error; the known fact is that, it occurs due to direct coupling of drive displacement into sense. The control of spring sidewall angles is known to have major effects on quadrature error with very large aspect ratios [43]. Among the design considerations spring design is the most significant one. To experimentally verify this phenomena gyroscopes with intentionally placed errors and imperfections are designed in the content of the thesis.

The modeling of the errors prior to fabrication was performed with Coventor. The imperfections are placed on the model that is used in Coventor, and FEM tool of the software was used to determine how much quadrature error is introduced with that intentional error.

Depending on literature search the effects of springs, force imbalances and mass imbalances were decided to be examined and the simulations were based on those imperfections. Figure 2.14 shows the actual layout of the half gyroscope and the examined parts of the gyroscope are numbered.

The device layer is formed by DRIE by only a single mask; the starting point was any mass imbalance that occurs during DRIE, nonequal thinning of springs and fingers. The main purpose of the simulations was to determine the amount of error introduced with these sources. At this point it is good to explain how the simulations were performed. The gyroscope cannot be placed in Coventor directly because with drive and sense fingers, the software cannot handle the problem after meshing. To lessen the burden on the software equal masses in the place of fingers were placed as in modal simulations. During the simulation drive mass was displaced by ~5μm differentially similar to actual

operation and sense displacement is monitored. The sense movement for 1^{0}/sec is calculated and the simulated sense displacement was divided to that amount to find rate equivalent error. Figure 2.15 shows the 3-D model used for simulations.

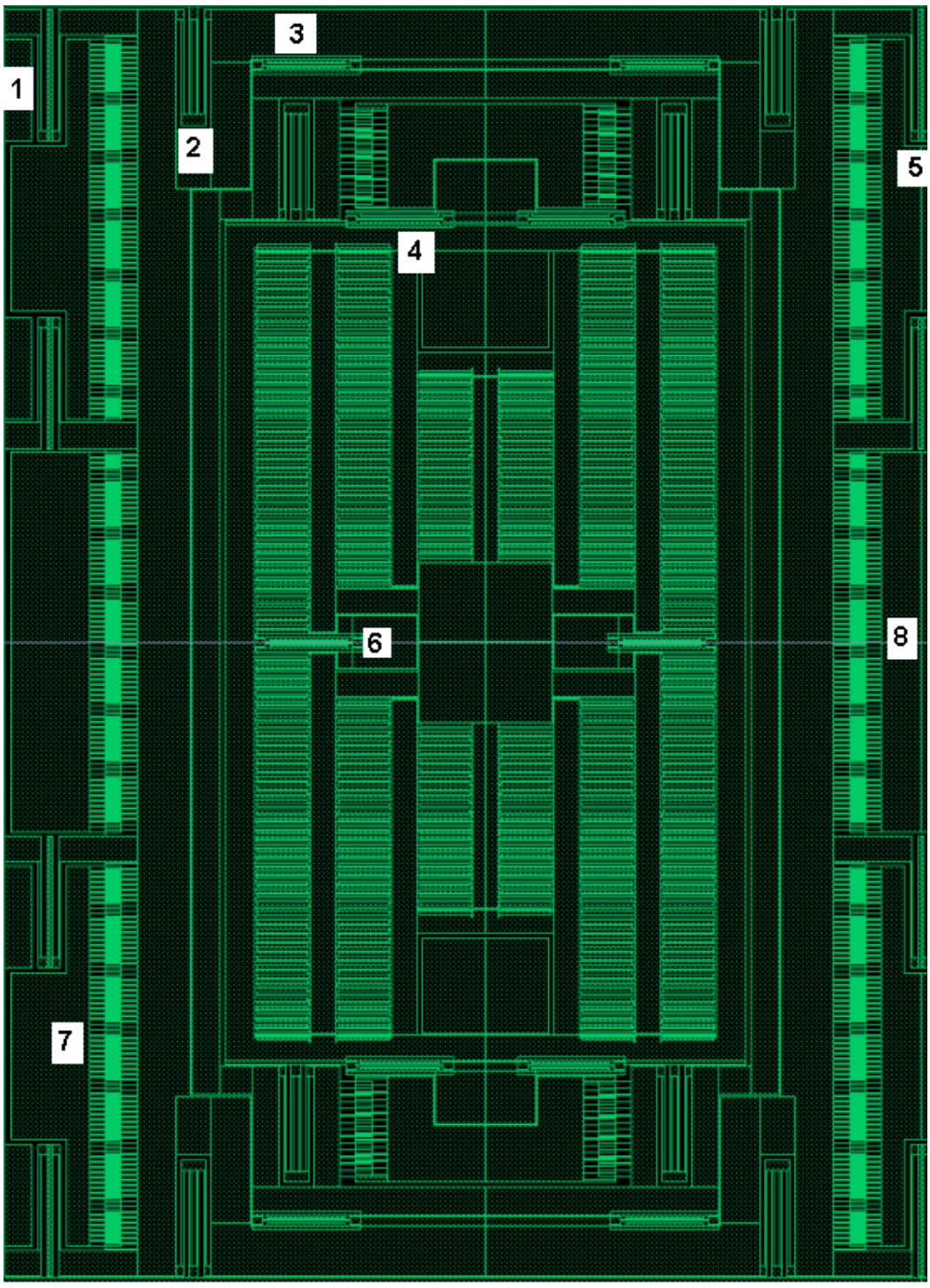

Figure 2.14: Actual layout of the half gyroscope

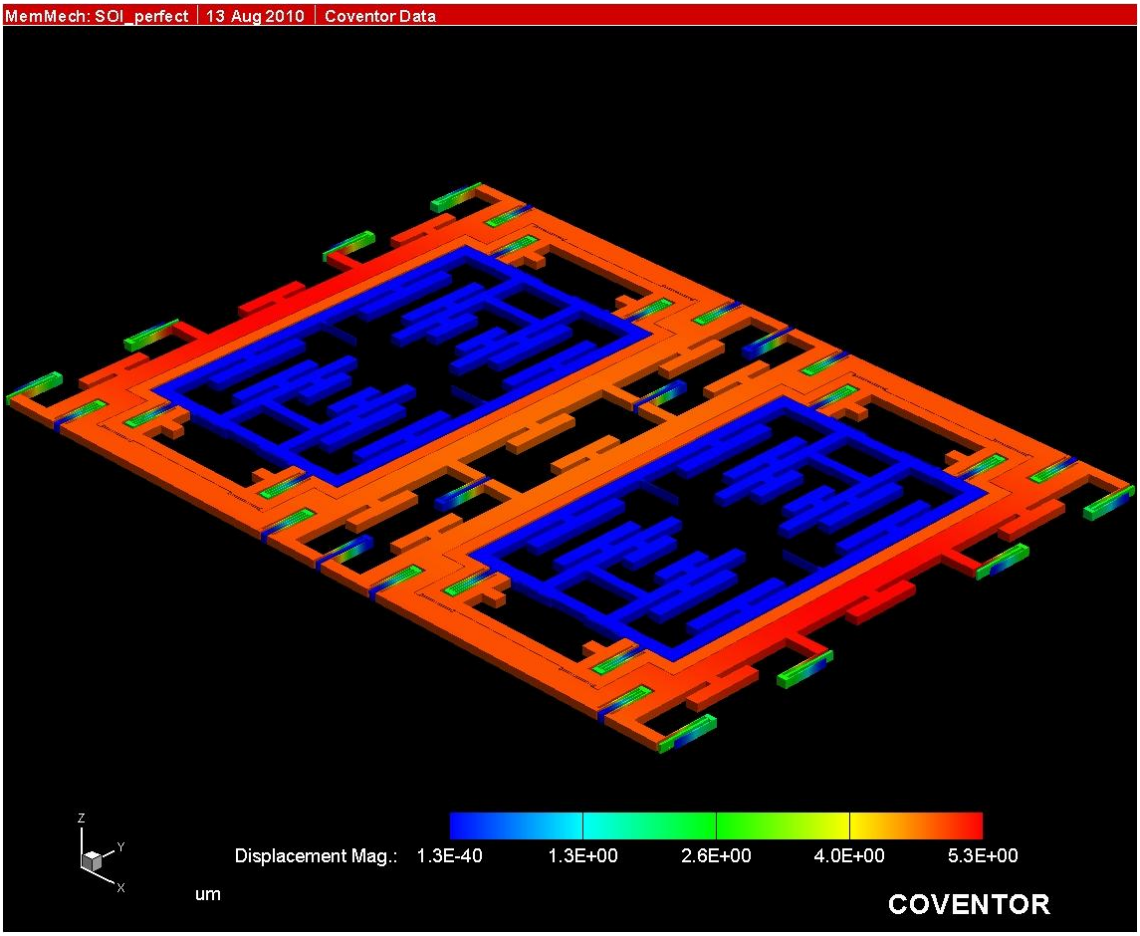

Figure 2.15: 3-D gyroscope model used in Coventor FEM simulations

Figure 2.15, visualizes the simulation procedure. As seen only movable parts are simulated since it is meaningless to include the stationary parts. Equal masses in the place of drive and sense fingers can be observed. Drive mode is displaced by ~5µm and proof mass also displaces with drive, but due to fully decoupled mechanism sense mode does not move. The movement of sense mode is so small that it cannot be visualized; it was extracted with the software's data extraction tool.

The simulations were started with mass imbalances. To observe the mass imbalance some portion of the drive fingers in regions 5 and 8 was deleted. The simulated mass imbalances were 1/500, 1/200 and 1/80 respectively. The calculated errors with these sources were not considerable; they were lower than 10^0/sec. The mass imbalance of 1/80 can be noticed by eye; i.e. this kind of imperfection is not realistic, this does not worth to consider. After simulations it was concluded that mass imbalance does not

cause considerable quadrature error. An electrostatic force imbalance that may occur due to non-equal thinning of drive fingers was also simulated. The gaps of region 7 were modified to 2.2µm and 2.5µm. Table 2.3 summarizes the simulated quadrature error levels for force and mass imbalances. Higher force imbalances might be simulated but they will not be realistic since all the drive fingers are almost etched in the same manner.

Table 2.3: Simulated quadrature error results for electrostatic force and mass imbalances

Quadrature Source	Nominal Value	Errored Value	Quadrature error (^{o}/sec)
Force Imbalance Gap of region 7	2µm	2.2µm	92.7
		2.5µm	178
Mass imbalance	0	1/80	10

The other and the most important sources are the spring imperfections. Most of the simulations were based on spring imperfections. The first imperfection was the misalignment of the springs. What happens if the spring 3 is 1 degree misaligned? 1800^0/sec quadrature! This error is also not realistic, since it can occur only on the mask and will exist on all of the runs (it would be noticed if occurred). Instead of misalignment, nonequal thinning of the springs is more important. For example one spring can be 3.8µm instead of 4µm (layout value) and another spring on the same gyroscope can be 3.9µm. This will probably result in quadrature error. To determine the amount and which spring causes how much error simulations were run. The results are summarized in Table 2.4.

Table 2.4: Simulated quadrature error results for the springs

Spring	1	2	3	4	5	6
Width (µm)	3.5	3.5	3.6/3.8	3.5/3.8	3.5	3.5
Quad. (^{o}/sec)	30	13.2	438/228	9.7/4	43.4	0.1

All of the springs' layout design widths were 4μm and on the simulations the nonideality was introduced via only one spring width change. By observing Table 2.4 the most important spring is found to be spring 3. Spring 3 transmits force from drive to sense and proof mass frames. It can be concluded that the springs which transmits force and motion are quite critical which makes sense. Quadrature error occurs due to coupling of drive motion to sense and any imperfection at the force transmitting springs directly increases quadrature error. Spring 5 causes also error but its error is common for both half gyroscopes which means it can be canceled by differential reading. Spring 4 and 6 are the same with 3 but they do not cause significant error since they do not transmit force from drive to sense. All the springs were simulated. One simulation was performed to see if superposition applies for the error sources. Springs 3 and 5 had errors and the total error was the sum of their individual errors. But key point here is that their error sign was the same, if they had opposite sign errors then they would cancel each other. The spring between 2 and 4 was not simulated because no considerable error was expected. Depending on the results summarized in Table 2.3 and Table 2.4 only the nonideality in spring 3 was drawn into the layout to observe real life results since spring effect was found to have more considerable effects on quadrature error. The imperfection on the layout was introduced at two levels, for some gyroscopes spring 3's width was drawn as 3.6μm and for some 3.8μm instead of design value 4μm. These errored gyros are placed on the layout in similar places with normal gyroscopes in order to compare their quadrature levels and performance.

A change in the widths of the springs was examined; the sidewall angle was not examined since it is not possible to observe it in real life. Sidewall angle cannot be controlled during the process or it is better to say it in this way, a controlled sidewall angle experiment cannot be performed. It can be simulated but experimental verification is not possible.

The main objective is to observe the results of probable process imperfections on quadrature error.

2.9 Summary

This chapter presents the Coriolis force and mechanical model of the gyroscope with their equations. Design of fully decoupled gyroscope is reviewed briefly. Then capacitive detection and actuation mechanisms are explained. Electrostatic spring effect used to fine tune the sense mode resonance frequency is examined. Then design of quadrature cancellation electrodes for the fully decoupled gyroscope is explained and equations to model the quadrature error are derived. Chapter ends with FEM simulations performed to extract the resonance frequencies of drive and sense modes and to model the quadrature error.

CHAPTER 3

READOUT AND CONTROL ELECTRONICS FOR GYROSCOPES

The displacement to be detected in the sense mode of a MEMS gyroscope is in the order of angstroms which require extreme care in the design of electronics. This chapter presents the details of readout and control electronics for MEMS gyroscopes. Section 3.1 explains the preamplifier stage where the output current of the sensor is converted to voltage. Section 3.2 presents how the parameters of the gyroscopes are extracted through tests. Section 3.3 provides the design of closed loop drive and sense mode electronics. Then Section 3.4 explains the quadrature cancellation electronics for the first time in METU. Section 3.5 deals with noise calculations of open loop sense mode, Brownian motion and closed loop sense mode respectively. Section 3.6 gives a brief summary of the chapter.

3.1 Preamplifier Stage

At preamplifier stage output current of the gyroscope is converted into voltage and amplified to a reasonable signal level. Transimpedance amplifier structure is used to convert output current to voltage in gyroscope. Figure 3.1 shows a typical transimpedance amplifier.

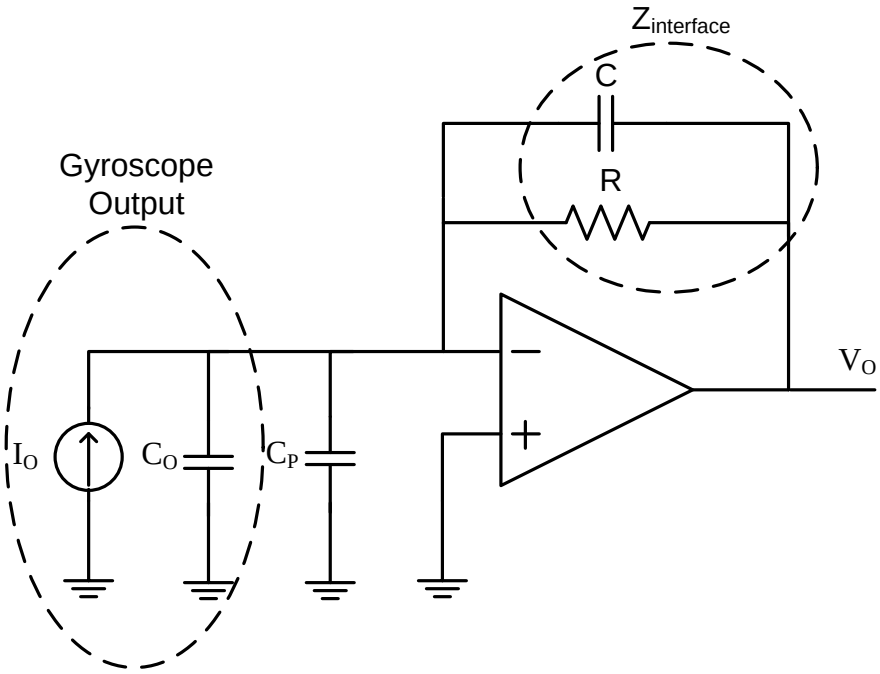

Figure 3.1: A typical transimpedance amplifier

The input output relation of the transimpedance amplifier can be found as,

$$\frac{V_O}{I_O} = \ -Z_{interface} \tag{3.1}$$

$$Z_{interface} = R//\frac{1}{sC} = \frac{R}{sCR+1} \tag{3.2}$$

$$sCR \gg 1 \rightarrow Z_{interface} = \frac{1}{sC}, capacitive\ interface \tag{3.3}$$

$$sCR \ll 1 \rightarrow Z_{interface} = R, resistive\ interface \tag{3.4}$$

As seen in Equations 3.3 and 3.4 depending on the values of C and R transimpedance amplifier can be made either capacitive or resistive. A capacitor should be placed at preamplifier stage of the capacitive sensors to ensure stable operation.

The main advantage of transimpedance amplifier shown in Figure 3.1 is that it is insensitive to parasitic capacitances and contact resistance. Purely transimpedance amplifier is not sufficient for gain and an instrumentation amplifier is used after the preamplifier stage. Capacitive type preamplifier is used in the sense mode preamplifier

stage because if resistive type is used, to satisfy the same gain, noise of that resistor will be higher. Resistive type is preferred in drive mode for system design considerations.

3.2 Obtaining Parameters through Resonance Tests

Model parameters of the gyroscope are needed during design of drive and sense control electronics. Frequency response of the sensor with preamplifier and instrumentation amplifier is obtained by resonance tests. The relation between input and output is found and parameters are extracted based on the found relation.

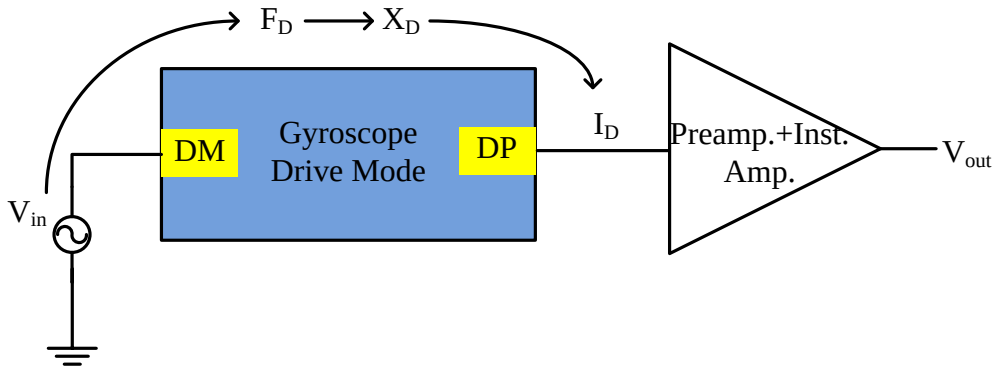

Figure 3.2: Schematic of drive resonance test

During resonance test of the drive mode, gyroscope is actuated from drive motor (DM) electrode, the output current is collected from drive pick (DP) electrode and converted into voltage as shown in Figure 3.2. To explain Figure 3.2 briefly, the applied V_{in} potential is converted into force F_D by capacitive actuation mechanism, the force F_D is converted into displacement X_D by drive mode dynamics and displacement X_D is converted into current I_D by capacitive detection mechanism. Finally the output current I_D is converted into voltage V_{out} by preamplifer and instrumentation amplifier. These conversions can be expressed as,

$$\frac{V_{out}(s)}{V_{in}(s)} = \frac{F_D(s)}{V_{in}(s)} \frac{X_D(s)}{F_D(s)} \frac{I_D(s)}{X_D(s)} \frac{V_{out}(s)}{I_D(s)} \qquad 3.5$$

Combining equations 2.6, 2.28, 2.33, 2.36 and 3.1

$$\frac{V_{out}(s)}{V_{in}(s)} = V_{PM}\frac{\partial C_{DM}}{\partial x}\frac{1}{m_D\left(s^2+\frac{w_D}{Q_D}s+w_D^2\right)}V_{PM}\frac{\partial C_{DP}}{\partial x}sZ_{interface}A_{int.amp.} \quad 3.6$$

$$\frac{V_{out}(s)}{V_{in}(s)} = \frac{V_{PM}^2\frac{\partial C_{DM}}{\partial x}\frac{\partial C_{DP}}{\partial x}sZ_{interface}A_{int.amp.}}{m_D\left(s^2+\frac{w_D}{Q_D}s+w_D^2\right)} \quad 3.7$$

At drive resonance frequency,

$$\frac{V_{out}(s)}{V_{in}(s)} = \frac{1}{m_D}V_{PM}^2\frac{\partial C_{DM}}{\partial x}\frac{\partial C_{DP}}{\partial x}\frac{Q_D}{w_D}Z_{interface}A_{int.amp.} \quad 3.8$$

The mass of the drive mode m_D can be found by hand calculation, proof mass potential V_{PM}, preamplifier gain $Z_{interface}$, and instrumentation amplifier gain $A_{int.amp.}$ are known by the design. Quality factor Q_D and resonance frequency of the drive mode w_D and the gain V_{out}/V_{in} are obtained from resonance tests. There is a known and fixed ratio between the sensitivities of drive motor $\partial C_{DM}/\partial x$ and drive pick $\partial C_{DP}/\partial x$ defined by the design. To sum up all the parameters except the sensitivities of drive motor and drive pick are known. The sensitivities of DM and DP can be found by using Equation 3.8 and the relation between them.

A similar algorithm can also be developed for the sense mode. Figure 3.3 shows the resonance test schematic of sense mode. Similarly the relation between input and output can be found by,

$$\frac{V_{out}(s)}{V_{in}(s)} = \frac{F_S(s)}{V_{in}(s)}\frac{Y_S(s)}{F_S(s)}\frac{I_S(s)}{Y_S(s)}\frac{V_{out}(s)}{I_S(s)} \quad 3.9$$

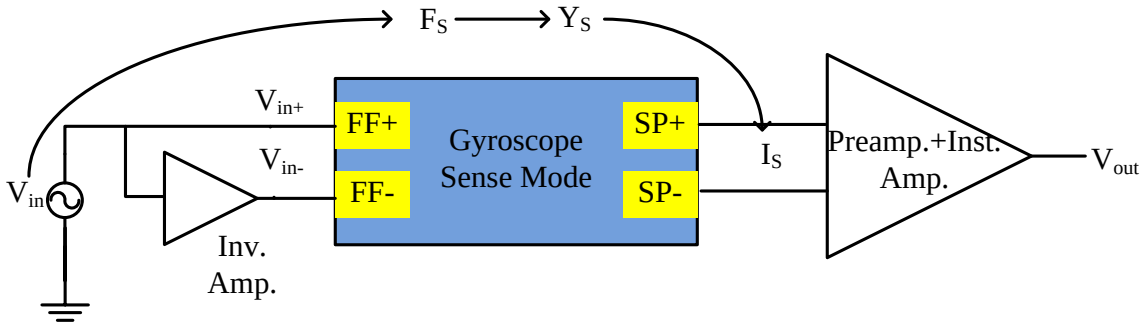

Figure 3.3: Schematic of sense resonance test

In a similar way of equation 3.6,

$$\frac{V_{out}(s)}{V_{in}(s)} = V_{PM}\frac{\partial C_{FF}}{\partial y}\frac{1}{m_S\left(s^2+\frac{w_S}{Q_S}s+w_S^2\right)}V_{PM}\frac{\partial C_{SP}}{\partial y}sZ_{interface}A_{int.amp.} \quad 3.10$$

$$\frac{V_{out}(s)}{V_{in}(s)} = \frac{V_{PM}^2\frac{\partial C_{FF}}{\partial y}\frac{\partial C_{SP}}{\partial y}sZ_{interface}A_{int.amp.}}{m_S\left(s^2+\frac{w_S}{Q_S}s+w_S^2\right)} \quad 3.11$$

At sense resonance frequency,

$$\frac{V_{out}(s)}{V_{in}(s)} = \frac{1}{m_S}V_{PM}^2\frac{\partial C_{FF}}{\partial y}\frac{\partial C_{SP}}{\partial y}\frac{Q_S}{w_S}Z_{interface}A_{int.amp.} \quad 3.12$$

A similar algorithm can be followed as in finding the sensitivity of drive mode. A relation between force feedback sensitivity $\partial C_{FF}/\partial y$ and sense mode sensitivity $\partial C_{sp}/\partial y$ is extracted though layout and their exact numerical values are found using Equation 3.12.

Different from drive mode the inputs and outputs are differential in sense mode. Noise in sense mode is critical and determines the minimum detectable rate, differential input and outputs are used to suppress the noise and increase noise immunity.

The phase difference between input and output signal at resonance depends on the preamplifier type used. If the interface is resistive, there is no phase difference between input and output signals. If capacitive type used there exists 90^0 phase difference between input and output.

3.3 Design of Drive and Sense Control Electronics for MEMS Gyroscopes

Gyroscope has basically two modes; namely drive and sense mode. From control electronics point of view, two modes are examined separately. Both the drive and sense mode control electronics are designed for closed loop, and they will be examined respectively. The followed procedure in controller design is as follows, first the open loop transfer function is obtained with simplified gyro model and controller parameters are found analytically, then the system is verified in SIMULINK design environment.

3.3.1 Drive Mode Control Electronics

Definition of Coriolis force states the direct relation between drive displacement and Coriolis force amplitude in Equation 2.1. The induced Coriolis force on sense mode due to an applied rate is directly multiplied with the amplitude of drive displacement. Drive displacement is one of the factors that determines the scale factor of the gyroscope. Drive mode amplitude control is absolutely necessary for the drive mode of the gyroscope to ensure constant scale factor.

Drive mode is operated at its resonance frequency to obtain maximum displacement with minimum applied actuation voltage. At vacuum drive mode quality factor exceeds few tens of thousands which makes it a very sharp bandpass filter. Since the gain of the system is also high with positive feedback the system is easily locked to drive mode resonance frequency. Self oscillation starts with the environmental noise. Then with amplitude control mechanism drive displacement is kept constant. Figure 3.4 shows the closed loop control mechanism for drive mode.

To explain qualitatively, drive pick signal (V_{DP}) is first demodulated with itself and passed through a low pass filter (LPF). After LPF drive pick signal is converted into DC which gives information about the amplitude of drive displacement. DC potential is compared with a reference DC voltage (desired drive displacement amplitude) and the error output is fed to a PI controller. PI controller works and stabilizes the circuit when error signal (V_{error}) is zero, i.e. when the designed drive displacement is achieved. Output of PI controller is DC and it is fed to a switching modulator which drives the gyro. Controller's output determines the amplitude of modulated signal. Since the modulator is a switching one, the output is a square wave. Noting that the gyroscope is operated at vacuum and quality factor is high only the first harmonic of the square wave drives the gyro. Higher harmonics are eliminated by the bandpass filter characteristics of the gyroscope.

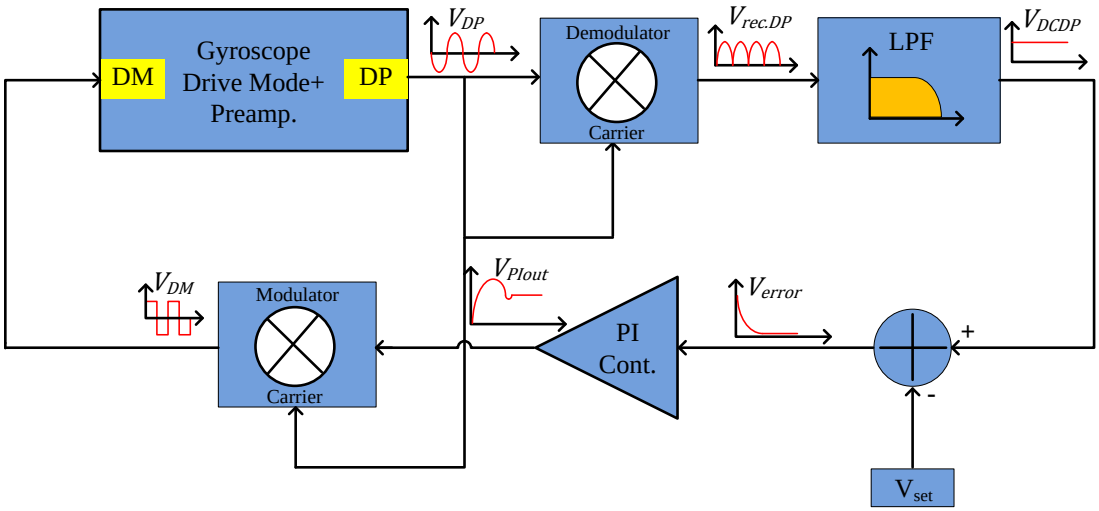

Figure 3.4: Closed loop control mechanism for drive mode

In the design of electronics the phase of the carrier applied to modulator and demodulator is crucial. Resistive preamplifier is used in drive mode and at resonance according to Equation 3.8 input and output of the gyroscope is in phase. So carrier of modulator should be chosen the drive pick signal itself. For demodulation DP signal should be used since the amplitude of the signal should be detected. Set voltage V_{set} is used to set the drive displacement to the desired value. It should be a constant potential and should not change with environmental conditions and chosen as the output of a bandgap reference. For this design output of the bandgap reference is fixed and the flexibility in drive displacement is achieved by varying the gain of low pass filter.

Before moving to open loop characteristics of drive control circuit to determine controller parameters, PI controller is analyzed. Figure 3.5 shows PI controller implementation with an OPAMP.

The transfer function of the PI controller, with proportional gain K_P and integral gain K_I;

$$C_{PI}(s) = K_P + \frac{K_I}{s} \qquad 3.13$$

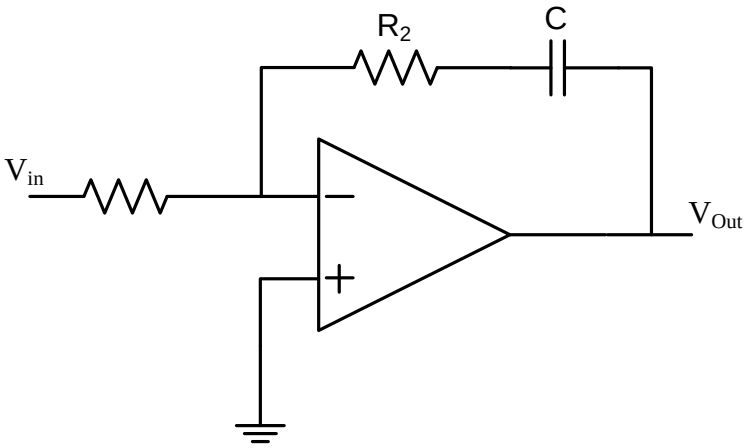

Figure 3.5: PI controller with OPAMP

The transfer function of the circuit shown in Figure 3.5 is found as

$$C(s) = -\frac{V_{out}}{V_{in}} = \frac{R_2}{R_1} + \frac{1}{sCR_1} \qquad 3.14$$

Matching Equation 3.13 with 3.14 proportional and integral constants are found as,

$$K_P = \frac{R_2}{R_1} \; and \; K_I = \frac{1}{CR_1} \qquad 3.15$$

As seen a PI controller can be implemented with an OPAMP two resistors and one capacitor.

The controller loop design starts with choosing the amplitude of drive oscillations. With control circuit what can be done is only setting the drive pick signal's amplitude constant. The amplitude of drive pick signal can be found as,

$$V_{DP}(jw) = V_{PM}\frac{\partial C_{DP}}{\partial x} jw_D X_D Z_{interface} A_{int.amp.} \qquad 3.16$$

Capacitive sensitivity of drive pick $\partial C_{DP}/\partial x$ can be found by the procedure described in section 3.2, and the other parameters are known by tests in Equation 3.16. After determining the drive displacement amplitude, the amplitude of the drive pick signal can be found. By adjusting the gain of demodulator and low pass filter desired drive pick amplitude can be set. Note that with this kind of approach not the drive amplitude is

kept constant, instead the product given in Equation 3.16 is kept constant. A variation in the drive resonance frequency w_D will change the drive displacement amplitude. But a few Hz frequency shift will change the drive displacement in the order of $1/10000$ which may not be critical.

In the design stage and during the tests proof mass potential is the main element that determines the drive displacement amplitude. Basically it can be thought the product of drive displacement and proof mass potential is kept constant since the other parameters are fixed. Maximum allowed drive displacement is 10µm for the gyroscope studied in this thesis and drive displacements of 3-7.5µm are analyzed during the tests. In the design procedure explained above the drive pick signal amplitude was set to 760mV peak which corresponds to 4µm displacement for 10V proof mass potential for SOI gyroscope N08. Higher drive displacements are also possible and increases the sensitivity of the sensor but 7.5µm is set as the limit to be on the safe side. Displacements greater than 7.5µm may damage the sensor due to overshoot at start up.

In order to model the drive mode controller, simplified transfer function of the drive mode is needed. Drive mode dynamics between modulator and demodulator at resonance can be simplified to a first order system which can be expressed as [31],

$$H_D(s) = \frac{A_D}{1 + s\frac{2Q_D}{w_D}} \tag{3.17}$$

where $A_D$is the drive resonance gain of the gyroscope Q_D and w_D are the quality factor and resonance frequency of the drive mode, respectively. Under the stated simplification open loop transfer function can be written as (transfer function between DM and modulator output in Figure 3.4)

$$H_{OL}(s) = \frac{A_D}{1 + s\frac{2Q_D}{w_D}} K_D H_{LPF}(s) \frac{K_I\left(1 + s\frac{K_P}{K_I}\right)}{s} K_M \tag{3.18}$$

In equation 3.18, $K_D$is the demodulator gain, $H_{LPF}(s)$ is the transfer function of the LPF and K_M is the gain of modulator.

The PI parameters, maximum overshoot and settling time of the system are adjusted with the parameters of the PI controller. It was found that if pole zero cancellation occurs; i.e.

$$1 + s\frac{2Q_D}{w_D} = 1 + s\frac{K_P}{K_I} \qquad 3.19$$

Then the system becomes simpler. If the equality is formed in Equation 3.19, the settle time is greatly reduced and no overshoot is observed. Since the quality factor and drive resonance frequency varies with gyroscope, PI parameters need to be updated for each gyroscope if settling time and overshoot is critical. Generally the parameters except the parameters of PI controller are fixed. In such a case increasing the integral gain makes the system fast however phase margin is also reduced. An optimization between phase margin and settle time should be found. 60^0 phase margin is the optimum point between stability and settle time.

A simple design procedure for the sample SOI gyroscope N08 is shown below. The resonance characteristics of N08 are given in Table 3.1.

Table 3.1: Drive resonance characteristics of SOI gyroscope N08

Characteristics	**Value**
Resonance frequency	13.9kHz
Gain	15.88dB (6.22)
Quality Factor (Q)	50546
$\boldsymbol{2Q_D/w_D}$	1.16

Using equation 3.18 and 3.19 phase margin of the system is set to 60^0. Since the transfer function is greatly simplified this can be done manually but the phase characteristics of the low pass filter should be taken into account. The lowpass filter was designed using "Texas Instruments Filter Pro" program. The low pass filter is a second order butterworthfilter with multiple feedback topology cut off frequency of 100Hz. Figure 3.6 shows the circuit diagram of the low pass filter .

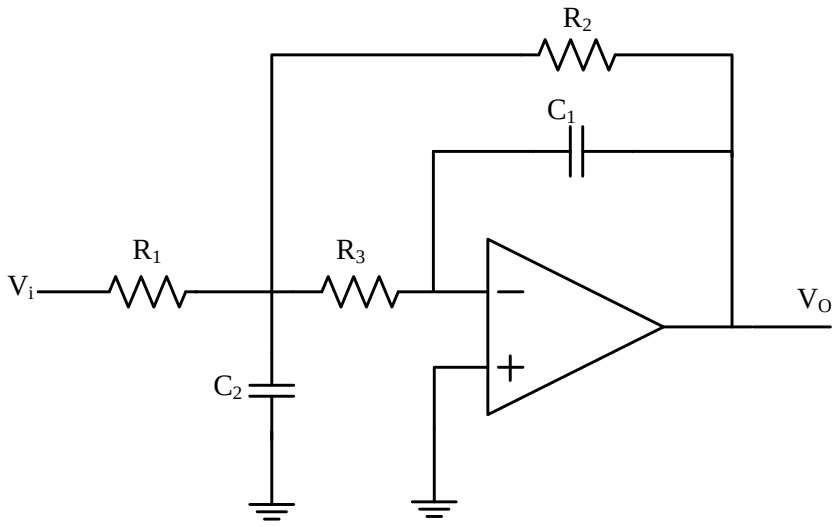

Figure 3.6: Multiple feedback topology Butterworth low pass filter

The transfer function of the low pass filter given in Figure 3.6 is,

$$H_{LPF}(s) = \frac{K_{LPF} w_0^2}{s^2 + \frac{w_0}{Q} s + w_0^2} \tag{3.20}$$

$$Q = \frac{\sqrt{R_2 R_3 C_1 C_2}}{(R_2 + R_3 + |K_{LPF}| R_3) C_1} \tag{3.21}$$

$$K_{LPF} = -\frac{R_2}{R_1} \; and \; w_0 = \frac{1}{\sqrt{R_2 R_3 C_1 C_2}} \tag{3.22}$$

The open loop transfer function given in Equation 3.18, can be rewritten for the sample SOI gyro with LPF transfer function as ;

$$H_{OL}(s) = \frac{6.56}{1 + s1.16} * \frac{2}{\pi} * \frac{4.16 * 394784}{s^2 + 881.1s + 394784} * \frac{K_I \left(1 + s\frac{K_P}{K_I}\right)}{s} * \frac{4}{\pi} \tag{3.23}$$

In Equation 3.23, $2/\pi$ is the rms value of rectified sinus with demodulator gain 1, and $4/\pi$ is the first harmonic of square wave driving the gyro. LPF transfer function is obtained for 4.16 gain and 100Hz cutoff. After a few iterations on MATLAB, K_I was optimized as 5 and $K_P$was found using equation 3.19 $5 * 1.16 = 5.8$. Bode diagram showing the phase margin is given below in Figure 3.7.

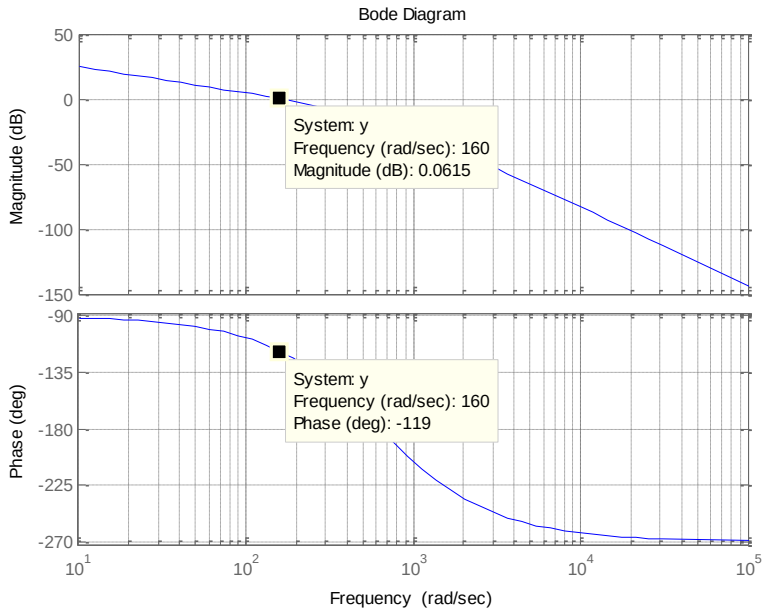

Figure 3.7: Open loop Bode diagram of drive amplitude control circuit

Figure 3.7 shows that, the system has a phase margin of $>60^0$. Settle time and overshoot can be obtained by the step response of closed loop transfer function. Figure 3.8 shows the step response. With pole zero cancellation applied the system settle time is 20msec and no overshoot is observed.

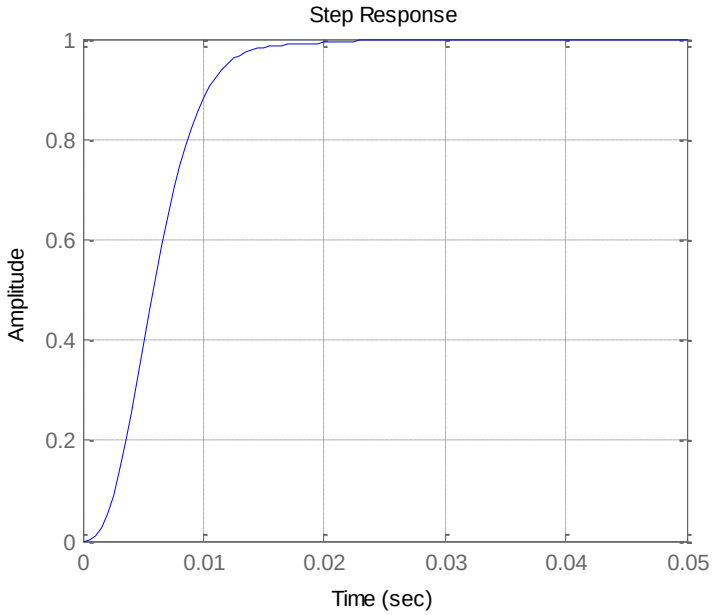

Figure 3.8: Step response of closed loop system

A SIMULINK model is formed for the drive mode of the gyroscope to see the transient response. Figure 3.9 shows the SIMULINK model for the drive amplitude control circuit of the sample gyroscope.

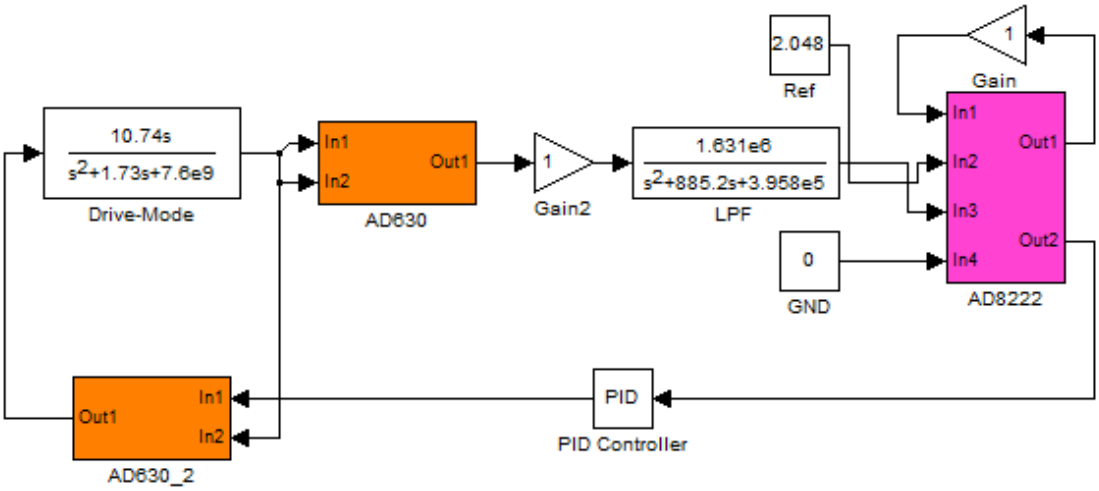

Figure 3.9: SIMULINK model used for drive amplitude control circuit

Drive model given in Figure 3.9 is a realistic model since all the components used in the real circuit are modeled here. Exact second order drive model is used here. Settle time and maximum overshoot can be found using Figure 3.10. Settle time is 25msec and no overshoot observed consistent with analytical modeling. The drive amplitude was set to 760mV as calculated.

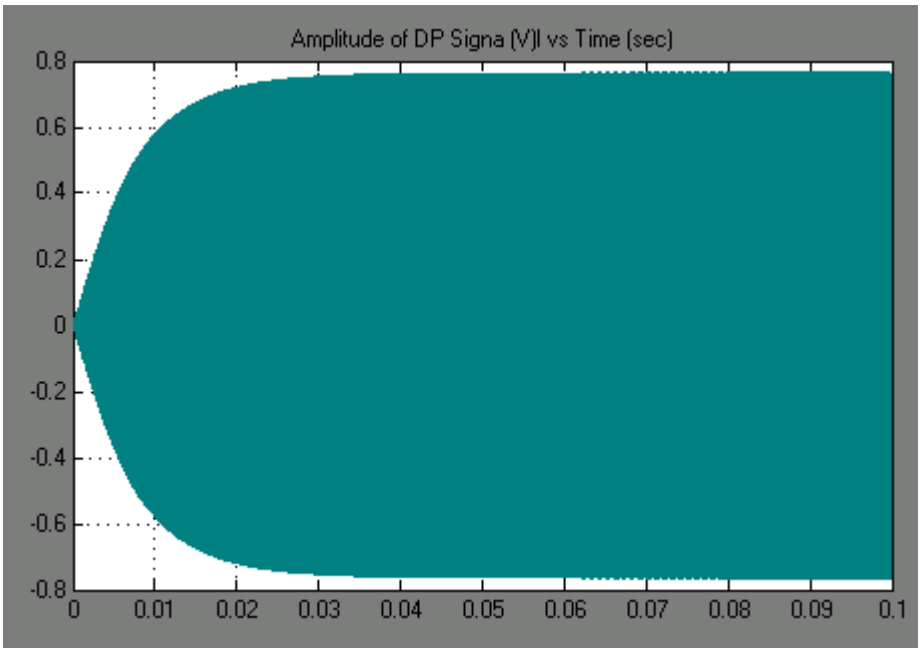

Figure 3.10: Output of drive motor signal in SIMULINK

A detailed analysis on drive control circuit can be found in [31]. In that thesis, effects of square wave drive, sinusoidal drive and half frequency drive are examined. In this study square wave drive signal is applied to the drive motor electrodes of the gyroscope.

3.3.2 Sense Mode Control Electronics

Open loop or closed loop rate sensing can be used in the sense mode of the gyroscope. Details of open and closed loop rate sensing are examined in the following sections.

3.3.2.1 Open Loop Rate Sensing and Quadrature Error

Open loop rate sensing is the standard approach used to extract the rate information. The output of the sense mode is an amplitude modulated signal at drive resonance frequency; so sense signal is demodulated with drive carrier and converted into DC by low pass filtering. Under ideal conditions sense pick signal is only due to applied rate, but in practice there is a large signal besides the rate signal called as quadrature signal. There exists 90^0 phase difference between quadrature and Coriolis signals. Figure 3.11 shows the typical open loop rate sensing structure.

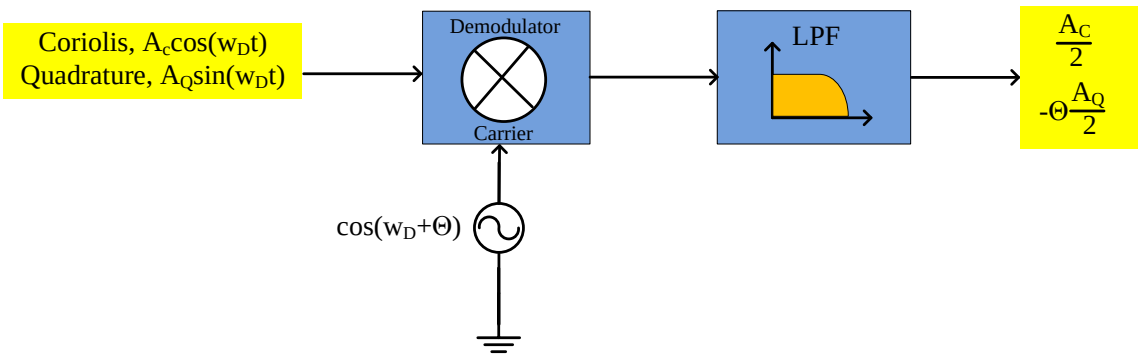

Figure 3.11: Typical open loop rate sensing structure

In Figure 3.11, Θ stands for any phase error introduced during demodulation, w_D for drive resonance frequency, A_C and A_Q for Coriolis and quadrature signal amplitudes respectively. Demodulator output;

$$A_D = cos(w_D t + \Theta)\,[A_C\, cos(w_D t) + A_Q\, sin(w_D t)] \tag{3.24}$$

$$A_D = [cos(w_D t)\, cos\Theta - sin(w_D t)\, sin\Theta][A_C\, cos(w_D t) + A_Q\, sin(w_D t)] \tag{3.25}$$

For small Θ; $cos\Theta \cong 1, sin\Theta \cong \Theta$. Under these assumptions low pass filter output can be found as;

$$A_{LPF} = \frac{A_C}{2} - \frac{A_Q}{2}\Theta \tag{3.26}$$

where $A_Q \gg A_C$. Even small phase errors during demodulation which is inevitable may cause errors at the output.

An analysis showing the quadrature signal's magnitude can be performed as follows. Assume drive displacement;

$$X_D = X_0\ sin(w_D t) \tag{3.27}$$

where X_0 is the maximum drive displacement then Coriolis acceleration in response to an applied rate of Ω_Z is

$$a_C = 2\Omega_Z \times \dot{X}_D = 2\Omega_Z w_D X_0 cos\,(w_D t) \tag{3.28}$$

Quadrature motion is the direct coupling of drive displacement into sense, so quadrature acceleration can be found by directly taking the derivative of drive displacement multiplied with coupling ratio ε.

$$a_Q = -w_D^2 \varepsilon X_0 sin\,(w_D t) \tag{3.29}$$

Then

$$\left|\frac{a_Q}{a_C}\right| = \frac{\varepsilon w_D}{2\Omega_Z} \tag{3.30}$$

For a high performance MEMS gyroscope, Ω_Z is in the order of ^{0}/hour and drive resonance frequency is around 15 kHz. Under these conditions quadrature acceleration a_Q is much larger than Coriolis acceleration a_C. Equation 3.30 shows how large quadrature signal can be.

Ideally no phase error exists and the output is only Coriolis force. The Coriolis force amplitude sensed by the gyroscope is a voltage signal (the output of instrumentation amplifier, refer to Figure 3.3) and can be expressed as

$$A_C = V_{PM} \frac{\partial C_{DP}}{\partial y} j w_D Y_S Z_{interface} A_{int.amp.} \tag{3.31}$$

In Equation 3.31 the Coriolis force amplitude directly depends on sense displacement Y_S which is given in 2.17 and 2.21 for matched and mismatched modes respectively, as

$$Y = \frac{2X_D \Omega_z Q_S}{j w_D} \frac{m_{PM}}{m_S}, matched\ mode \tag{3.32}$$

$$Y = \frac{X_D \Omega}{\Delta w} \frac{m_{PM}}{m_S}, mismatched\ mode \tag{3.33}$$

The frequency separation between drive and sense modes Δw and quality factor Q depends on vacuum conditions. The gyroscope is vacuum packaged but the vacuum level inside the package may vary with time, causing a drift of the quality factor and frequency separation which results in a change in scale factor. Open loop rate sensing is

not a reliable method for long term operation of the gyroscope. Instead a closed loop rate sensing mechanism can be used which is more reliable.

Phase sensitive demodulation is used both in open and closed loop rate sensing mechanism. As found in Equations 3.26 and 3.30 the quadrature signal may cause offsets at the output. Canceling the quadrature error will make phase sensitive demodulation more effective and decrease the unwanted offset at the output.

3.3.2.2 Closed Loop Rate Sensing

The main idea behind closed loop rate sensing is sensing the induced Coriolis motion on the sense mode of the gyroscope and stopping it, and the required potential to stop the Coriolis motion is given as output. Closed loop rate sensing is called as force feedback which requires additional electrodes placed on the gyroscope.

Force feedback is commonly used in commercial gyroscopes in the market since it ensures robust operation. The applied force on force feedback electrodes should stop the Coriolis force, then

$$V_{PM}\frac{\partial C_{FF}}{\partial y}V_{FF} = 2m_{PM}\Omega j w_D X_D \tag{3.34}$$

$$V_{FF} = \frac{2m_{PM}\Omega j w_D X_D}{V_{PM}\frac{\partial C_{FF}}{\partial y}} \tag{3.35}$$

In equations 3.34 and 3.35 $V_{FF}$is the amplitude of AC signal applied to force feedback electrode and $\partial C_{FF}/\partial y$ is the sensitivity of the force feedback electrode. The amplitude of the applied AC signal V_{FF} is the measure of applied rate and it is the output of the closed loop circuit. The parameters that determine V_{FF} do not depend on vacuum conditions; they are stable throughout the gyroscope life. In closed loop operation the scale factor of the gyroscope is expected to be more stable compared to open loop operation. In addition it improves linearity since sense mode does not move (for high rates due to varying gap type sensing linearity can be deteriorated) and bandwidth can also be adjusted with controller parameters in closed loop. Figure 3.12 shows the block diagram of closed loop rate sensing.

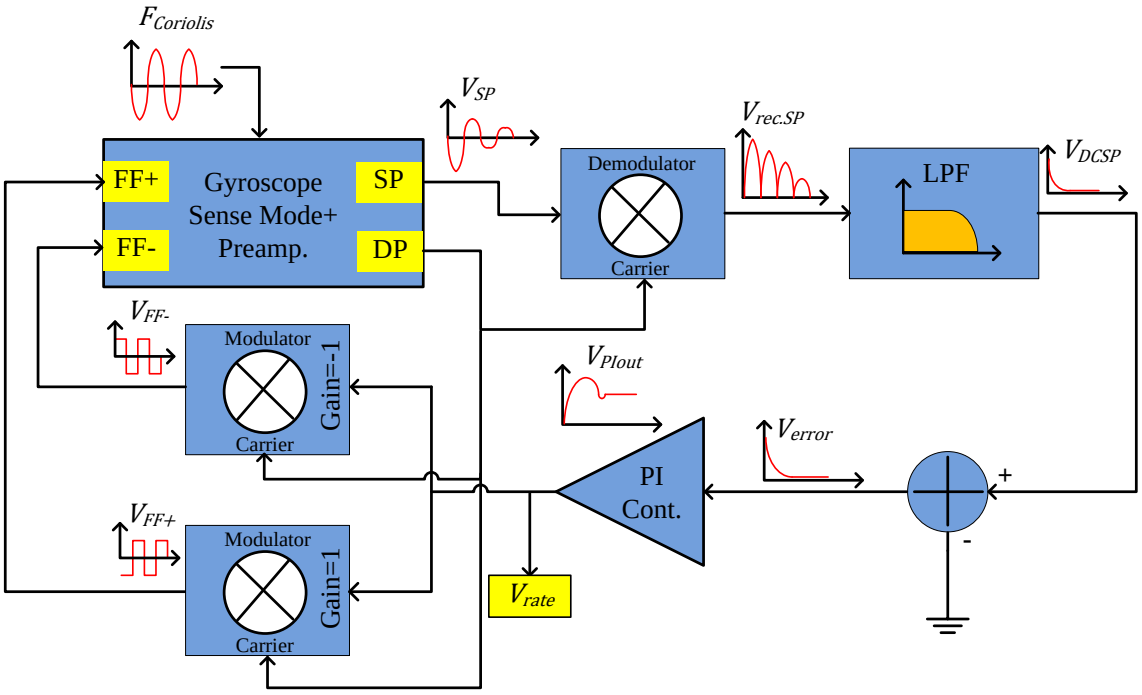

Figure 3.12: Block diagram of closed loop rate sensing

Referring to Figure 3.12, Coriolis force is sensed by the sense mode of the gyroscope and controller acts to stop the movement of sense mode by applying required potentials to force feedback electrodes. In the closed loop configuration sense mode does not move, i.e. it is always kept stationary by the PI controller. The amplitude of the stopping voltage is given to outer world as rate information.

The gyroscope is operated at mismatch conditions meaning that sense mode operates at off resonance conditions. So the approximation given in Equation 3.17 cannot be applied to sense mode controller design. Instead sense mode dynamics can be modeled as a constant gain stage under mismatch conditions given in Equation 2.20. Then open loop transfer function of the sense mode controller can be written as (the transfer function from the input of force feedback electrodes to the output of modulator in Figure 3.12)

$$H_{OL}(s) = \frac{V_{SP}(s)}{V_{FF}(s)} K_D H_{LPF}(s) H_{PI}(s) K_M \qquad 3.36$$

In equation 3.36 $K_D$is the gain of demodulator, $H_{LPF}(s)$ is the transfer function of the low pass filter, $H_{PI}(s)$ is the transfer function of the PI controller and $K_M$is the gain of modulator. Assuming mismatch conditions $V_{SP}(s)/V_{FF}(s)$ can be considered as constant and taken as a constant gain stage. With this assumption controller design procedure is simplified otherwise the envelope of the sense mode should be found under mismatch conditions. Two sense resonance peaks are observed during vacuum tests as it will be explained Section 5.1. Two sense peaks can be considered as single peak which is the sum of two peaks. The gain under mismatch conditions can be found by inserting the drive resonance frequency into the model found in Equation 3.11. The open loop transfer function for the sample SOI gyroscope N08 can be expressed as

$$H_{OL}(s) = 0.93 * \frac{4}{\pi} * \frac{6.56 * 394784}{s^2 + 881.1s + 394784} * \left(\frac{K_P s + K_I}{s}\right) * \frac{4}{\pi} \qquad 3.37$$

In Equation 3.37 the first $4/\pi$ is the multiplication of (2) demodulator gain with the rms value of rectified sinus ($2/\pi$) and second $4/\pi$ is the first harmonic of driving square wave. LPF with gain 6.56 and 100Hz cutoff frequency is used in the design. Using the transfer function in Equation 3.37, after a few trials with no overshoot and 75^0 phase margin $K_P = 0$ and $K_I = 10$ is found using MATLAB. Introducing a proportional gain (a zero to the system) degrades the response of low pass filter and step response. The low pass characteristic of the system should be preserved since system operation is based on low pass filter. With proportional PI controller gain being equal to zero, low pass characteristic of the system is preserved. Another option is setting the zero of PI controller much greater than the cutoff frequency of low pass filter, but no use of that is found during simulations.

Figure 3.13 and Figure 3.14 show the open loop bode plot and closed loop step response of the modeled system. Using Figure 3.13 phase margin of the system is found as 75^0 using step response settle time is 35msec.

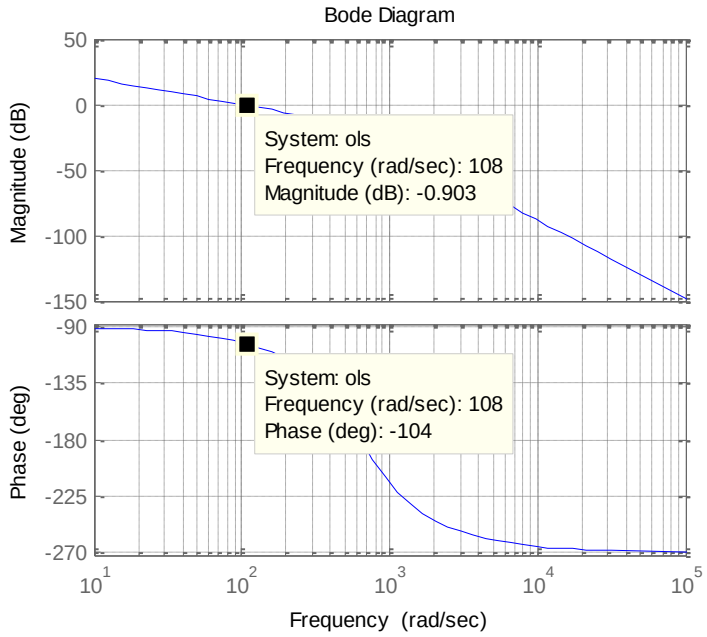

Figure 3.13: Bode plot for sense mode controller design

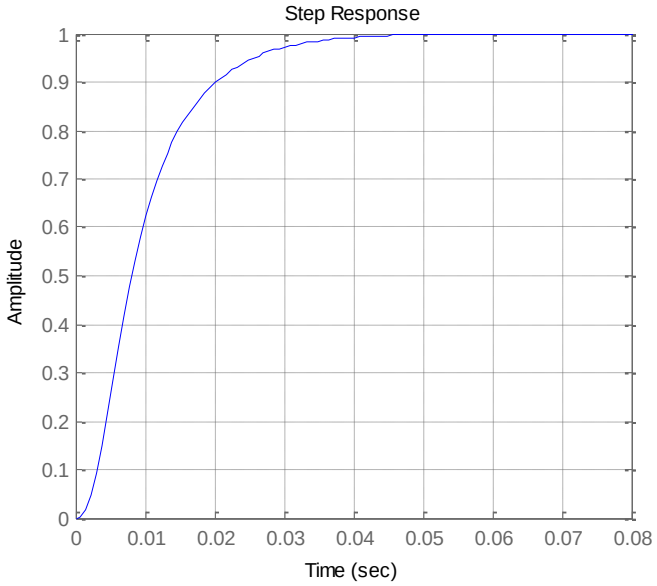

Figure 3.14: Step response of closed loop sense mode

Figure 3.15 shows the formed SIMULINK model for force feedback circuit. In this SIMULINK model two sense peaks are modeled separately, and the Coriolis signal is given as a disturbance. The sense pick signal as a result of an angular rate $1^0/\text{sec}$ is given below in Figure 3.16. The settle time of the system is 35msec and consistent with

analytical formulation obtained from simplified transfer function and step response. During the simulations analytically found integral gain of 10 was used.

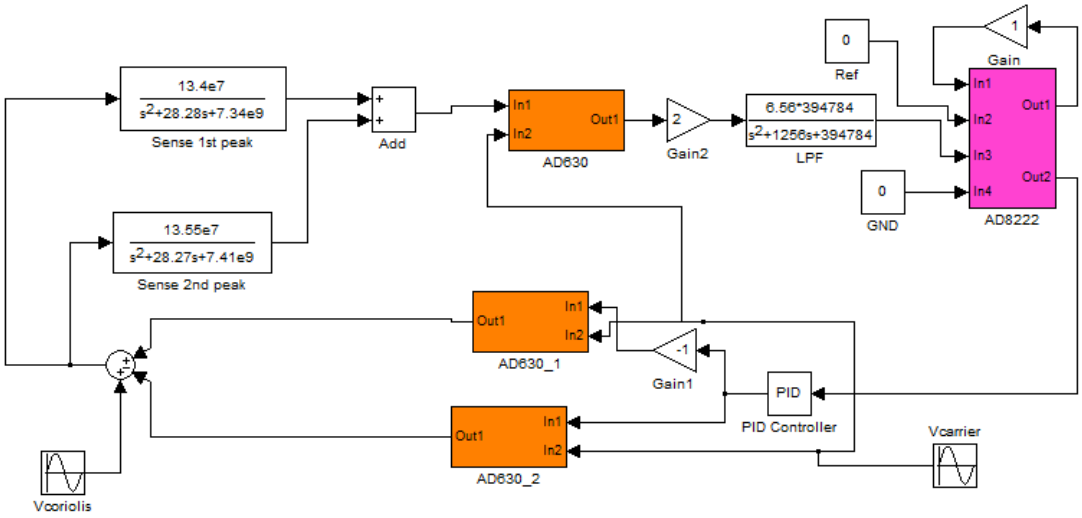

Figure 3.15: SIMULINK model for force feedback circuit

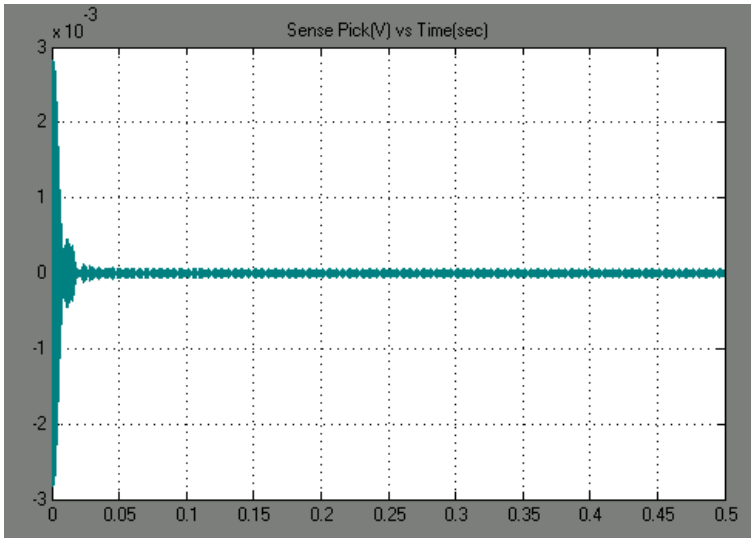

Figure 3.16: Sense pick signal after applied rate

Bandwidth is another critical design parameter of the gyroscope and should be considered during simulations. To measure the bandwidth of the system a periodic chirp signal is multiplied with Coriolis signal applied to the system and the output of PI controller (rate output) is monitored. The frequency of periodic chirp signal is swept from 0 to 100Hz in 5 seconds. In other words the frequency of applied 1^0/sec Coriolis

force is changed from 0Hz to 100Hz. Figure 3.17 shows the rate output. As expected the rate output cannot follow the applied time varying rate after a certain frequency and the amplitude of the rate signal starts to decrease. By using Figure 3.17, the bandwidth of the force feedback system is found as 80Hz which corresponds to 3dB point (4 seconds = 80 Hz).

In this study gyroscope is operated always in closed loop both in sense and drive mode to ensure stable operation throughout the time.

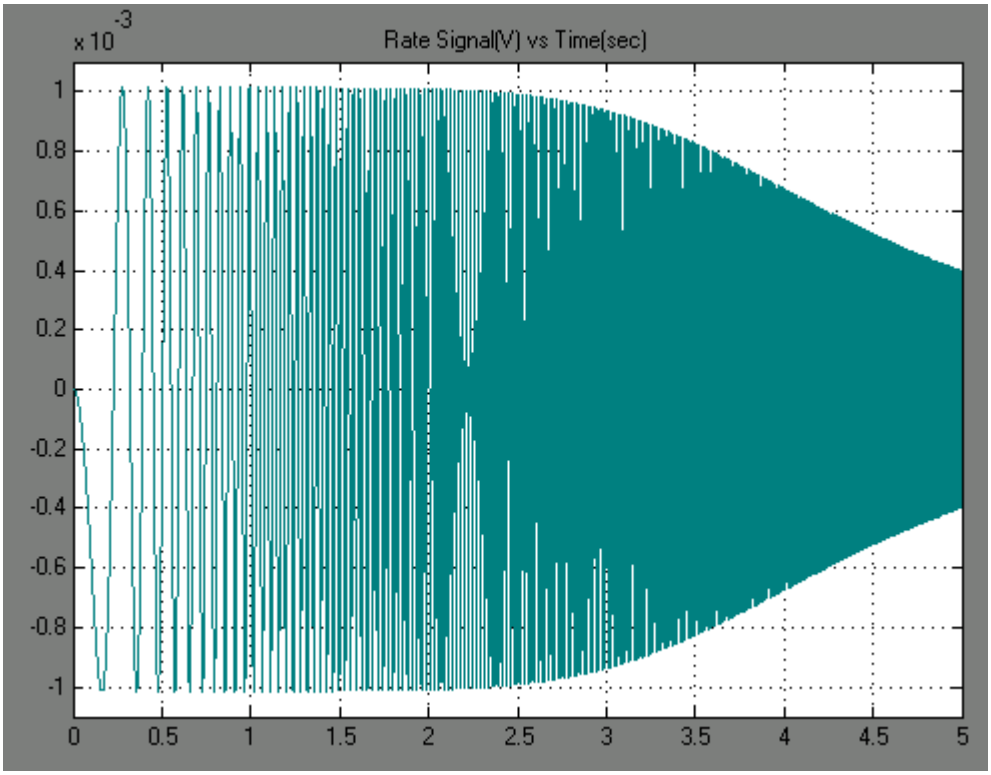

Figure 3.17: The response of the gyroscope to a time varying rate

3.4 Design of Quadrature Control Electronics

The control electronics for quadrature circuit is similar to the control mechanism used in force feedback. Since we want to detect quadrature signal, the carrier used to demodulate the sense pick (SP) signal should be 90^0 phase shifted version of the carrier that is used to detect rate. Drive pick signal (DP) is used as the carrier in force feedback module which detects rate, so to detect quadrature signal 90^0 phase shifted DP signal is

used. After demodulating the quadrature signal it is converted to DC by a low pass filter (LPF) and compared with ground. The comparison result is the input of a PI controller and the output of the PI controller is a DC signal. This DC signal is the required quadrature potential ΔV, the required inverse $-\Delta V$ is obtained through an inverting amplifier. Figure 3.18 shows the block diagram of the quadrature cancellation electronics.

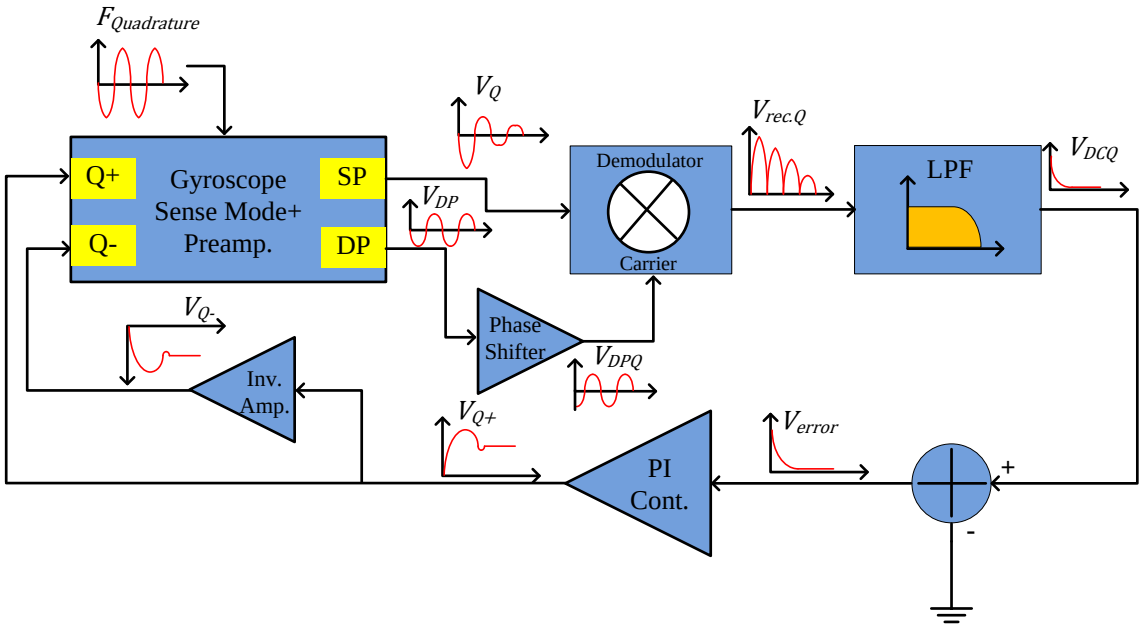

Figure 3.18: Block diagram of quadrature cancellation electronics

No bandwidth considerations exist for the quadrature circuit since the quadrature signal's frequency is always at drive resonance frequency. This is the main difference between force feedback controller design and quadrature circuit controller design. The applied quadrature force by the controller acts on sense mode dynamics. For modeling purposes, under mismatch conditions sense mode dynamics can be thought as constant gain stage. The open loop transfer function of the system shown in Figure 3.18 can be expressed as

$$H_{OL}(s) = \frac{V_{SP}(s)}{F_Q(s)}\Big|w = w_D \cdot K_D H_{LPF}(s) H_{PI}(s) K_{quad} \qquad 3.38$$

$$\frac{V_{SPquad}}{F_Q} = \frac{Y}{F_Q}\frac{I_{SP}}{Y}\frac{V_{SPquad}}{I_{SP}} \tag{3.39}$$

By substituting Equation 2.48 into 3.39 and including other terms,

$$\frac{V_{SPquad}}{F_Q} = \frac{1}{m_S(s^2 + \frac{w_S}{Q_S}s + w_S^2)} V_{PM} \frac{\partial C_{SP}}{\partial y} \frac{1}{C} A_{Inst.Amp.} \tag{3.40}$$

In Equation 3.38 K_D is the gain of demodulator, H_{LPF} is the transfer function of the low pass filter, H_{PI} is the transfer function of the PI controller and K_{quad} is the gain of quadrature configuration. K_{quad} can be found by dividing Equation 2.45 by quadrature potential ΔV,

$$K_{quad} = n\frac{4V\varepsilon Xh}{d^2} \tag{3.41}$$

Note that in quadrature controller design no modulator gain is included, it is included in drive and sense control electronics due to square wave driving modulator. Thanks to the structure of quadrature electrodes the structure automatically drives the gyroscope sinusoidal. Equation 3.38 can be written for SOI gyroscope N08 as (with demodulator gain 1, second order low pass filter cut off 100Hz and gain 1)

$$H_{OL}(s) = 3.5 * 10^6 * \frac{2}{\pi} * \frac{394784}{s^2 + 879.5s + 394784} * \frac{K_P s + K_I}{s} * 1.03 * 10^{-7} \tag{3.42}$$

The quadrature controller design is similar to force feedback, the low pass characteristics of the system should be preserved to ensure proper operation. For that reason the zero introduced by the PI controller should be out of band of the poles of the low pass filter. Setting the proportional gain to zero is feasible like in force feedback. Figure 3.19 and Figure 3.20 provide the bode plot and step response with integral gain of 100.

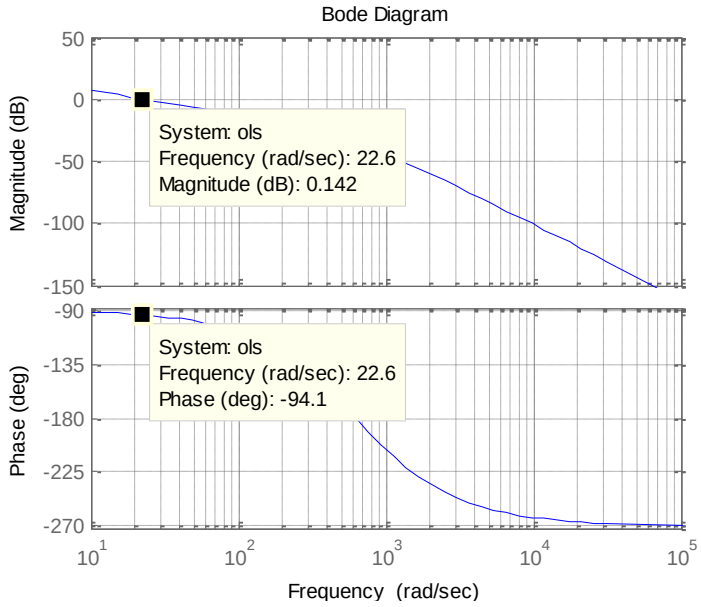

Figure 3.19: Open loop Bode plot for quadrature controller design

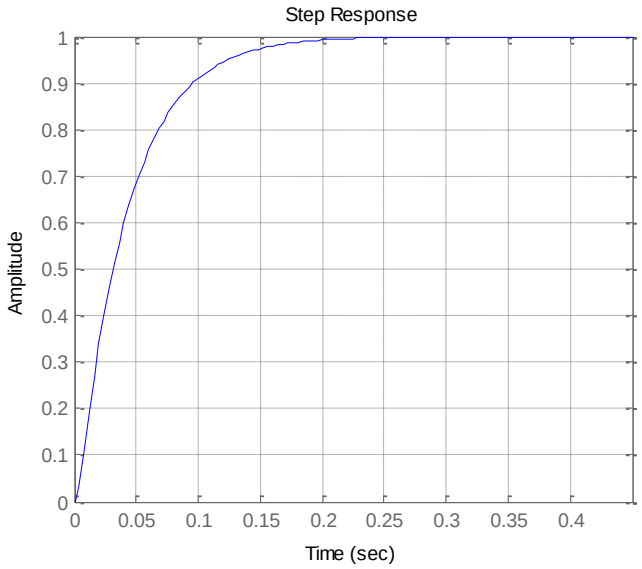

Figure 3.20: Closed loop step response of quadrature controller

The system has a phase margin of 86^0, settles with no overshoot and settle time is 25msec found from Figure 3.19 and Figure 3.20 respectively. To verify the analytical results and see the transient response a SIMULINK model for the quadrature cancellation circuit is formed as in drive control and force feedback circuits.

In the actual system the output of the PI controller generates the quadrature force on the gyroscope. For that reason first the transfer function from F_Q to V_{SPquad} should be found which is given in Equation 3.40 to form the SIMULINK model. Figure 3.21 shows the SIMULINK model for quadrature circuit of SOI gyroscope N08.

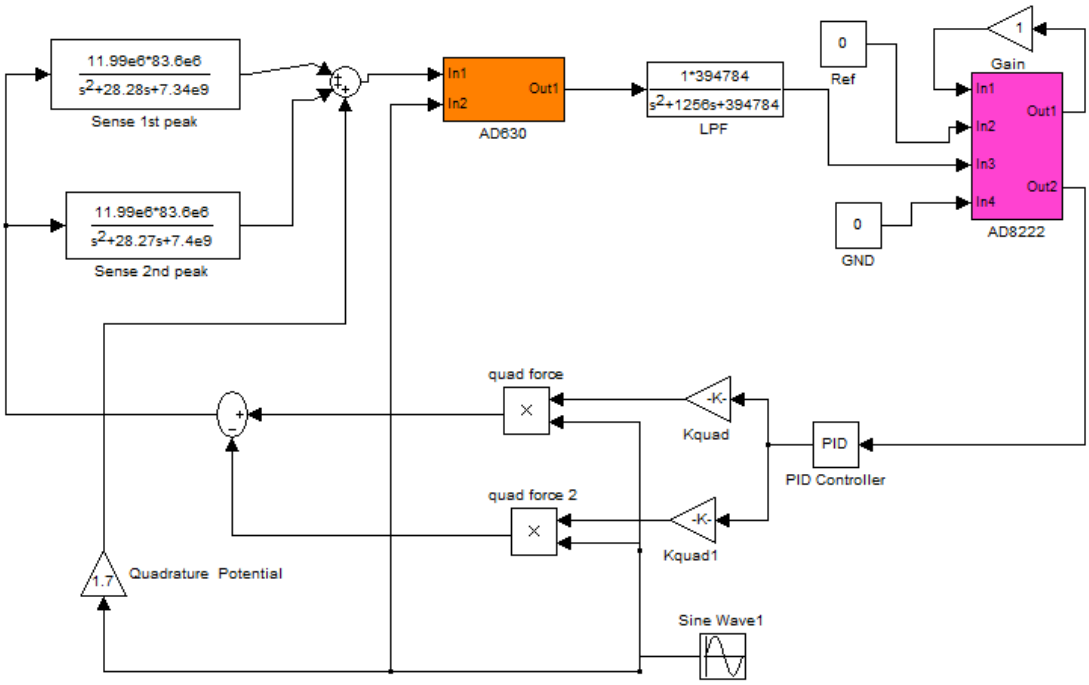

Figure 3.21: SIMULINK model for quadrature circuit

As in force feedback two sense peaks are observed at sense mode and they are modeled as two separate resonators. In SIMULINK model measured quadrature signal amplitude is given to the system as disturbance through "Quadrature Potential" node. Since SIMULINK performs time domain simulation and the transfer function is adjusted to take force as input, the input of the gyroscope module in Figure 3.21 is the applied quadrature force. The parameters used in Figure 3.21 are the parameters of SOI gyroscope N08, and the simulation results are shown in Figure 3.22.

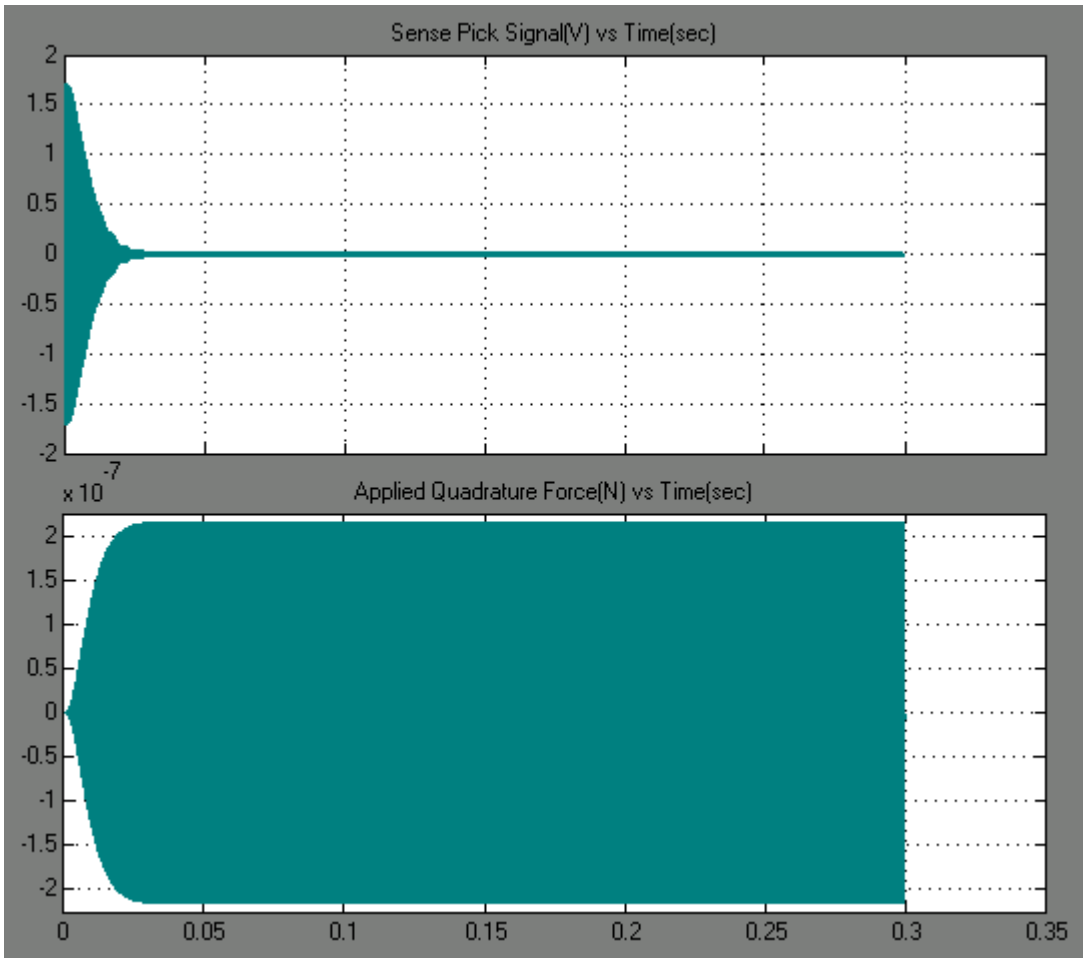

Figure 3.22: SIMULINK results of SOI gyroscope N08

Settle time of the circuit is 30ms, extracted from "Sense Pick Signal" and there is no overshoot observed on the "Applied Quadrature Force". Applied force is in the order of $2.1*10^{-7}$N. During the simulations analytically found PI controller with integral gain 100 was used.

3.5 Noise Analysis of Readout Electronics and Mechanical Structure

In the following sections noise analysis of open loop sense electronics, closed loop sense electronics and mechanical structure (Brownian noise) is performed, respectively.

3.5.1 Noise Performance of Open Loop Sense Electronics

Performance limit of the gyroscope is determined by the sense mode electronics. High performance gyroscope design requires intense care in sense mode preamplifier and control electronics, since the currents to be detected are in the order of femto amperes. Noise contribution of each component should be modeled exactly and components should be chosen carefully. Figure 3.23 shows a capacitive preamplifier.

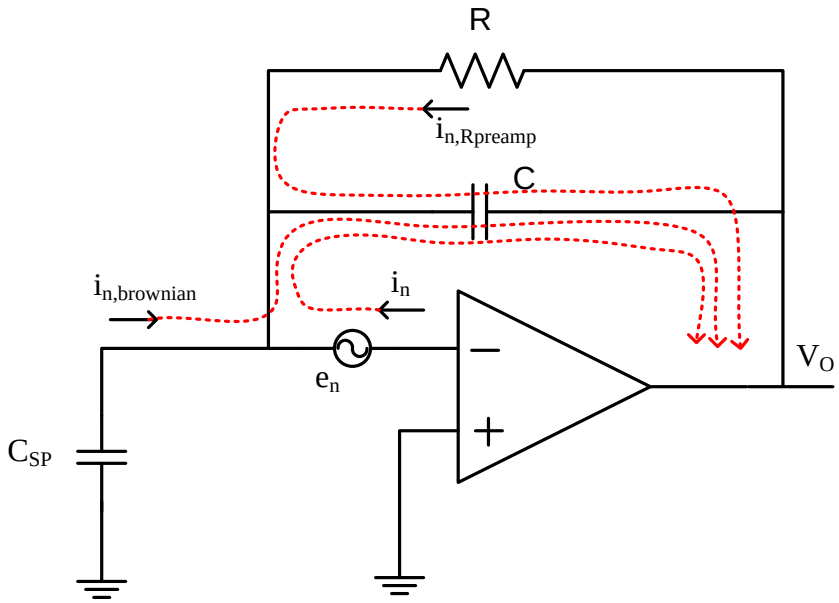

Figure 3.23: Noise sources of preamplifier

Referring to Figure 3.23 $i_{n,brownian}$ denotes the noise current due to Brownian motion (will be explained in the next section) of the sense mode. Brownian noise of the sensor is converted in voltage through the preamplifier as the rate information. This kind of noise is due to mechanical sensor and it is inevitable, but it can be suppressed by vacuum packaging. The other noise source is the electronic noise and analyzed next.

The noise in the sense mode of the gyroscope is dominated by the preamplifier stage, where the output current of the sensor is converted into voltage. At the preamplifier stage three mechanisms produce noise, i_n current noise of the OPAMP and converted into voltage through the impedance of the capacitive preamplifier, e_n voltage noise of the OPAMP converted into voltage through the noise gain of the preamplifier, and $i_{n,Rpreamp}$

current noise of the shunt resistor converted into voltage through the impedance of capacitive preamplifier.

Figure 3.24 shows the detailed open loop configuration and the used components.

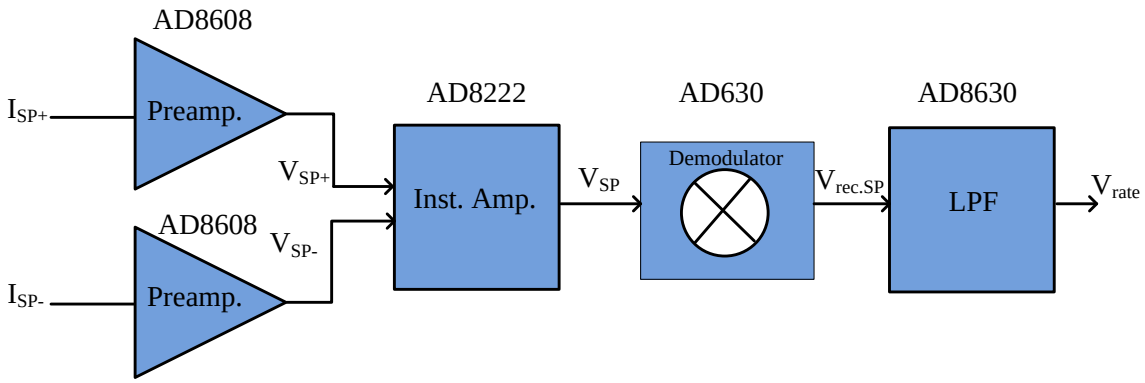

Figure 3.24: Components used in open loop rate sensing

AD8608 from Analog Devices is used as the preamplifier stage in the sense and drive mode electronics. Input referred current noise density of AD8608 at 1kHz is specified as 10fA/√Hz and input referred voltage noise density of AD8608 at 10kHz is specified as 6.5nV/√Hz in [47].

Table 3.2 shows the component and frequency values used in noise calculations.

Table 3.2: Parameter values used in noise calculations

Parameter	Value
Operation Frequency (f)	13.5 kHz
Preamplifier Capacitance (C)	3.9pF
Output Capacitance of the Sense Mode (C_{SP})	5.5pF
Preamplifier Resistance (R)	470MΩ

Input current noise of the OPAMP is converted into voltage by preamplifier,

$$V_{n1} = 10\frac{fA}{\sqrt{Hz}}\frac{1}{w_D C_{preamp}} = 30.23\frac{nV}{\sqrt{Hz}} \quad 3.43$$

Noise gain of the preamplifier can be found by using Figure 3.25, taken from [48].

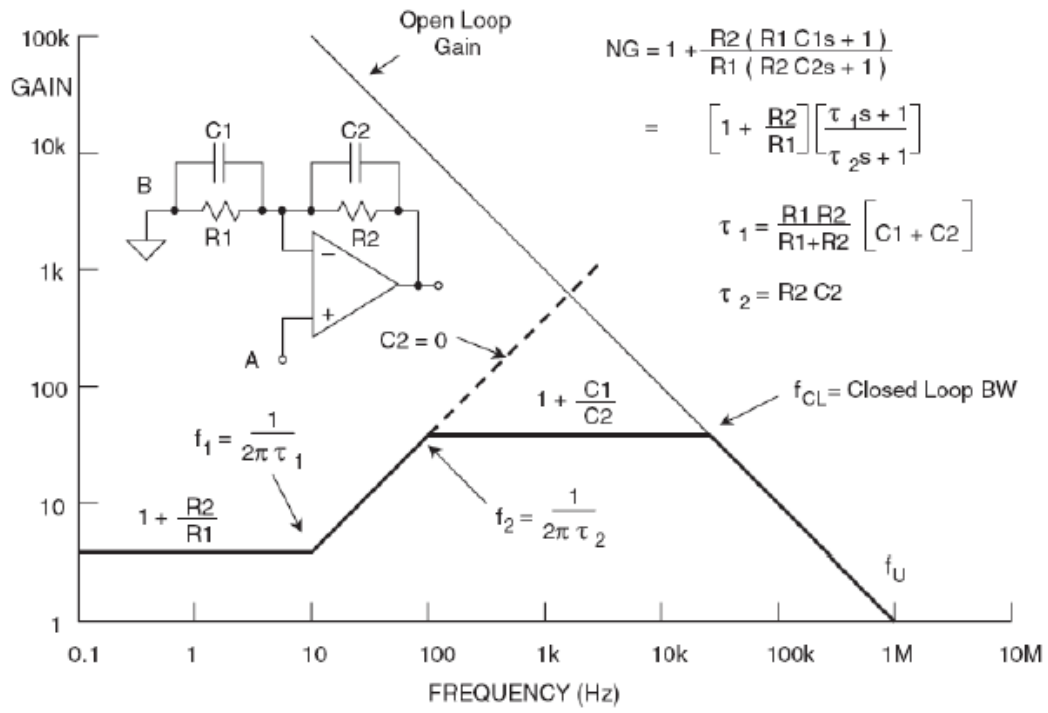

Figure 3.25: Noise gain of preamplifier vs frequency graph [48]

The operation frequency is found to be in the flat gain region. So the output noise due to voltage noise of the OPAMP can be found by

$$V_{n2} = 6.5\frac{nV}{\sqrt{Hz}}\left(1+\frac{5.4pF}{3.9pF}\right) = 15.5\frac{nV}{\sqrt{Hz}} \quad 3.44$$

The current noise of the resistor is converted into voltage by preamplifier

$$V_{n3} = \sqrt{\frac{4k_BT}{R_{preamp}}}\frac{1}{w_D C_{preamp}} = 17.94\frac{nV}{\sqrt{Hz}} \quad 3.45$$

Then total electronic noise at the output of preamplifier can be found as

$$V_{n,preamp} = \sqrt{V_{n1}^2 + V_{n2}^2 + V_{n3}^2} = 38.42\frac{nV}{\sqrt{Hz}} \quad 3.46$$

After the preamplifier stage instrumentation amplifier AD8222 with gain of 20.3 used. Input referred noise model of AD8222 is given in [49] as

$$V_{n,AD8222} = \sqrt{e_{n1}^2 + \left(\frac{e_{n0}}{G}\right)^2},\ e_{n1} = 8\frac{nV}{\sqrt{Hz}}\ and\ e_{n0} = 75\frac{nV}{\sqrt{Hz}} \tag{3.47}$$

where G denotes the gain. With a gain of 20.3 input referred noise of AD8222 was calculated as 8.81 $nV/\sqrt{Hz}$.

Total noise at the output of AD8222

$$V_{n,AD822out} = 20.3\sqrt{2(8.81^2 + 38.42^2)} = 1.13\frac{\mu V}{\sqrt{Hz}} \tag{3.48}$$

Noise is multiplied by 2 since dual channels of AD8222 are used. Referring to Figure 3.24, demodulator and low pass filter are used after amplification of rate signal. As demodulator "Balanced AD630 Demodulator" is used and is given in datasheet [50] that it can recover signal from 100dB noise, it is assumed that noise contribution of demodulator is zero. The last stage is the low pass filter, the rate information is converted into DC. At DC the most significant noise is the flicker or 1/f noise. AD8630 is chosen at DC signal processing blocks due to its low flicker noise. 1/f corner frequency can be found by using the equation is given in [48],

$$\frac{V_{n,p-p}(F_L, F_H)}{6.6} = V_{n,rms}(F_L, F_H) = V_{n,w}\sqrt{F_C ln\left(\frac{F_C}{F_L}\right) + F_H - F_C} \tag{3.49}$$

In equation 3.49 $V_{n,w}$ is the white noise density, F_C is the corner frequency, F_H and F_L are the upper and lower frequency limits of the flicker noise measurement. For AD8630, $V_{n,p-p} = 0.5\mu V\ p-p, V_{n,w} = 22\,nV/\sqrt{Hz}, F_H = 10Hz\ and\ F_L = 0.1Hz$ which are given in [51]. With these values corner frequency is found as 1.2Hz. With typical values standard OPAMPs have corner frequencies higher than 500Hz. 1.2Hz corner frequency makes AD8630 a good choice for DC signal processing. In noise calculations flicker noise of AD8630 is ignored since with 1.2Hz corner frequency it has almost 0 1/f

noise. Only voltage noise of AD8630 is included. Noise contribution of AD8630 with 6.54 gain low pass configuration is

$$V_{n,AD8630} = 22\frac{nV}{\sqrt{Hz}}(1 + 6.54) = 165.88\frac{nV}{\sqrt{Hz}} \quad 3.50$$

Total noise at the output of the low pass filter

$$V_{n,tot} = \sqrt{\left(1.13\frac{\mu V}{\sqrt{Hz}}\frac{4}{\pi}6.54\right)^2 + \left(165.88\frac{nV}{\sqrt{Hz}}\right)^2} = 9.41\frac{\mu V}{\sqrt{Hz}} \quad 3.51$$

The total noise at the output of AD8222 (Equation 3.48) is first demodulated with gain 2 ($4/\pi$) and then multiplied with the gain of low pass filter (6.54). In the above calculations noise coming from the resistors of low pass filter is not calculated. It is found that noise coming from those resistors is small compared to preamplifier noise.

In order to find rate equivalent noise, scale factor of the gyroscope should be known. Scale factor of the SOI gyroscope N08 for mismatch conditions and 10V proof mass potential was calculated as 26.32mV/ ^{0}/sec. The rate equivalent open loop electrical noise is found to be 1.29^0/hr/√Hz. Note that scale factor directly depends on proof mass voltage and frequency mismatch between drive and sense modes.

3.5.2 Noise Performance of Closed Loop System

It is a rule of thumb that feedback worsens the noise performance of open loop dynamics due to additional noise of feedback electronics. However with proper design the noise contribution of feedback can be minimized. Figure 3.26 provides closed loop structure for the gyroscope.

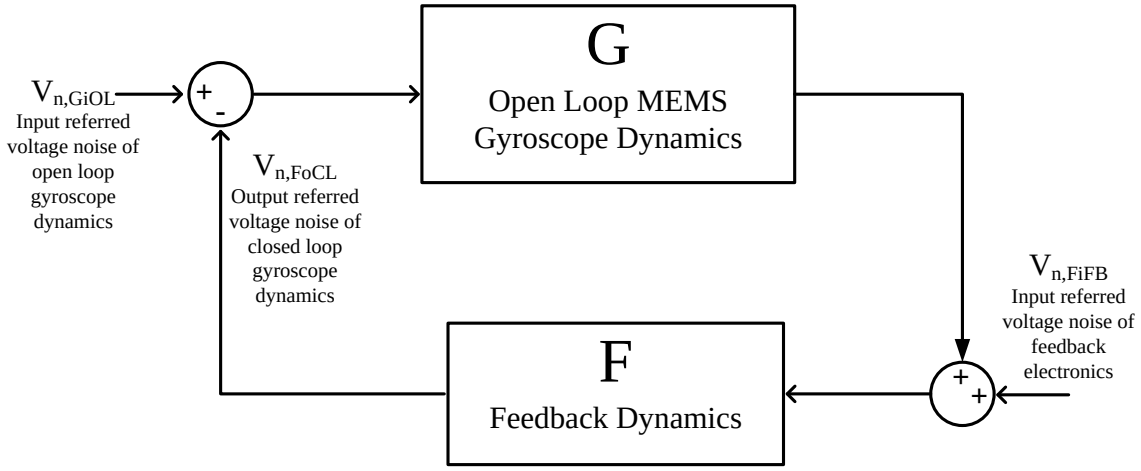

Figure 3.26: Closed loop structure for the gyroscope

Referring to Figure 3.26 output referred voltage noise of closed loop gyroscope dynamics can be written as,

$$V_{n,FoCL} = F\{G(V_{n,GiOL} - V_{n,FoCL}) + V_{n,FiFB}\} \quad 3.52$$

$$V_{n,FoCL} = \frac{FG}{FG+1}V_{n,GiOL} + \frac{F}{FG+1}V_{n,FiFB} \cong V_{n,GiOL} + \frac{1}{G}V_{n,FiFB}, \quad FG \gg 1 \quad 3.53$$

With a properly designed system with $FG \gg 1$ and with a high forward gain the noise contribution of feedback network can be neglected.

Figure 3.27 shows the feedback dynamics (F) and used components.

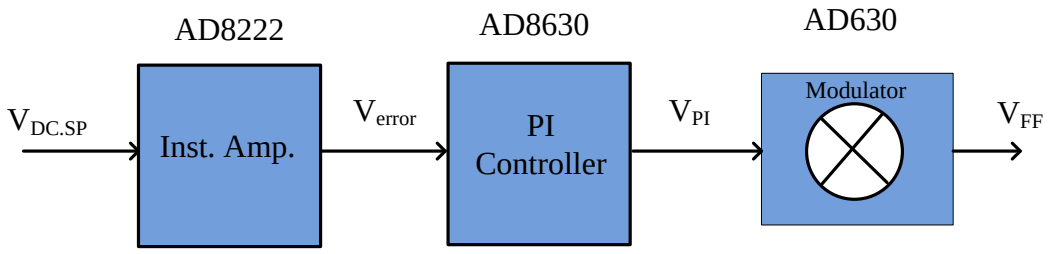

Figure 3.27: Feedback dynamics (F) with components

Referring to Figure 3.27, the noise contribution of comparator (AD822), PI controller (AD8630) and modulator (AD630) should be found. As explained in previous section noise contribution of modulators is ignored. PI controller and comparator operate at DC

so flicker noise should be included. As in low pass filter stage, AD8630 is used in PI controller, so flicker noise can be neglected.

1/f corner frequency of AD8222 is estimated as 3.5Hz using Equation 3.49. Input referred thermal noise of AD8222 with gain 1 is found as 75.43 $nV/\sqrt{Hz}$. Then total input referred voltage noise of AD8222 with gain 1 can be found by,

$$V_{n,AD8222} = \sqrt{\left(75.4\frac{nV}{\sqrt{Hz}}\right)^2 + \left(75.4\frac{nV}{\sqrt{Hz}}\right)^2 * 3.5Hz * \frac{1}{f}} = 159.94\frac{nV}{\sqrt{Hz}}, \quad f = 1Hz \tag{3.54}$$

Thermal noise of AD8630 is $22nV/\sqrt{Hz}$. Total input referred voltage noise of feedback circuit is

$$V_{n,feedback} = \sqrt{159.94^2 + 22^2} = 161.44\frac{nV}{\sqrt{Hz}} \tag{3.55}$$

For 10V proof mass potential the closed loop scale factor of the SOI gyroscope N08 using Equation 3.35 is found as 8.8 mV/^{0}/sec. Then rate equivalent input noise of feedback circuit is found as 0.066 ^{0}/hr/√Hz. Using Equation 3.53 total rate equivalent noise of the closed loop system is found as 1.356^0/hr/√Hz for SOI gyroscope N08.

3.5.3 Brownian Noise

Brownian noise is produced by Brownian motion of air molecules. It is the mechanical noise source and random motion of sensor is converted into signal by the readout circuitry. It is a kind of white noise and Brownian force can be expressed by [22]

$$F_B = \sqrt{4k_BTb}\frac{N}{\sqrt{Hz}} \tag{3.56}$$

In equation 3.56, k_B is the Boltzmann's constant, T is the ambient temperature and b is the damping coefficient. Noting that

$$\frac{b_S}{m_S} = \frac{w_S}{Q_S} \rightarrow b_S = \frac{m_S w_S}{Q_S} \tag{3.57}$$

Then Brownian force can be expressed as

$$F_B = \sqrt{4k_B T \frac{m_S w_S}{Q_S}} \tag{3.58}$$

Rate equivalent Brownian noise can be found by dividing the Brownian force to Coriolis force

$$\Omega_{rate} = \frac{\sqrt{4k_B T \frac{m_S w_S}{Q_S}}}{2m_{PM}\Omega w_D X_D} \tag{3.59}$$

For unit rate $\Omega = \pi/180 \ \ and \ A = m_{PM}/m_S$, rate equivalent noise can be found as

$$\Omega_{rate} = \frac{180}{\pi A X_D}\sqrt{\frac{k_B T}{Q_S\sqrt{k_S m_S}}}\frac{w_S}{w_D} \tag{3.60}$$

Rate equivalent noise in Equation 3.60, implies that drive displacement has direct effect on noise. Increasing the drive displacement increases the scale factor which reduces the rate equivalent noise. Other parameter is the A, again determines the scale factor directly, for a more sensitive gyroscope A should be as large as possible. Quality factor and mass are other parameters that determine rate equivalent noise. Since they are in square root their effect does not directly affect noise, however with wafer level vacuum packaging the quality of sense mode can be increased 5-10 times (quality of 15000-30000) which significantly reduces rate equivalent noise. Suppressing the Brownian noise is one of the major goals of vacuum packaging of MEMS gyroscopes. If drive and sense resonance frequencies are close to each other that reduces the noise however during actual operation sense and drive resonance frequencies are close to each other and ratio is approximately unity. ($w_S \cong w_D$, already)

For SOI gyroscope N08, rate equivalent Brownian noise can be calculated for 10V proof mass potential as

$$\Omega_{rate,N08} = \frac{180}{\pi * 0.385 * 4 * 10^{-6}\mu m} * \sqrt{\frac{1.38 * 10^{-23} m^2 kgs^{-2}K^{-1} * 300K}{3029\sqrt{1224\frac{N}{m} * 1.668 * 10^{-7} kg}}} * \frac{13.64kHz}{13.9kHz} = 1.285^0/hr/\sqrt{Hz} \quad 3.61$$

Total output noise can be found by combining mechanical Brownian noise and electronics noise. This is calculate ed for SOI gyroscope N08 as

$$\Omega_{n,totalN08} = \sqrt{\Omega_{n,electronics}^2 + \Omega_{n,mechanical}^2} = \sqrt{1.356^2 + 1.285^2} = 1.87^0/hr/\sqrt{Hz} \quad 3.62$$

This is the theoretical white noise limit for the SOI gyroscope N08 with 10V proof mass potential and 4μm drive displacement. Note that both the electronics and mechanical noise depends on drive displacement, drive displacement can be used to reduce noise. Increasing the drive displacement reduces the rate equivalent noise; limit comes from the linearity limit of the gyroscope for drive displacement.

3.6 Summary

This chapter presents the readout and closed loop control electronics studied in this work. The capacitive and resistive preamplifiers are studied then the procedure followed to extract the parameters of the gyroscope through resonance tests is explained. Closed loop drive and sense mode controller design is presented. The design procedure can be summarized as; first obtain the open loop transfer function with simplified gyro model, second optimize the PI parameters using open loop model and lastly verify the design in SIMULINK. Design of quadrature control electronics is explained, the design procedure is similar to force feedback. Open and closed loop electronics noise calculations and mechanical noise calculations are done and white noise limit of the sample SOI gyroscope N08 is found.

CHAPTER 4

FABRICATION OF MEMS GYROSCOPES

The fabrication process used in this study is based on SOG (silicon on glass) process. The main idea behind the process is fabricating first glass wafer with recesses and electrical interconnects, then bonding it to the silicon device layer. Device layer can be formed prior to bonding or after bonding. Since the gyroscope is a capacitive sensor constructing the device layer on an insulating layer is significant. By this way unwanted parasitic capacitances and electrostatic levitation force are minimized [22].

Previously the gyroscopes developed at METU were fabricated with SOG process in which the device layer was formed after anodic bonding of silicon wafer to processed glass wafer. That process has its own problems; the process was switched to SOG based SOI process in which device layer is formed prior to bonding of silicon and glass wafers. The organization of this chapter is as follows, section 4.1 describes the SOG based SOI process with description of SOI wafer to glass anodic bonding. Section 4.2 presents the SOG process with its problems then Section 4.3 makes a comparison between SOG based SOI and SOG processes. Section 4.4 presents the effects of BHF on contact resistance. Finally section 4.5 gives a summary of the chapter.

4.1 SOG based SOI Process

The current SOG based SOI process starts with an empty glass wafer. The first step is the anchor formation; these anchors will be anodically bonded to silicon device layer. As mask material photoresist (PR) is not sufficient, because glass etch is performed in hydrofluoric acid (HF) and etch rate of HF to PR is high. Chromium/Gold (Cr/Au) is

used as masking material for glass etch. In order to Cr to have a good adhesion to polished glass surface, glass surface should be roughed. Adhesion of Cr/Au is important in the sense that undercut will be lower with a better quality film. Undercut can be defined as lateral etching of etchants while etching in the vertical direction. So, the first process step is roughing the polished glass surfaces with BHF (HF is diluted with ammonium fluoride, NH_4F so that etch rate is reduced), Figure 4.1 shows conceptual BHF applied glass surface. It is known that metal adhesion to rough surfaces is higher than that of polished surfaces.

Second step is the evaporation and patterning of Cr/Au on glass surface. Cr/Au is used instead of only Au, since Cr is used as adhesion layer. Glass etch mask (anchor mask) is formed with Cr/Au at this point (Figure 4.2).

Third step is the glass etch. Glass is etched in pure HF. Since the etching is a chemical process, etch rate highly depends on ambient temperature. Etch rate should be checked at the start of the process. Glass etch process is isotropic and known to have high undercut ratios. 1:1.3 undercut is considered to be sufficient. The isotropic etching behavior of HF is useful for the process since the next step is the Cr/Au evaporation. With vertical sidewalls step coverage of Cr/Au will not be good, isotropic etching provides step coverage on all around the wafer. Figure 4.3 shows etched glass surface.

At the fourth step glass etch mask Cr/Au is stripped, and the wafer is prepared for the next evaporation. BHF is applied to glass wafer again to ensure surface roughness and second Cr/Au evaporation is done (Figure 4.4). As the fifth step this metallization is patterned to form electrical interconnects (Figure 4.5). Process of glass wafer with recesses and electrical interconnects is finished. In other words glass is ready for anodic bonding.

Glass wafer process is same as for both the previous SOG and SOG based SOI processes.

The process of device layer starts with an SOI wafer and device layer is formed on SOI wafer by DRIE (Deep Reactive Ion Etching). Oxide layer of SOI wafer acts as an etch stop layer during DRIE (Figure 4.6 and Figure 4.7). DRIE or bosch process switches

between passivation and etch cycles to form high aspect ratio structures. DRIE coats polymer in the passivation cycle. Prior to anodic bonding, passivation polymer of the DRIE should be removed. Otherwise anodic bonding may be unsuccessful. DRIE polymer is removed in piranha solution (1:1 Sulfuric Acid : Hydrogen Peroxide, H_2SO_4:H_2O_2). The wafer should be checked under microscope to observe whether the polymer is completely removed or not after each cleaning step. It should be taken into account that during piranha native oxide is grown on silicon substrate.

The next step is the anodic bonding of processed glass and SOI wafers. It is important to remove the grown oxide on silicon substrate, if not ohmic contact between silicon and interconnect metallization will not be formed. Just before anodic bonding native oxide on silicon device layer is removed with BHF. Surface tolerance of anodic bonding is in the order of nanometers [53] and cleaning of bonding surfaces is extremely important. For that reason the processed glass wafer is also cleaned in 1:1 piranha solution. After cleaning of processed glass and silicon wafers they are aligned and anodically bonded (Figure 4.8). A more detailed description of anodic bonding will be given in the following section.

After anodic bonding first the handle layer of the SOI wafer is completely etched. Handle layer can be removed by wet or dry etch. In this study handle layer is removed with DRIE (Figure 4.9). Oxide layer acts as an etch stop layer during dissolving the handle part of SOI.

The final step is the removal of SOI oxide layer which was used as an etch stop layer. Oxide layer can be removed wet (BHF) or dry (RIE). When removed by BHF the time of etch should be adjusted well since BHF also etches the glass wafer. SOG based SOI process finishes with removal of oxide (Figure 4.10).

Figure 4.1 - Figure 4.10 provides the steps of SOG based SOI process.

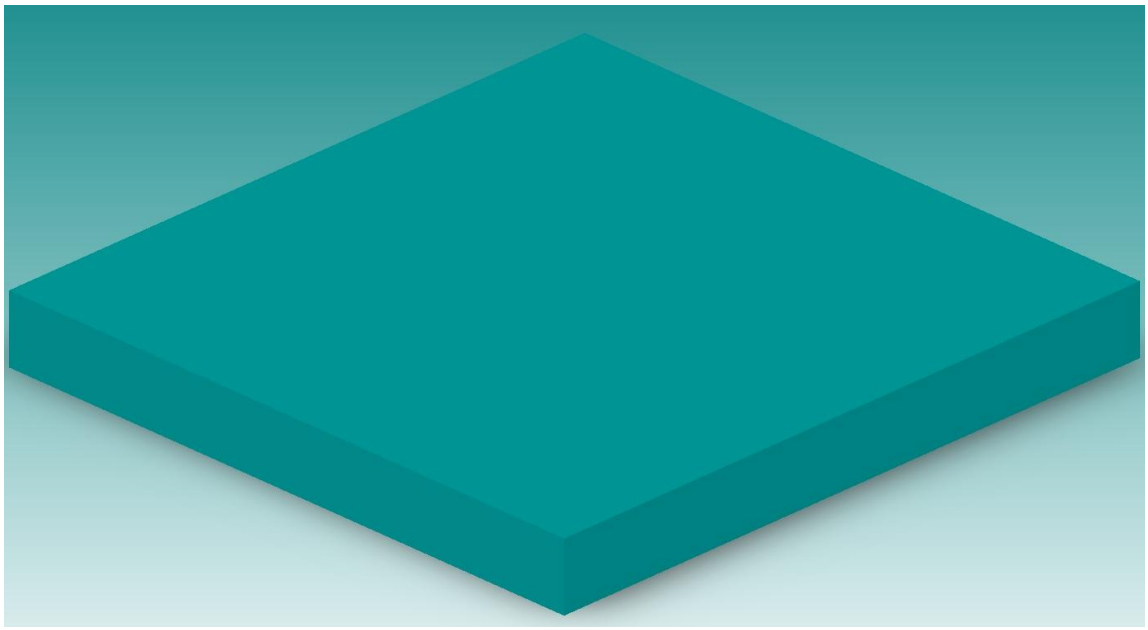

Figure 4.1: Step 1. Apply BHF to glass wafer

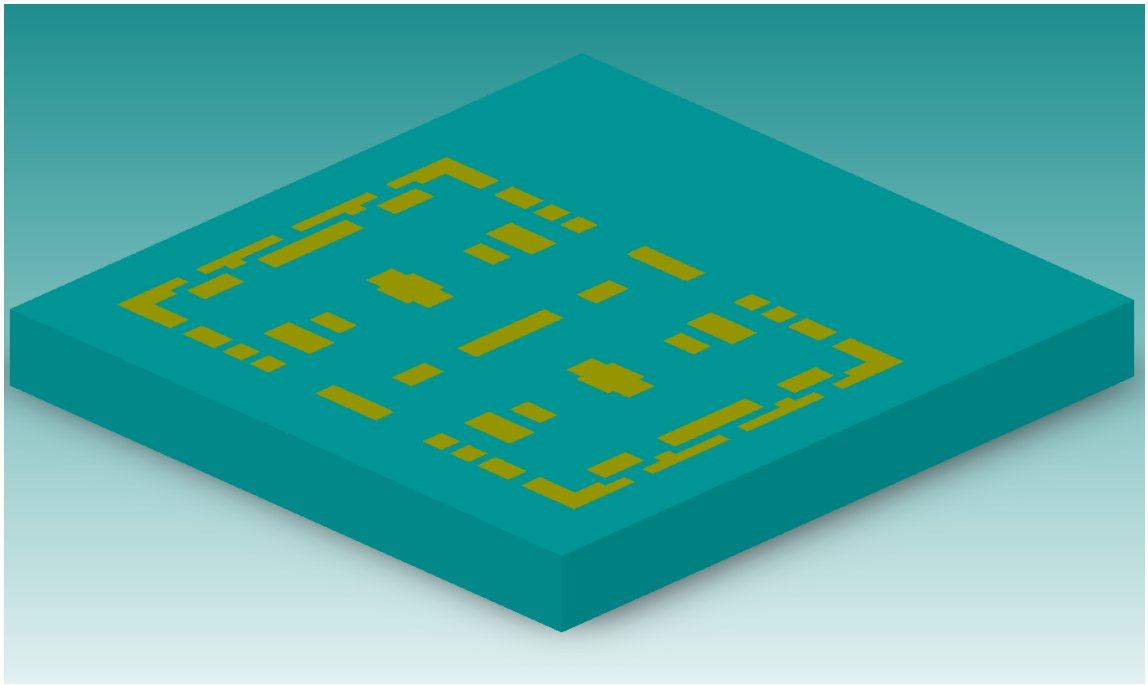

Figure 4.2: Step 2. Coat and pattern Cr/Au for glass anchor mask

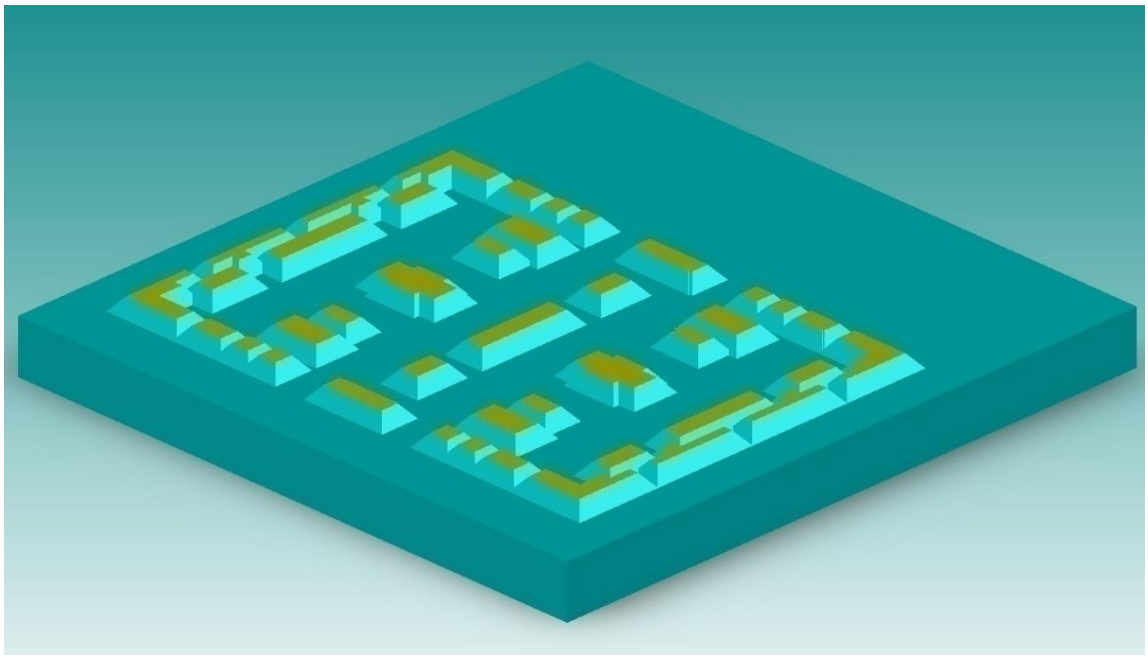

Figure 4.3: Step 3. Perform glass anchor etch in HF

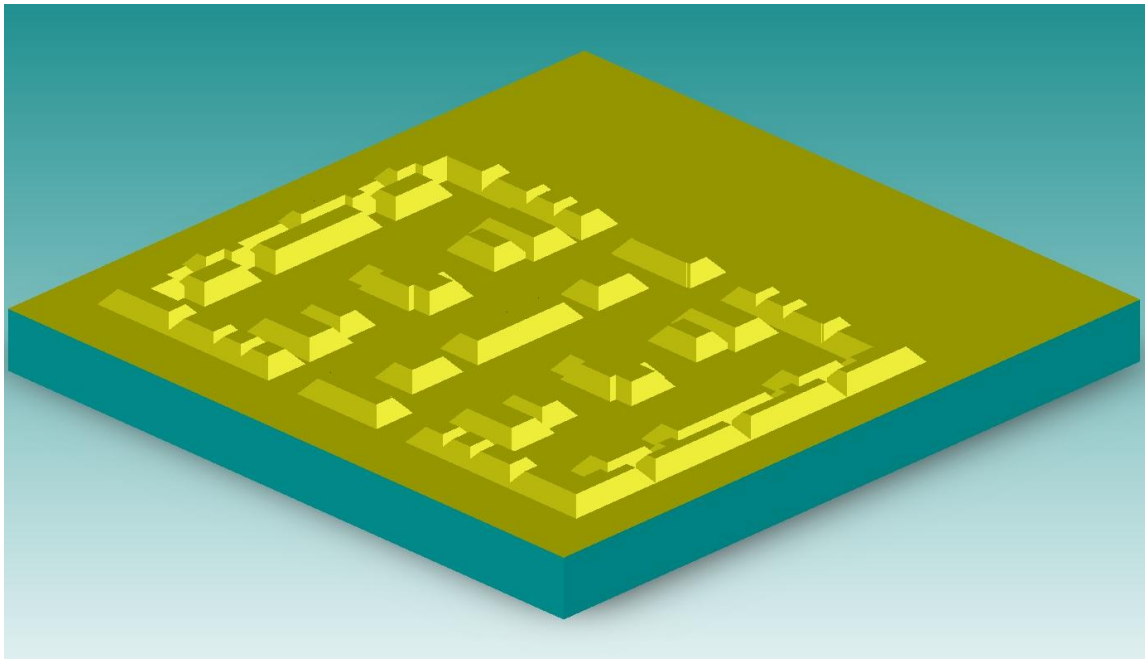

Figure 4.4: Step 4. Strip first Metallization and coat 2nd Cr/Au for interconnect metallization

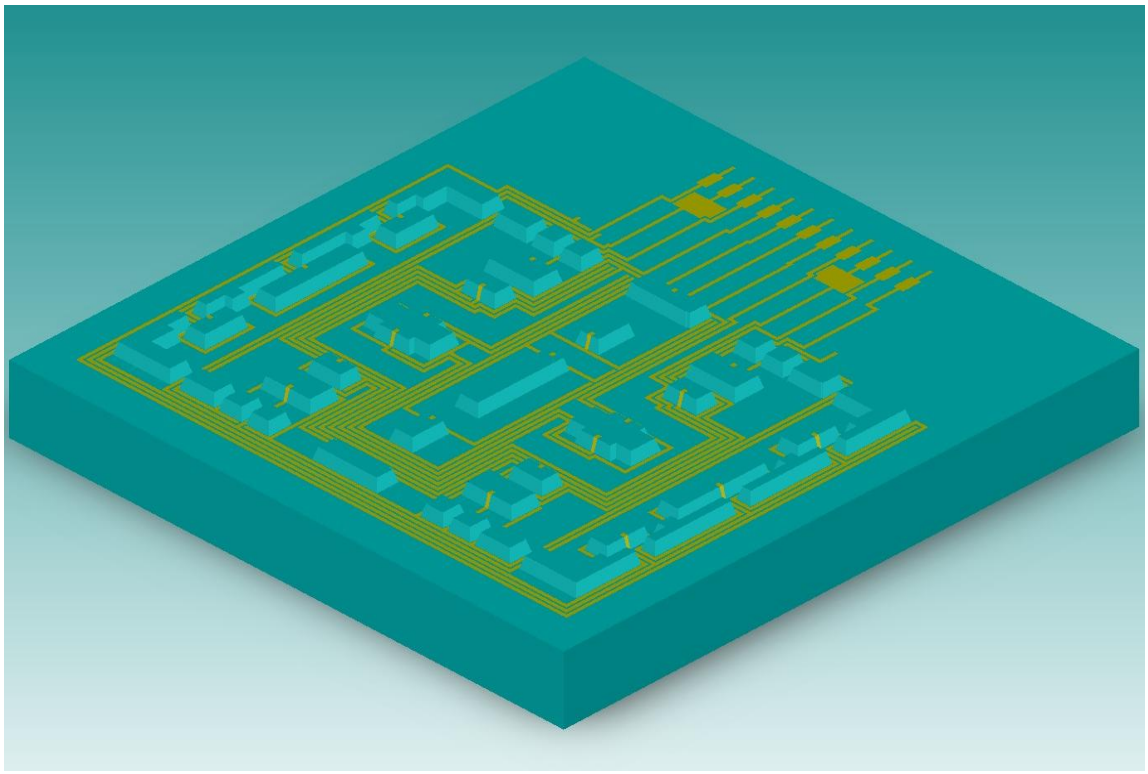

Figure 4.5: Step 5. Pattern the coated Cr/Au for interconnect metallization, end of glass wafer process

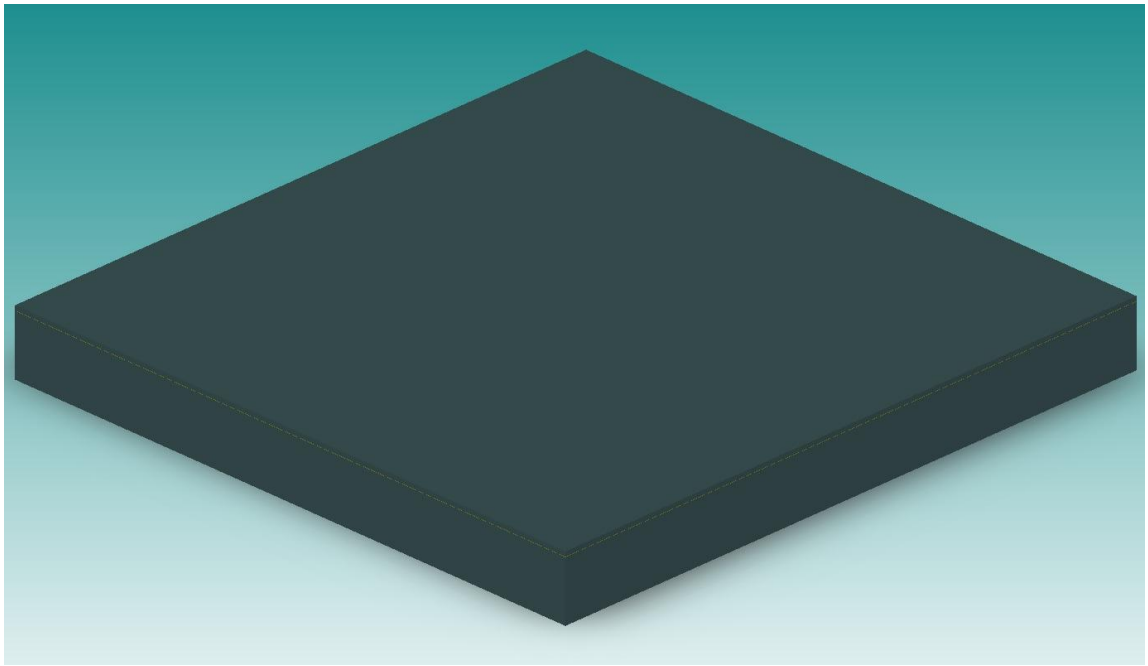

Figure 4.6: Fabrication of device layer, take an SOI wafer

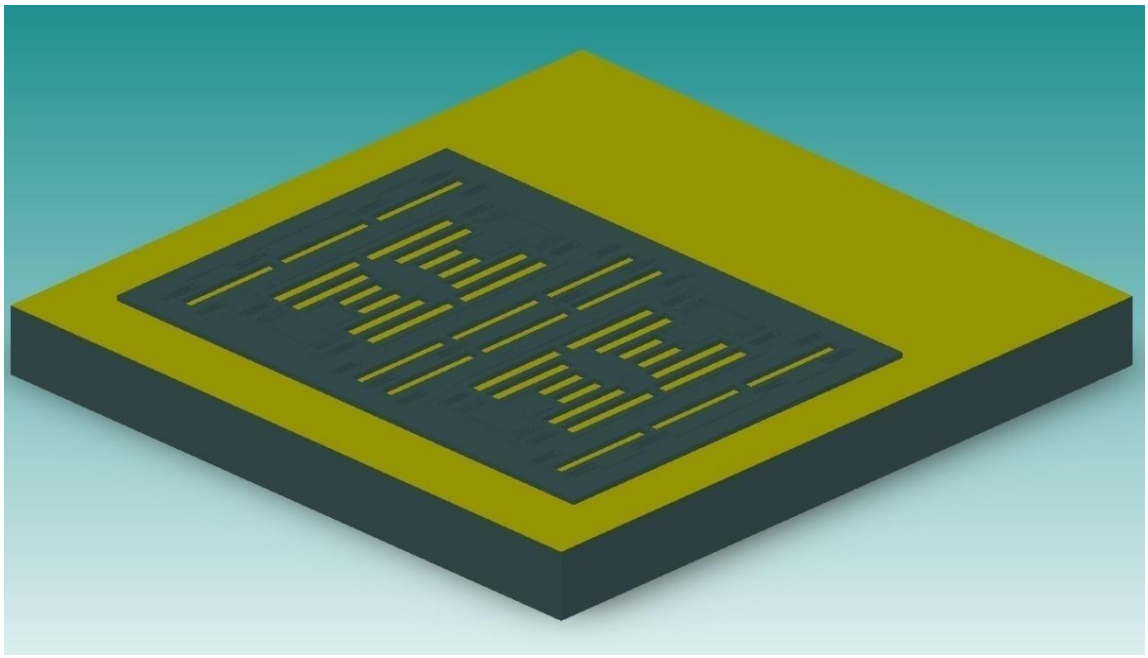

Figure 4.7: Step 6. Pattern the SOI wafer with PR and form the device layer

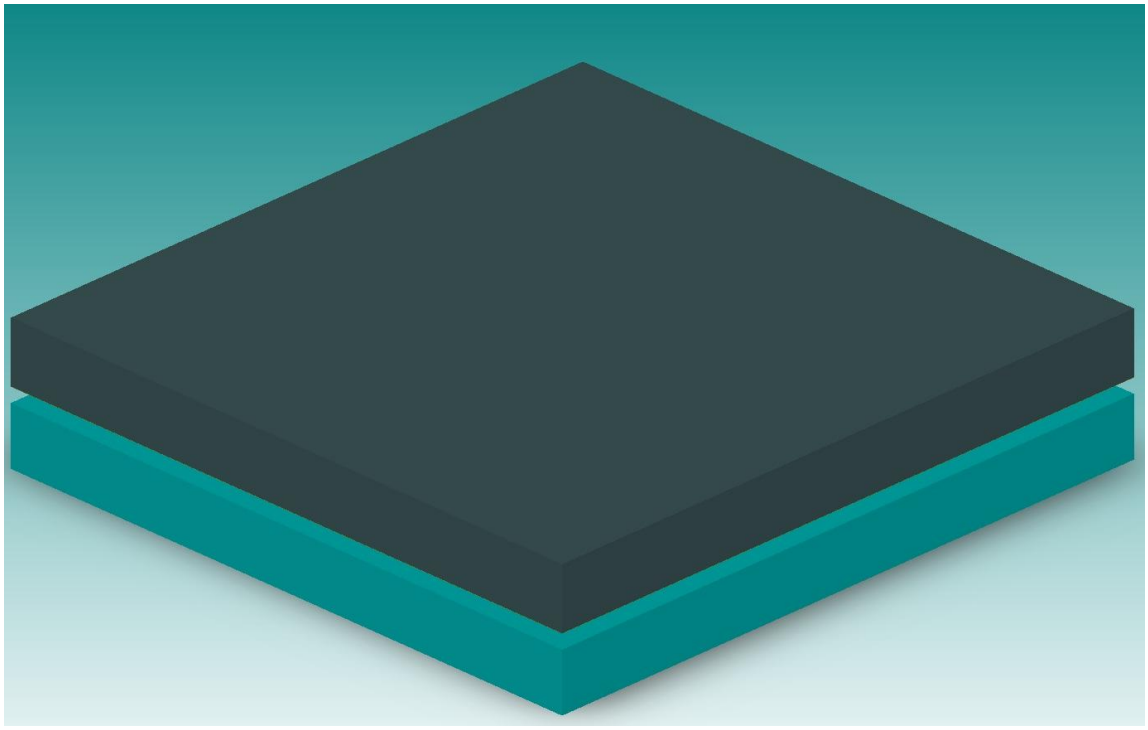

Figure 4.8: Step 7. Anodically bond processed SOI and glass wafers

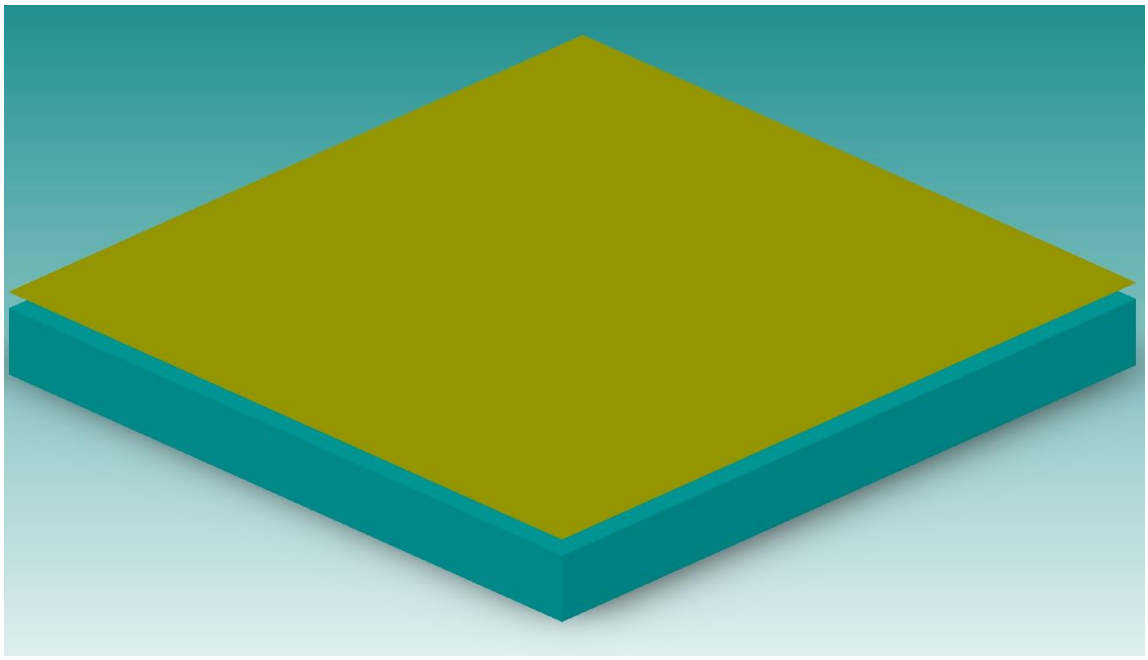

Figure 4.9: Step 8. Remove the handle part of SOI wafer

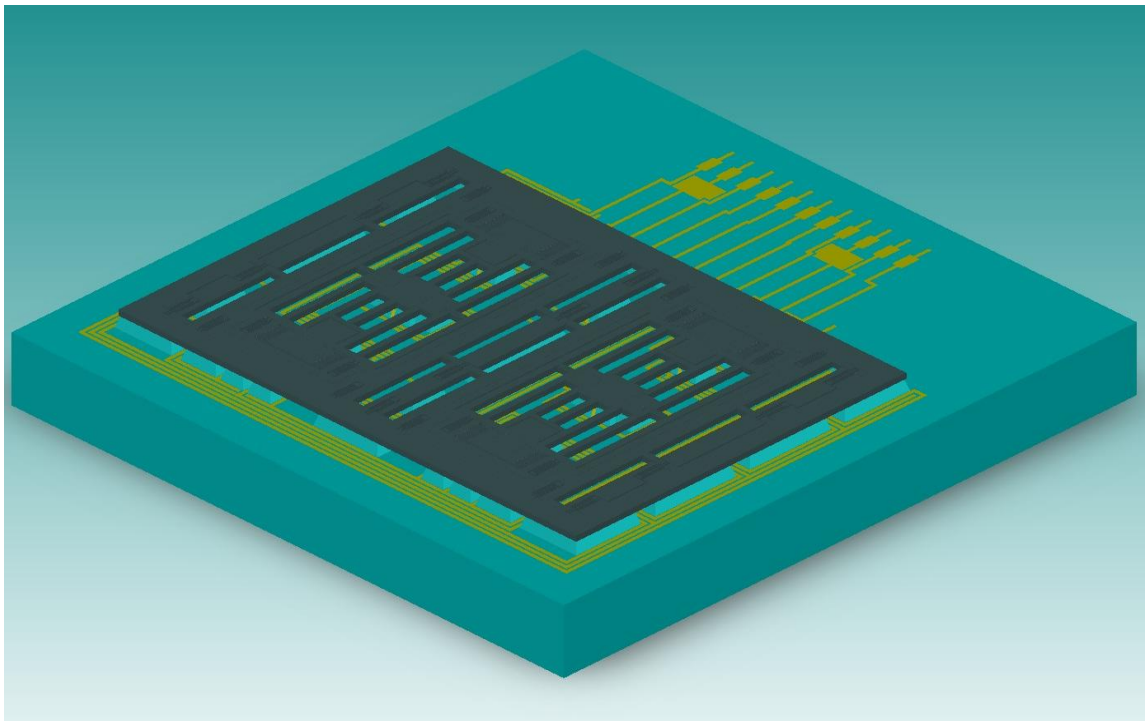

Figure 4.10: Step 9. Remove the oxide of SOI wafer, final step

4.1.1 Anodic Bonding of SOI and Glass Wafers

Figure 4.11 shows a standard anodic bonding scheme.

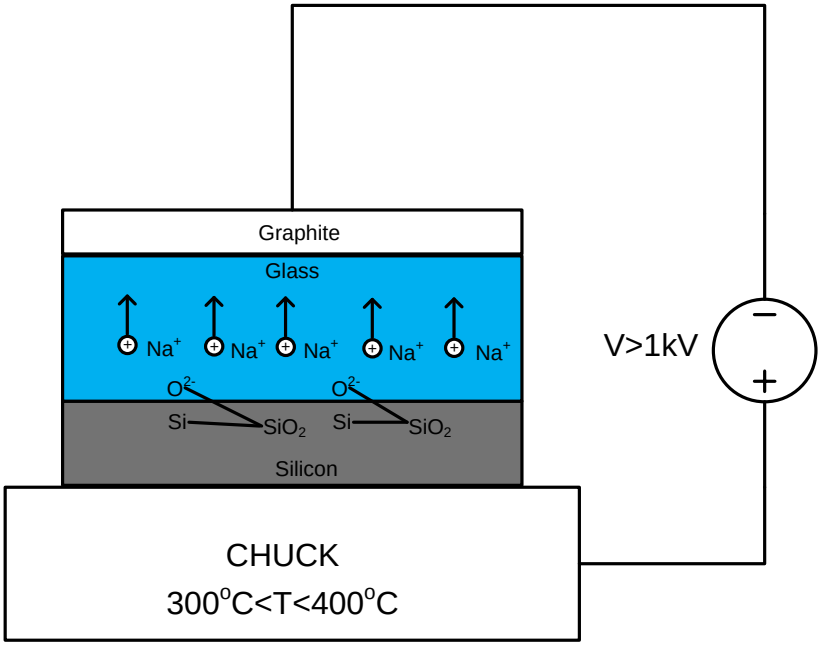

Figure 4.11: Standard anodic bonding scheme

In standard anodic bonding silicon and glass wafers are brought into intimate contact with applied pressure and electrostatic force, and heated to temperatures 300-400 ^{0}C. The glass wafer used for anodic bonding is intentionally doped with sodium (Na^{+}) ions, at the elevated temperatures glass wafer becomes a weak conductor and Na^{+} ions leave oxygen (O^{2-}) ions at the bond interface due to applied high potential (>1kV). The oxygen ions chemically interact with silicon atoms and form covalent bonded silicon dioxide (SiO_2) which is a very high quality bond.

Bonding of SOI wafer to glass is performed in the same manner but the underlying principles should be understood. Figure 4.12 shows the SOI to glass wafer anodic bonding configuration. The system can be modeled as two capacitors in series. The first capacitance C_1 is formed between graphite and device layer of SOI. The second capacitance C_2 is formed between device and handle layer of SOI. The thickness of oxide is 2µm, the thickness of glass wafer is 500µm. So it can be concluded that $C_2 >> C_1$ and these capacitors are connected in series which implies potential across C_1 is

much larger than that of C_2 (V_1>>V_2). Almost all of the applied potential for anodic bonding occurs between device layer of SOI and glass. So anodic bonding of glass and SOI wafer can be done as standard anodic bonding, and it is verified that the anodic bonding quality of SOI is same as standard anodic bonding.

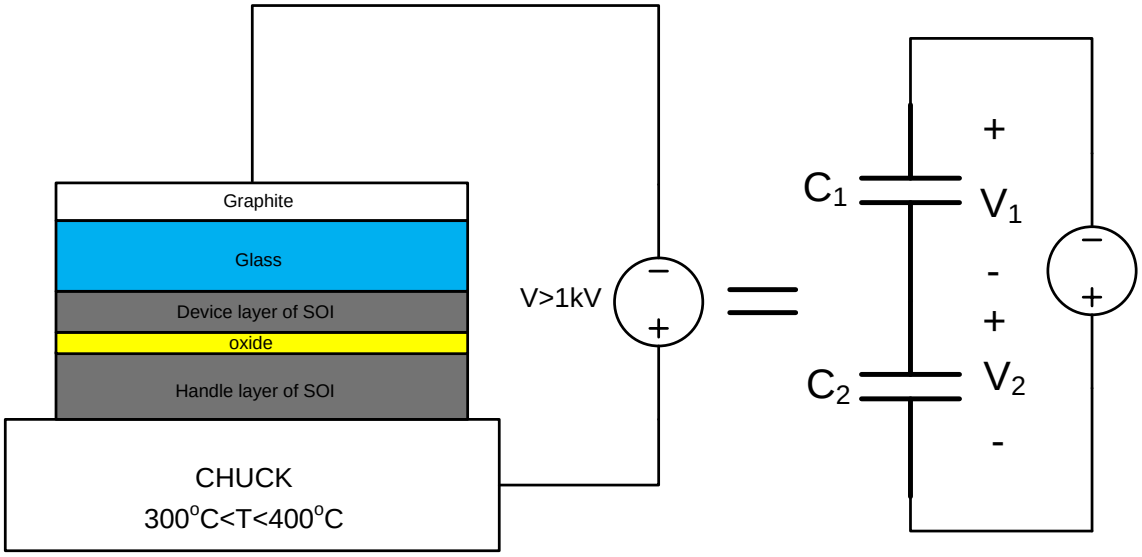

Figure 4.12: SOI to glass wafer anodic bonding configuration

4.2 SOG Process

The glass process is same for both SOG based SOI and SOG processes. They are different in the device layer formation stage, Figure 4.13 - Figure 4.17 shows the process flow of SOG after glass wafer process.

In SOG process 100µm thick silicon wafer is taken and shield metal is coated and patterned on silicon wafer (Figure 4.14). The mask is the inverse of glass anchor mask, i.e. only the regions to be bonded on silicon are opened. Then anodic bonding of silicon and glass wafers is performed (Figure 4.15). BHF should be applied to silicon wafer before anodic bonding to ensure ohmic contacts. In SOG process device layer is defined after anodic bonding (Figure 4.16). As the final step shield metal and DRIE polymer is removed and the device is formed (Figure 4.17). Shield metal is used to reduce the notch effect during DRIE.

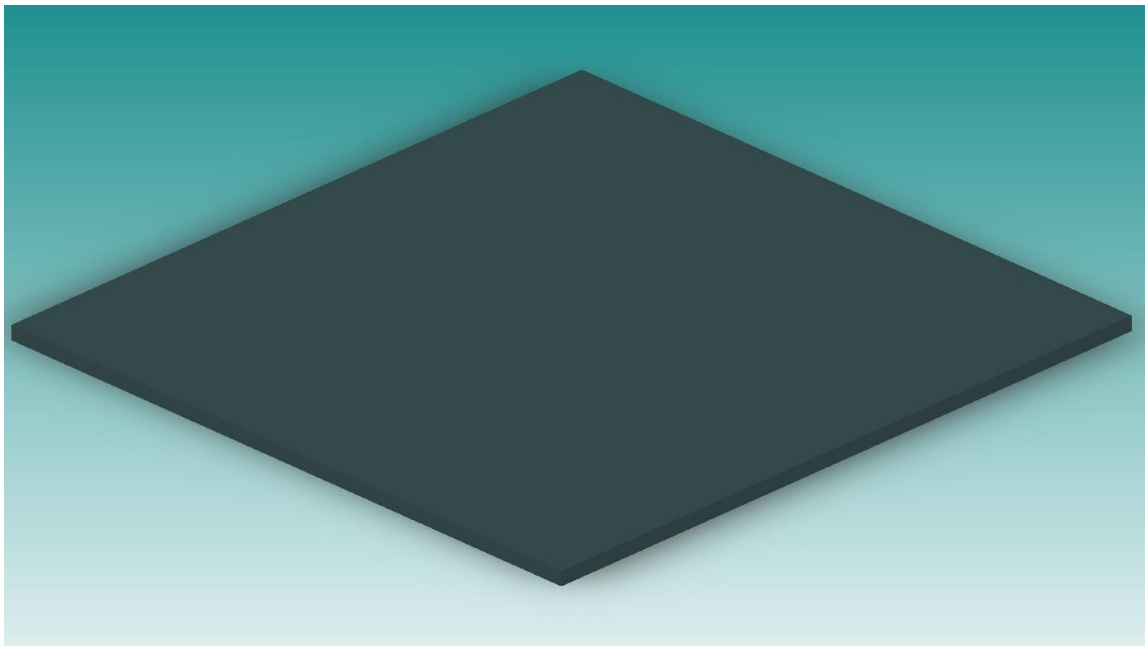

Figure 4.13: 100µm Thick Silicon Wafer

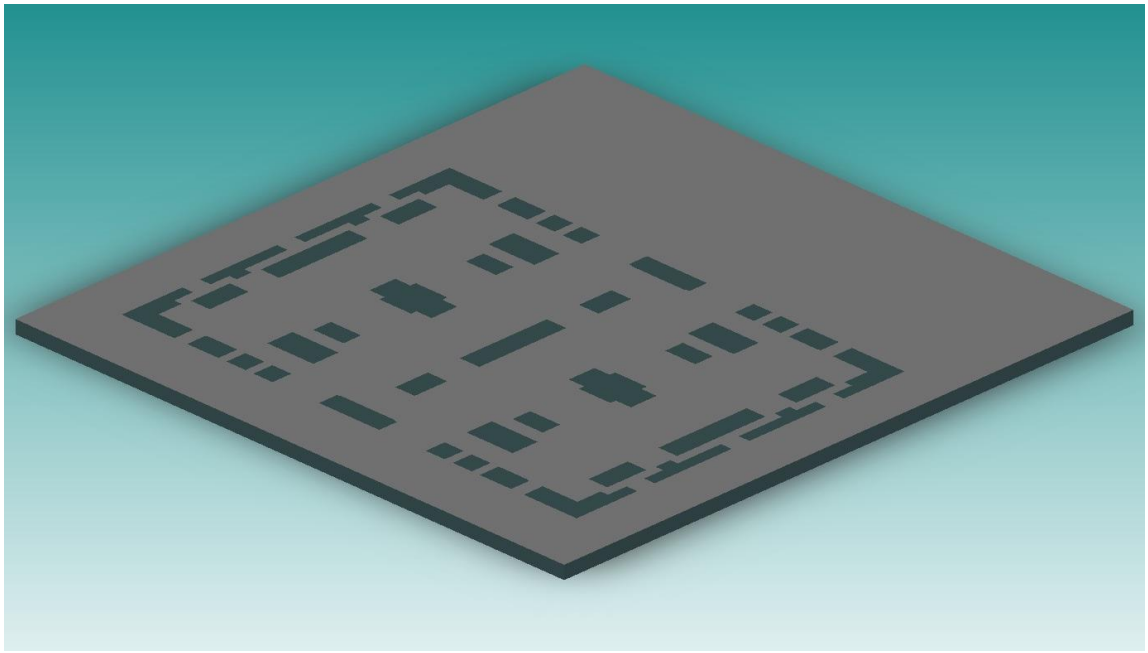

Figure 4.14: Step 6 of SOG. Coat and pattern DRIE shield metal

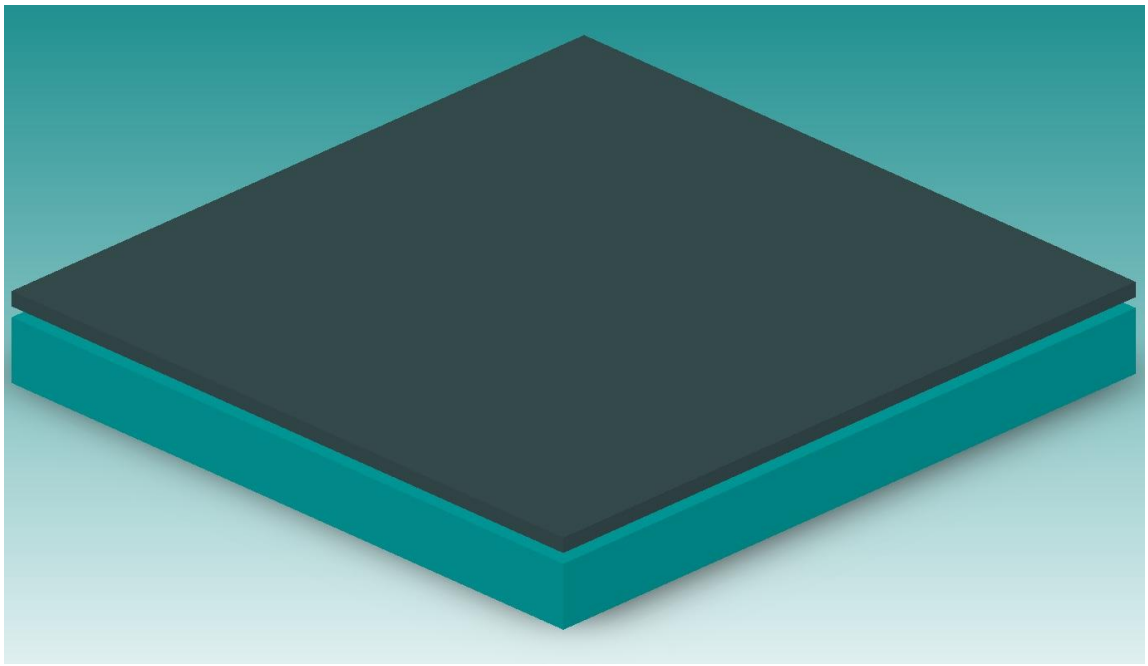

Figure 4.15: Step 7 of SOG. Anodically bond silicon and glass wafers

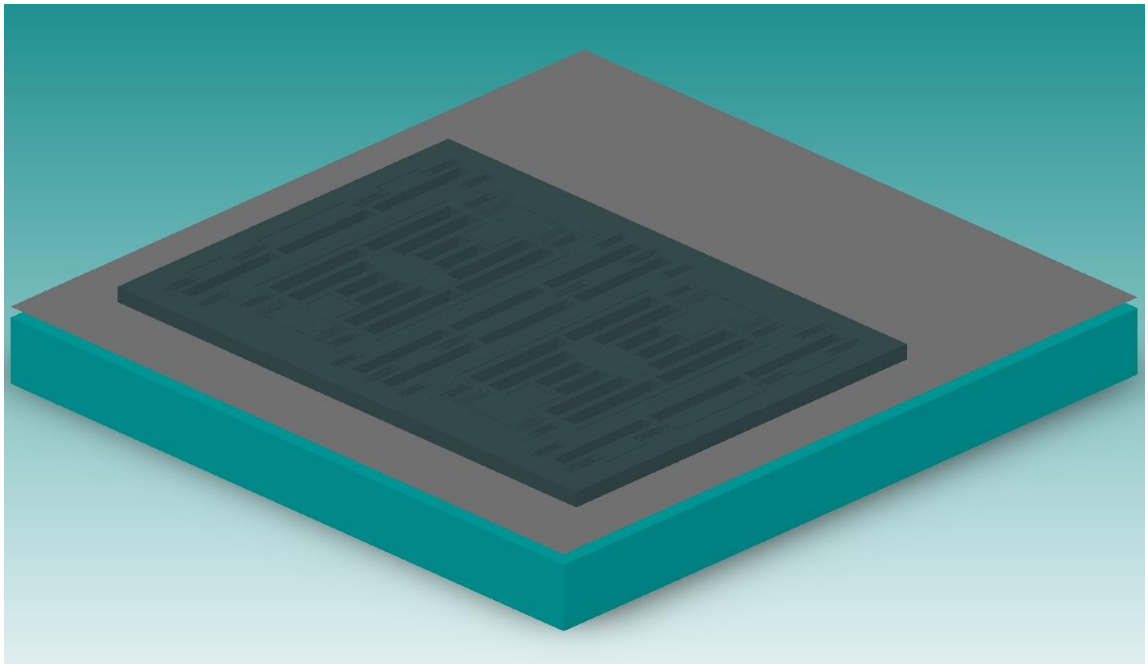

Figure 4.16: Step 8 of SOG. Define structural layer on silicon wafer

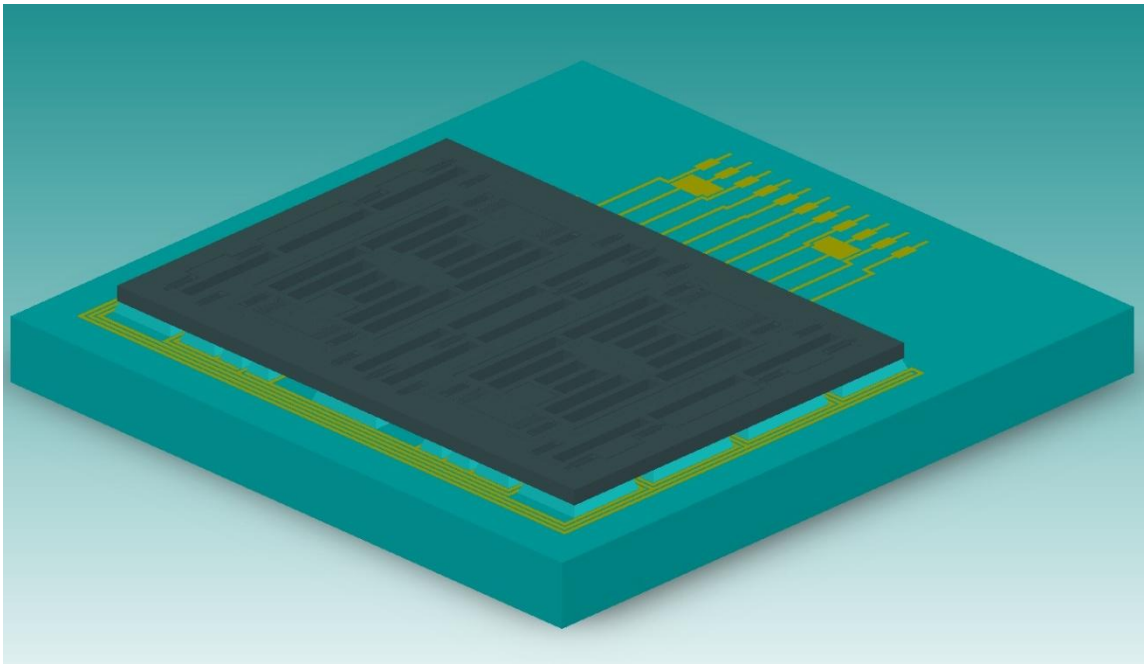

Figure 4.17: Step 9 of SOG. Remove shield metal and DRIE polymer, final step of SOG process

Performing DRIE on bonded silicon wafer was the main problem of SOG process. During the etch cycle of DRIE heat is generated due to chemical etching process and the generated heat should be removed. To better visualize the heating effect DRIE operation is summarized in Figure 4.18. As seen first polymer is coated everywhere, then with vertical ion bombardment the polymer is removed in vertical direction. Final step is the etching of silicon with fluorine, this is an exothermic reaction and the excessive heat is generated at this point of the process. As a general guideline DRIE etch rate increases with increasing temperature however DRIE polymer coat rate decreases with increasing temperature.

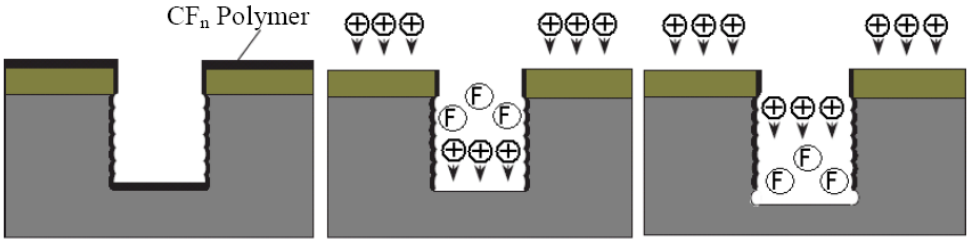

Figure 4.18: DRIE passivation and etch sequence

When the silicon wafer is bonded to glass wafer the thermal time constant of the system increases due to high thermal resistance of glass wafer. As the etch proceeds, the thermal resistivity of silicon wafer dramatically increases and the silicon wafer becomes hotter. As the substrate temperature increases DRIE starts to etch on sidewalls. At the end of the DRIE process the gaps are widened, 2µm designed gaps are measured to be 4µm. To solve this problem DRIE etch is not performed at once; instead time breaks are used to cool the wafer [52].

4.3 Comparison of SOG based SOI and SOG Processes

The main difference between SOG based SOI and SOG processes is the DRIE, in SOG based SOI process DRIE is performed on SOI wafer before anodic bonding. However, in SOG process DRIE is performed after anodic bonding. Device layer thicknesses are 35µm for SOG based SOI and 100µm for SOG process. Handling of 100µm thick silicon wafer was very hard, almost half of the wafers were lost during process. On the other hand handling of SOI wafer is easy, since the total thickness of SOI wafer is almost 500µm (35µm device layer + 450µm handle layer + 2µm oxide layer). In SOG gyroscopes proof mass potentials of 30V-40V was used, however this value is decreased to 10V-15V for SOI gyroscopes. In SOG based SOI process it is possible to obtain aspect ratio of 35:1, in SOG typically 20:1 to 30:1 is obtained. SOG based SOI process seems to be better in the stated aspects.

Oxide layer of SOI wafer is used as an etch stop layer in SOG based SOI process, but the devices are affected by the so called notch effect. Notch occurs due to loading effect in DRIE. Etch in wider openings goes faster compared to narrow openings (loading effect). When the etch stops on oxide layer in wider openings, the oxide is charged due to vertical ion bombardment and notch effect occurs. Figure 4.19 shows SEM images of Loading and notching effects. Notching effect is inevitable, however it can be reduced by adjusting etch period carefully. Since the backside of SOG silicon wafer is coated with shield metal notching effect is not directly observed in SOG wafer.

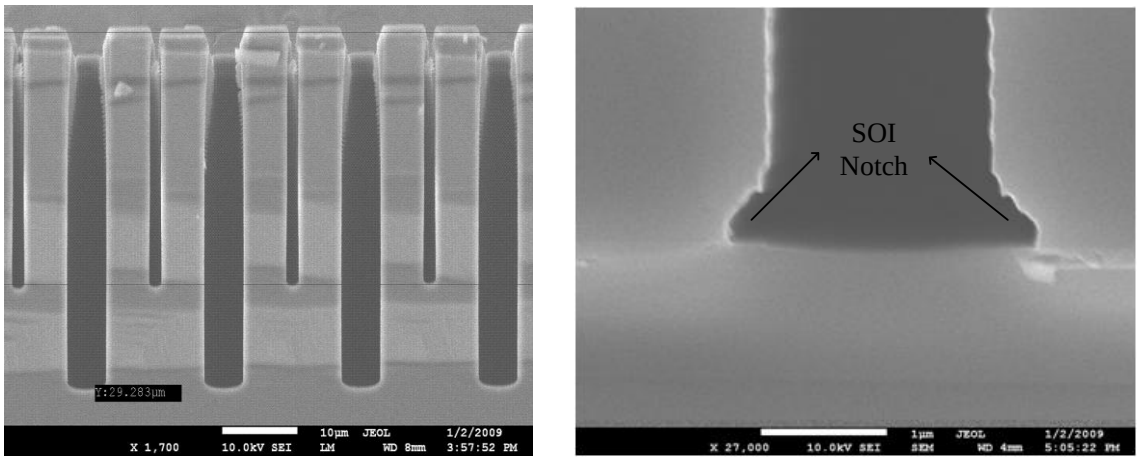

a b

Figure 4.19: Loading effect of DRIE (a) and Notching effect (b)

The etch profile of SOG based SOI is expected to be better than SOG due to DRIE conditions and lower device layer thickness, i.e. etch through 35µm is expected to be more stable than etch through 100µm.

Figure 4.20 and Figure 4.21 show the photographs of fabricated SOG gyroscopes from frontside and backside, respectively. DRIE damage due to overheating of substrate can be observed from both frontside and backside. Spring view from backside illustrate that the springs are thinned so much. The views indicate that the gap of the gyroscope widens from top to bottom. While switching to SOG based SOI process the main goal was a more stable DRIE etching. The heating problem encountered in SOG process is not observed in SOG based SOI since the DRIE is performed prior to anodic bonding. Only problem is the DRIE notch but it occurs only at the end of etch though a few micrometers.

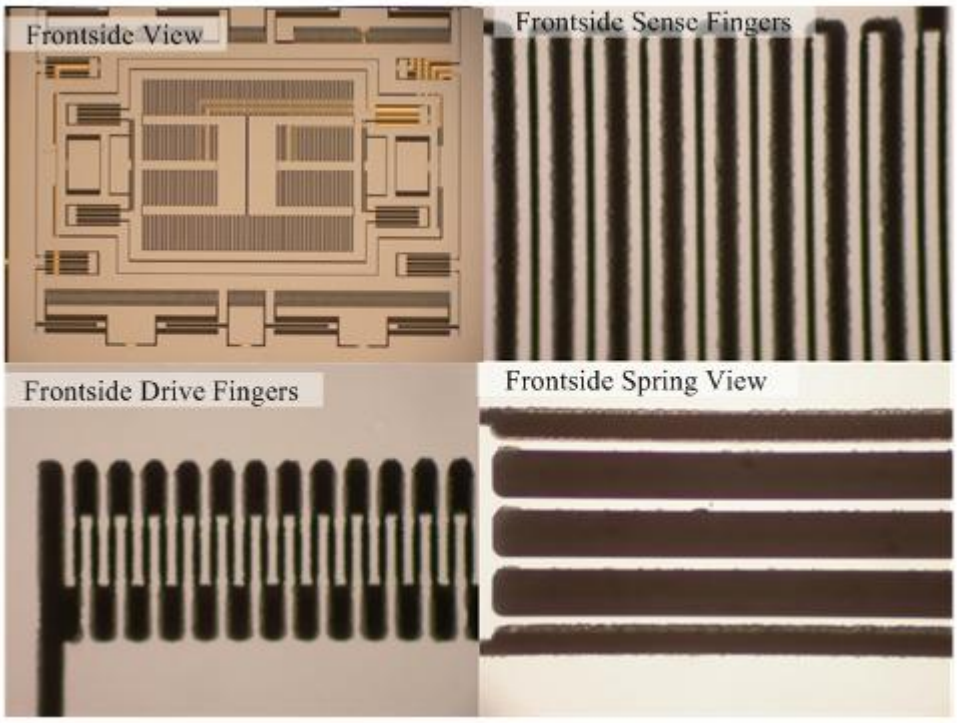

Figure 4.20: Frontside view of SOG gyroscope

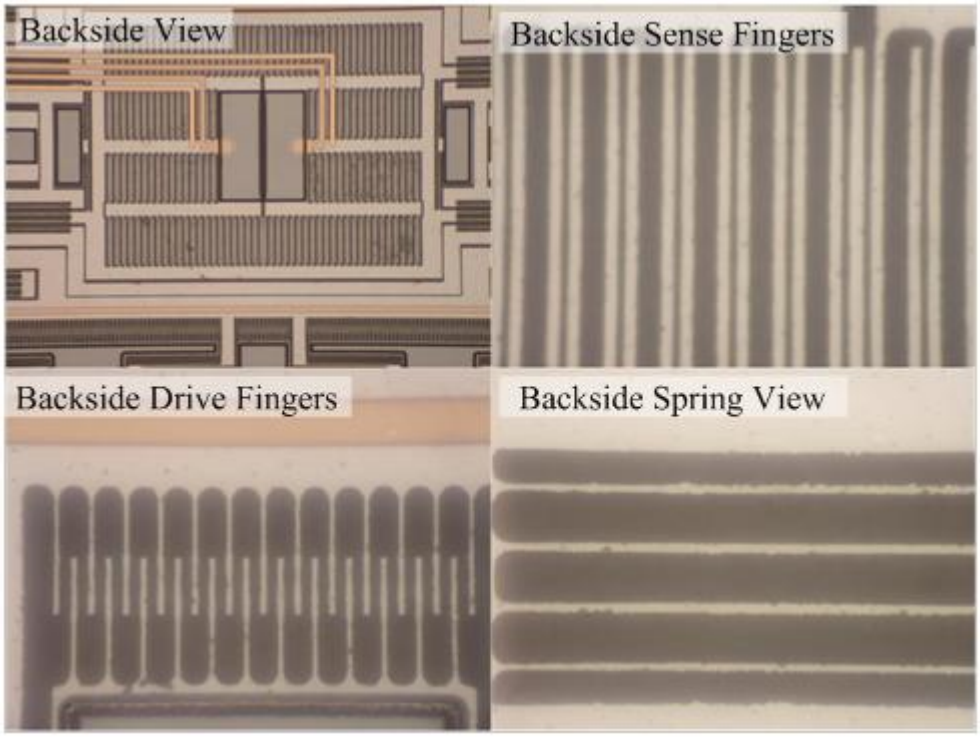

Figure 4.21: Backside view of SOG gyroscope

Figure 4.22 provides the frontside view of SOI gyroscope.

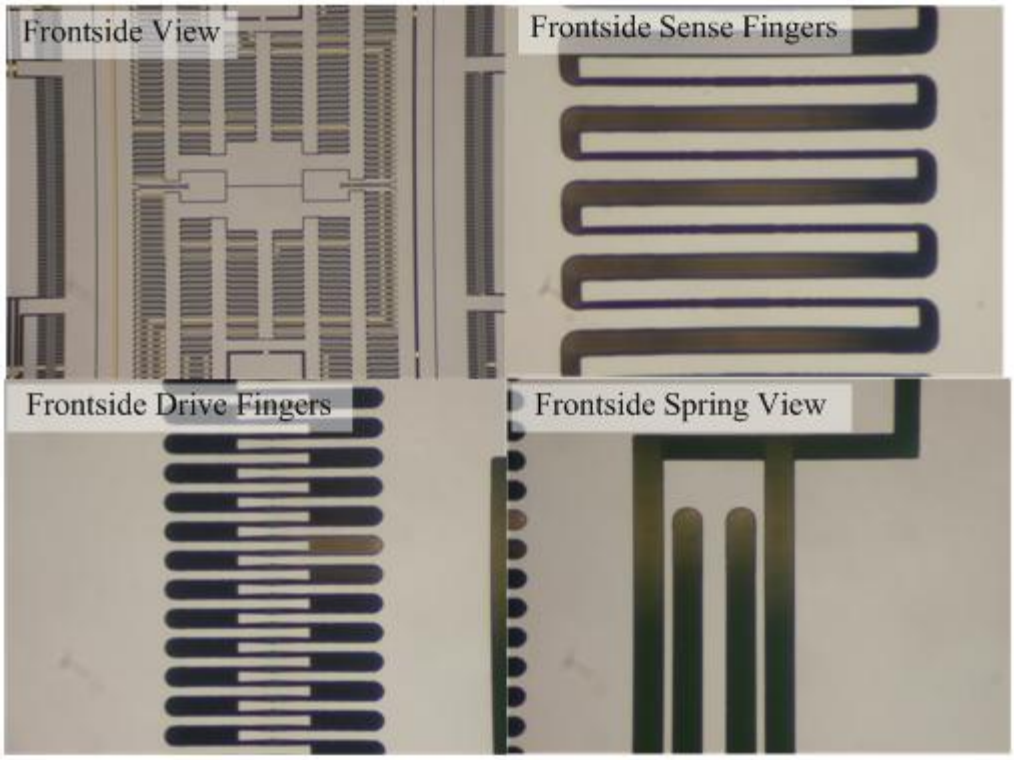

Figure 4.22 Frontside view of SOI gyroscope

As seen in Figure 4.22 the views of SOI gyroscopes are better than that of SOG gyroscopes. Figure 4.23 shows SEM images taken from sense fingers from SOG and SOI gyroscopes.

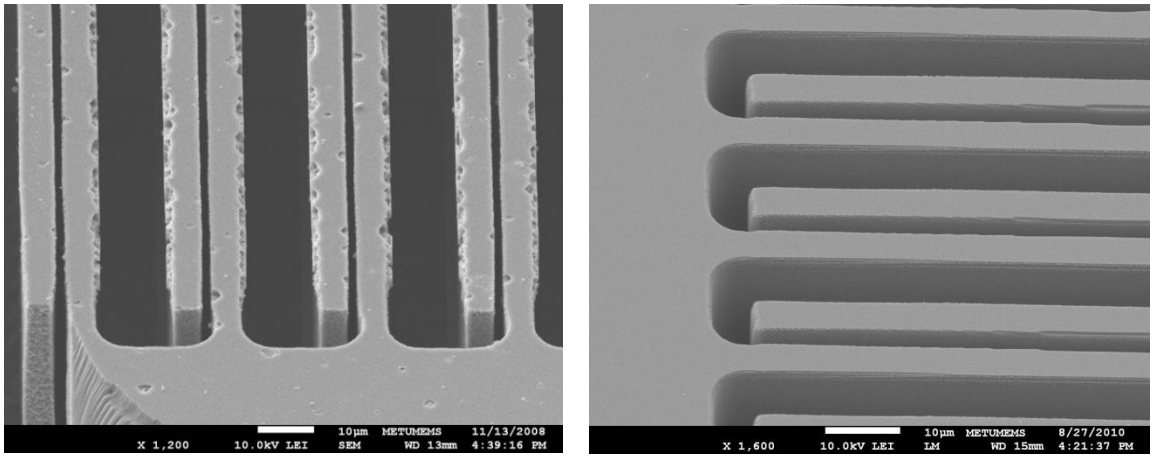

a SOG sense finger b SOI sense finger

Figure 4.23 SEM images of SOG (a) and SOI (b) gyroscopes

It is obvious that in SOG process sense finger destruction is higher than SOI finger destruction.

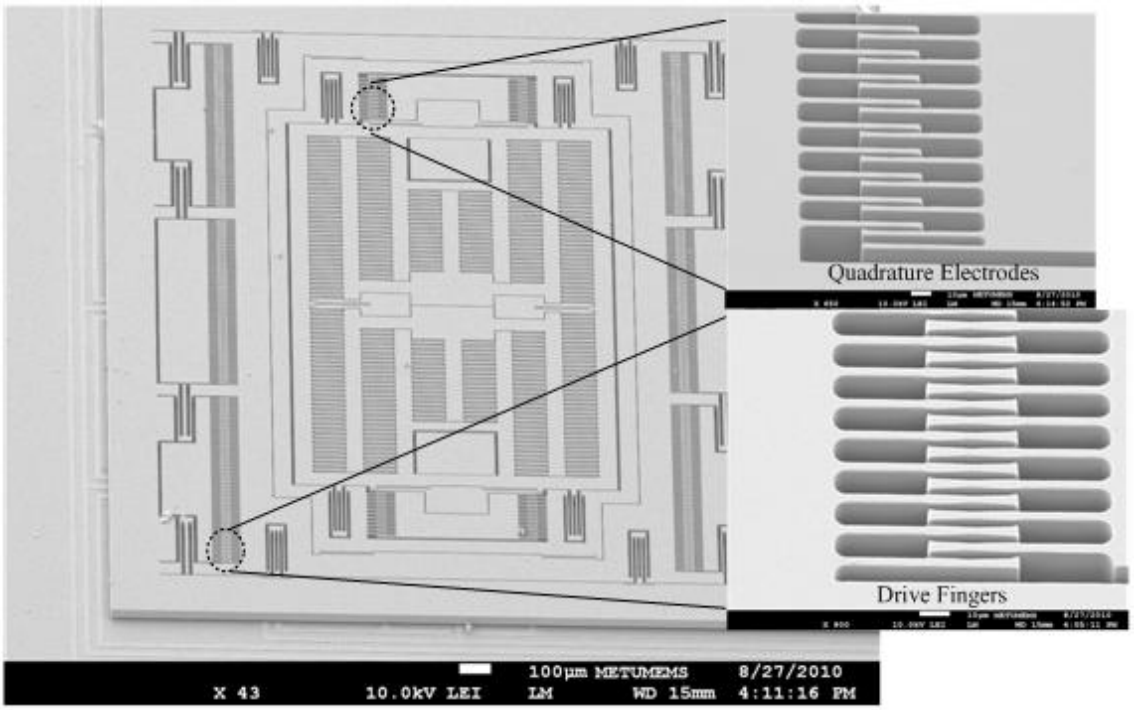

Figure 4.24 SEM image of an SOI gyroscope

In Figure 4.24 SEM image of an SOI gyroscope and zoomed views of quadrature electrodes and drive fingers are shown. The destruction on fingers is due to SOI notch but they are only on the surface. Overall destruction level is lower compared to SOG gyroscopes. These are the improvements due to DRIE etching (thickness is reduced to 35µm and not performed on glass). Stable DRIE etching increases the gyroscope performance since the unwanted quadrature signal is reduced. Mechanical structure is more close to ideal in SOI gyros.

Up to now the comparison of SOG based SOI and SOG processes is based on visual inspection and measurements; however the real comparison should be based on probe tests. During probe tests the resonance characteristics of drive and sense modes are obtained. To make a quantitave comparison between two processes drive modes of the gyroscopes on SOG and SOG based SOI wafers are compared, and Table 4.1 shows the data.

Table 4.1: Drive mode comparison of SOI and SOG wafers

Process	Tested	Working	Yield	Avr. Freq. (kHz)	Std dev.	Avr. Gain (dB)	Std Dev.
SOG	54	31	57.4%	13.02	0.71	-31.97	2.7
SOG based SOI	48	36	75%	13.82	0.41	-38.77	2.8

At first glance, it is seen that the yield of SOG based SOI process is almost 30% higher than that of SOG process. Design values of both the SOI and SOG drive frequencies are 15.5kHz. However due to process imperfections and local heating, measured frequencies are lower than the design values. SOI gyroscopes seem better in terms of resonance frequency; they are more close to their design values. Standard deviation of drive resonance frequencies is a measure of process uniformity in all around the wafer. Lower standard deviation in drive resonance frequency in SOI implies a more uniform DRIE process. Since the DRIE is limited with 35µm, etch time is shorter and DRIE is performed on SOI wafer instead of etched glass wafer, a more uniform DRIE etch is expected for SOI wafer. The average gain of SOI gyroscopes is lower, however the gain depends on the square of applied proof mass potential and 30-40V potential is applied to SOG gyroscopes whereas only 10-15V is applied to SOI gyroscopes. Under these conditions that much of gain difference is normal. Standard deviation in gain of SOI and SOG gyroscopes is almost the same.

To conclude, due to uniform DRIE etch, higher yield and operating at more feasible proof mass potentials (10-15V rather than 30-40V) SOG process is replaced with SOG based SOI process.

With an SOI wafer, SOG process can also be done. In this process shield metal is coated on device layer of SOI and bonded to glass as in SOG process. Later the handle and oxide layer of SOI is removed. At last step DRIE is performed. The advantage of this process compared to previous SOG process is handling of SOI wafer is easier compared to the 100µm silicon wafer used in previous SOG process. The thickness of SOI device layer can be chosen depending on the design.

4.4 Effect of BHF on Contact Resistance

Examining the contact resistance is one of the jobs studied. Effect of contact resistance on device performance depends on the readout method. Output of the gyroscope is converted into voltage through a transimpedance amplifier and this method is insensitive to contact resistance but ohmic contacts are always desired. Adding BHF before anodic bonding of glass and silicon was one of the process optimizations performed.

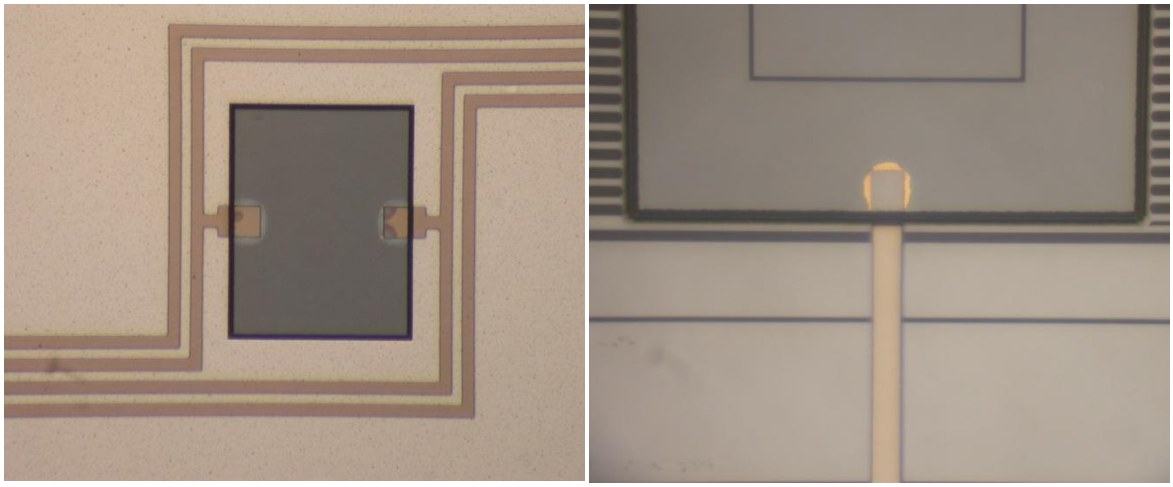

a b

Figure 4.25: Contact resistance (a) bad contact (b) good contact

Figure 4.25 shows a good and bad contact. In both SOG and SOG based SOI process interconnect metallization is on glass substrate and contacts between metal and silicon are occurs during anodic bonding on glass anchors. Normally during anodic bonding metal and silicon touch each other and a low (100-300Ω) contact resistance is expected. However contact resistances in the order of 100kΩ were measured. It is found that the view of contacts give idea about the contact resistance. In Figure 4.25 a the contacts started to change their color from yellow to brown. A complete yellow contact is measured to be a bad contact (resistance of 100kΩ measured). To be an actual ohmic contact the contact color should completely turn into brown and seems as if gold is squeezed like in Figure 4.25 b. The contact shown in Figure 4.25 b is an ohmic contact and the measured resistance is only due to the resistance of interconnect metallization (100-300Ω). It is found that the native oxide on silicon wafers prevents ohmic contacts to occur, adding BHF step to silicon before anodic bonding turns the contacts to be

ohmic as in Figure 4.25 b, when no BHF is applied contacts were as in Figure 4.25 a or even worse.

Anodic bonding temperature is another significant parameter determining the characteristics of the contact regions. The anodic bonding temperature should be lower than the eutectic point of silicon and gold. When silicon and gold touch each other and temperature is increased above 363^0C, an alloy occurs between them whose melting temperature is lower than both the gold and silicon [53]. The melting temperature of that alloy is 363 ^{0}C and that point is called as the eutectic point. When the anodic bonding temperature is higher than eutectic temperature of silicon and gold the eutectic alloy occurs and goes through the metal line. Figure 4.26 shows the eutectic formation through the metal lines. This situation may cause problem if additional cleaning is required. The eutectic metal lines are damaged and the contact is lost. Performing anodic bonding below the eutectic point is the optimum choice (350^0C, for example). Ohmic contacts are formed and metal lines survive during cleaning of the wafer.

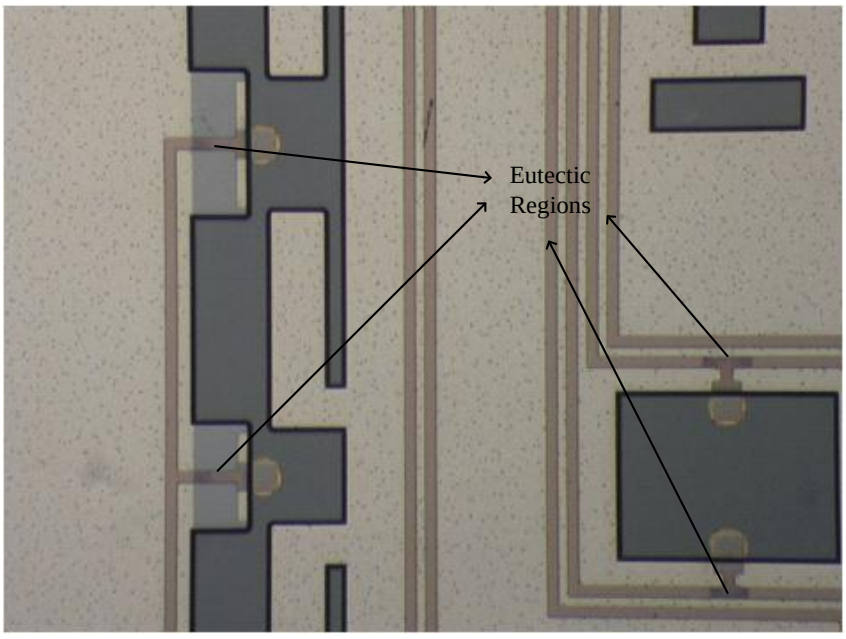

Figure 4.26: Eutectic formation on contacts

4.5 Summary

This chapter first describes the SOG based SOI process with detailed process flow. Anodic bonding of SOI and glass wafers is explained on two series capacitor model in which the charge should be preserved. Then SOG process with its problems is presented. The main problem of the process is performing DRIE on recessed glass wafer. The comparison between SOG based SOI and SOG processes is made and SOG based SOI process is found to be better in terms of yield, process uniformity, DRIE quality and handling. Improvements obtained with adding BHF step to silicon wafer before anodic bonding are presented with photographs.

CHAPTER 5

TEST RESULTS

This chapter presents the test results of the SOI and SOG gyroscopes. The improvements obtained with quadrature cancellation circuit and the effect of springs on quadrature error is provided. Section 5.1 presents the characterization and test procedure for gyroscopes and section 5.2 explains the test setup and test method for gyroscopes. Section 5.3 provides the data about the experimental verification of quadrature error. Section 5.4 gives the test results of the SOI gyroscopes with closed loop drive, sense and quadrature circuit. Effect of quadrature error on gyroscope performance is presented. In Section 5.5, scale factor and bias repeatability test results are provided. Section 5.6 shows the test results of the gyros with intentionally placed errors. Section 5.7 presents the test results of the SOG gyroscopes. Finally section 5.8 summarizes the performed tests and gives the conclusions.

5.1 Characterization and Test Procedure of Gyroscopes

Tests of the gyroscopes start after the fabrication process is completed. Gyroscopes from different places of the wafer are chosen and tested prior to dicing to see whether the wafer is worth dicing or not. If resonance characteristics of both drive and sense modes are observed as expected, the wafer is diced. After dicing each gyroscope die is tested separately at probe station. Figure 5.1 shows the atmosphere test setup used to test gyroscope dies. As seen in Figure 5.1 each die is placed in probe station where electrical contacts to the sensor are taken through the probes. Then the sensor is driven from dynamic signal analyzer which sweeps the frequency in the desired frequency band

and measures the transfer function of the system. The output current of the gyroscope is converted into voltage by a preamplifier and fed to dynamic signal analyzer. This test is a functionality test, i.e. the resonance characteristics of the sense and drive modes are extracted. For a gyroscope to pass the test both drive and sense modes of the gyroscope should show resonance characteristics. Gyroscopes having problems (that do not show resonance characteristics) are eliminated at this test. The gain, resonance frequency and proof mass potentials are recorded on a table. Then gyroscopes having desired resonance frequencies and gains are chosen. Generally a mismatch of 500Hz-1kHz is for 10V proof mass potential is sufficient for a gyroscope to be chosen.

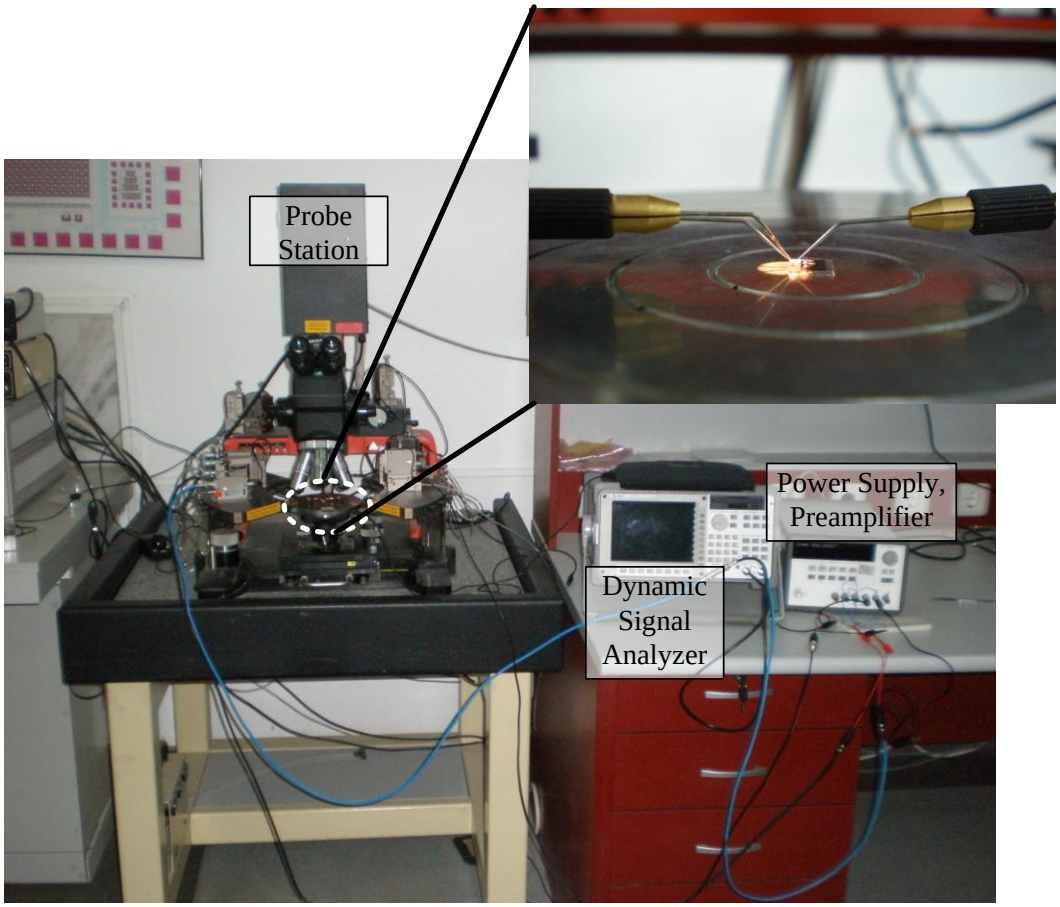

Figure 5.1: Test setup for die level gyroscope tests

After the probe tests gyroscope is mounted on hybrid preamplifier substrate, in other words gyroscope is combined with electronics. Figure 5.2 shows a gyroscope mounted to hybrid glass preamplifier substrate. The substrate is mounted in a special package

which can be vacuum sealed. So the circuit dimensions are adjusted to be mounted in the package shown in Figure 5.2. After connecting the gyroscope with preamplifier and instrumentation amplifier the module is again tested to check whether it is operating properly or not. Before vacuum sealing this test should be performed since, after packaging the connection between inside and outside is only package pins, there is no access to the inside of the package. Then the gyroscope is vacuum packaged with surrounding electronics using a technique called projection welding.

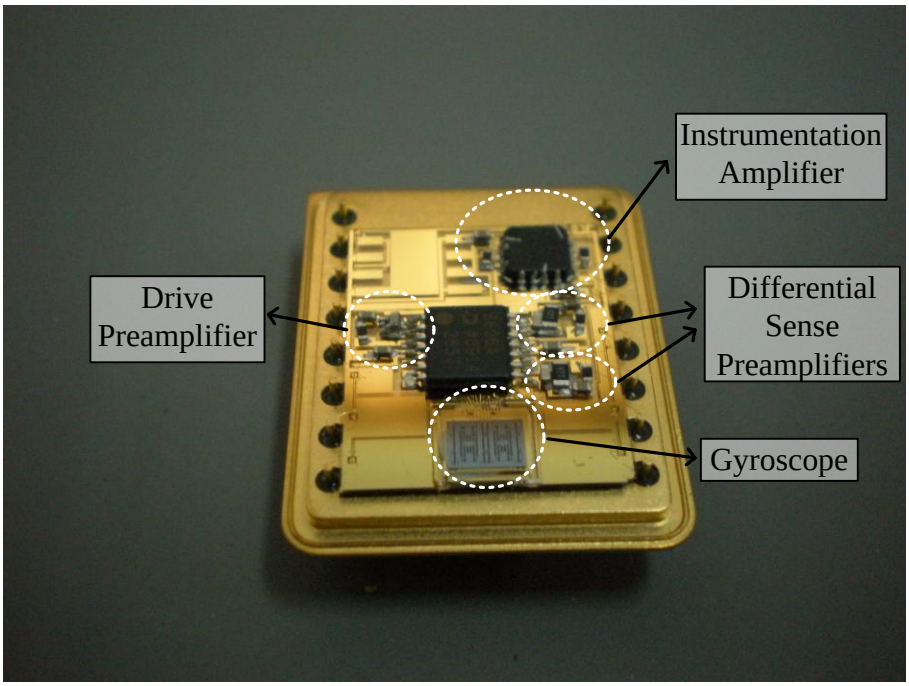

Figure 5.2: Gyroscope mounted on preamplifier substrate

When vacuum packaging step of the gyroscopes are completed, resonance tests are repeated to extract the parameters of the gyroscopes (capacitive sensitivities of drive and sense modes, quality factors and resonance frequencies). The capacitive sensitivities can be extracted either from atmosphere tests or vacuum tests, but quality factors and resonance frequencies can only be extracted from vacuum tests since they change with vacuum. The method followed to extract the parameters is described in Section 3.2.

Figure 5.3 shows the resonance characteristics of drive and sense modes at atmospheric pressure and vacuum. In vacuum the quality factors and gains of the both drive and sense modes increase. For drive mode, phase and gain characteristics are consistent at

atmosphere and vacuum. They show second order characteristics as they are modeled. The quality factor of the drive mode is typically 100-200 at atmosphere and increases to 45000-50000 at vacuum, gain similarly increases to 15dB-20dB from -30dB. Quality factor, resonance gain and resonance frequency are obtained from Figure 5.3 b, and second order transfer function of the gyroscope is extracted.

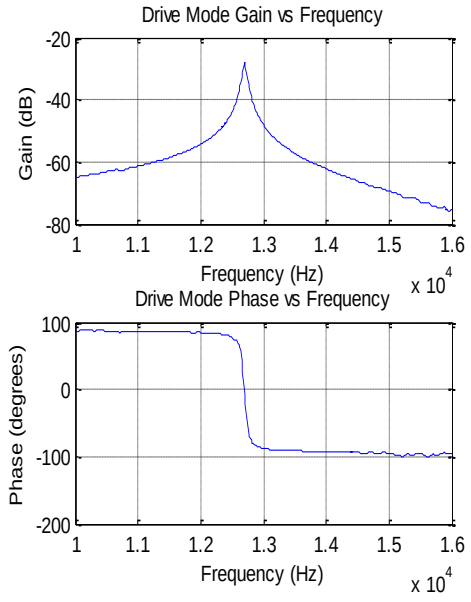

a. Drive mode at atmosphere

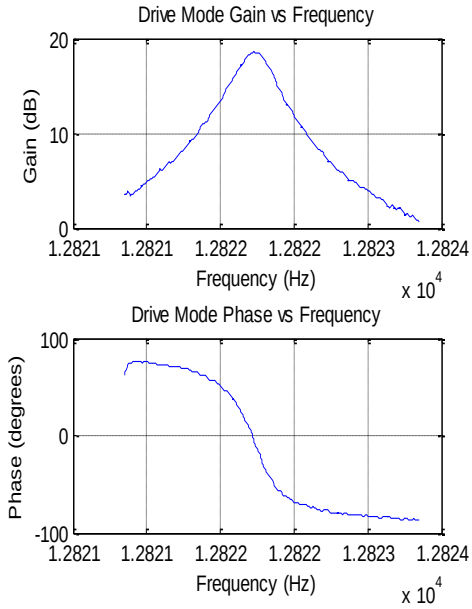

b. Drive mode at vacuum

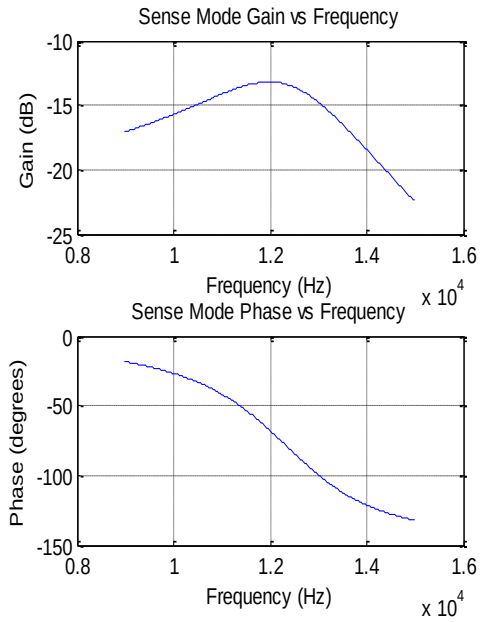

c. Sense mode at atmosphere

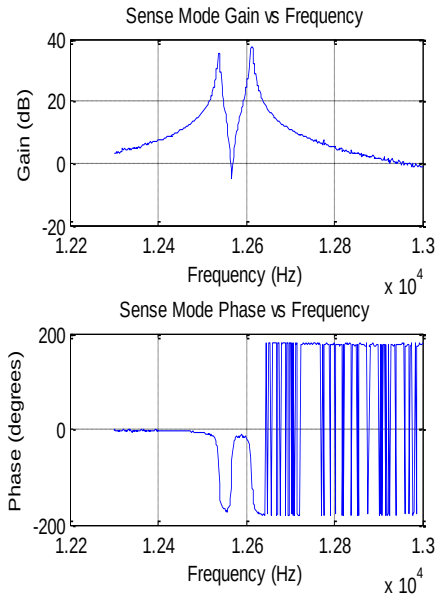

d. Sense mode at vacuum

Figure 5.3: Measured gyroscope resonance characteristics at atmosphere and vacuum

For the sense mode on the other hand, vacuum characteristics is different from drive mode. As seen Figure 5.3 d, two resonance peaks are observed. This is due to the design of the gyroscope and process imperfections. Gyroscope is designed for g-insensitivity. There are two gyroscopes and drive modes have mechanical connection between them forcing them to have a single peak; however sense modes do not have mechanical connection. Although they are perfectly symmetric in the layout, due to process imperfections a slight mismatch is observed between them. The nonideality in the sense mode cannot be observed at atmospheric pressure due to overdamped resonance characteristics. Two sense peaks are observed as a single wide peak at atmosphere. At vacuum they are clearly visible. The phase characteristics also exhibit as if there are two separate sense resonators and sense mode is modeled as if there are two separate resonators. The sense mode has quality factor of 5-10 and gain of (-10dB)–(-15dB) at atmosphere and quality factor of 2500-3000 and gain of 35-40dB at vacuum. Sense mode parameter extraction is done as in drive mode and detailed procedure is given in Section 3.2. The resonance gain, quality factor and resonance frequency are obtained from Figure 5.3 d.

The resonance characteristics of all the gyroscopes studied in this study will not be given like in Figure 5.3, instead the resonance gain, quality factor and resonance frequency will be given only. It is believed that it will be easier for the reader to follow in this way.

Table 5.1 and Table 5.2 show drive and sense resonance characteristics of the tested gyroscopes for specified proof mass potentials, respectively. There are empty spaces in Table 5.2 denoting that peak is not observed. Δf in Table 5.2 stands for the frequency mismatch of the drive and sense modes. Δf is taken as the minimum resonance frequency difference between drive and sense modes. For sense mode two separate resonance information is given to model the sense mode as two resonators.

Table 5.1: Measured drive resonance characteristics of the tested gyroscopes

Gyroscope	Proof Mass (V)	Res. Freq. (kHz)	Res. Gain (dB)	Quality Factor
SNW#6_G14	12	13.486	16.55	39667
SNW#6_F09	14	12.876	11.88	18162
SNW#7_N08	10	13.9	15.88	50546
SNWQ#1_N08	13	12.822	18.55	43465
SNWQ#1_L01	13	12.812	18.45	44957
SNWQ#1_J13	13	12.729	19.67	48586
SNWQ#1_F08	13	12.672	19.83	47820
SNWQ#1_O07	13	12.790	20.88	50654
SNWQ#1_K09	13	12.394	19.176	47670
SNWQ#1_I08	13	12.659	18.64	45213

Table 5.2: Measured sense resonance characteristics of the tested gyroscopes

		1st Peak			**2nd Peak**			
Gyro	V_{PM} (V)	Res.Fr. (kHz)	Gain (dB)	Q	Res.Fr. (kHz)	Gain (dB)	Q	Δf (Hz)
SNW#6_G14	12	13.325	37.65	1838	13.313	31.40	1763	161
SNW#6_F09	14	12.318	32	1027	12.229	30.8	1087	558
SNW#7_N08	10	13.698	34.92	3044	13.634	34.88	3029	202
SNWQ#1_N08	13	12.612	38.48	2314	12.5379	35.92	2411	210
SNWQ#1_L01	13	12.586	36.94	2420	15.926	21.26	845	226
SNWQ#1_J13	13	12.590	37.77	2518	12.285	37.56	2507	139
SNWQ#1_F08	13	12.473	39.47	1696	12.464	31	1696	199
SNWQ#1_O07	13	12.536	37.78	786	-	-	-	204
SNWQ#1_K09	13	12.14	38.17	2944	-	-	-	154
SNWQ#1_I08	13	12.548	33.02	1915	12.349	35.82	2235	111

5.2 Test Setup and Method for Gyroscopes

After vacuum packaging and characterization of gyroscopes, the next step is the performance tests. The vacuum packaged sensor module is connected with drive, sense and quadrature cancellation module on a PCB. These modules are placed in metal packages to reduce the noise. Figure 5.4 shows the photograph of the test setup for gyroscope performance tests.

During the tests first step is the scale factor and linearity tests. Gyroscope with its surrounding electronics is placed inside the computer controlled rate table. The applied rate is varied between $\pm 100^0$/sec with 10^0/sec steps and the output of the gyroscope is recorded by the data acquisition computer. Rate is started from 0^0/sec increased to 100^0/sec, decreased to -100^0/sec and finally increased to 0^0/sec with 10^0/sec steps. A triangular rate is applied to gyroscope, with this way the linearity and hysteresis is checked and scale factor is calculated. Then the gyroscope is fixed and the output of the gyroscope is recorded by the data acquisition computer. The recorded data is then processed by "AlaVar 5.2" Allan variance processing software.

The outputs of the inertial sensors are integrated during their usage. For example the output of the gyro is the angular velocity but to find the location (position) one have to integrate the velocity. And this is continuously done. Small errors are added up due to integration and at last these errors may diverge. Besides these the sensors scale factor may change, bias variations may occur etc. For the stated reasons modeling and estimating the sensor's error is critical. Allan Variance shows us the dominant errors with respect to averaging time. In this study Allan Variance method is used to measure the performance of the gyroscope.

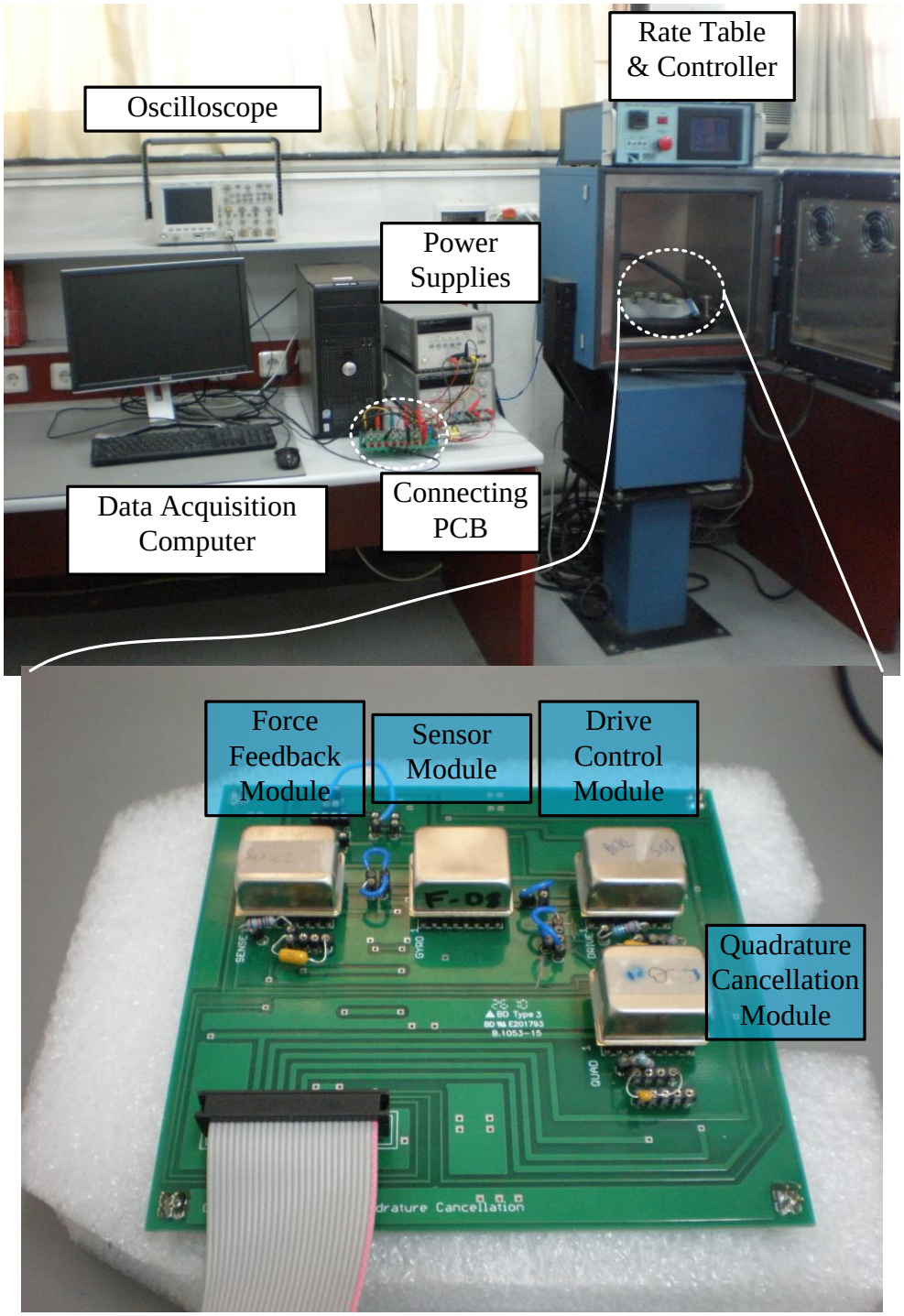

Figure 5.4: Photograph of the test setup for gyroscope performance tests

Figure 5.5 shows a typical Allan Variance plot. The most significant performance parameters are angle random walk which gives the thermal noise density or resolution and bias instability which gives the minimum detectable rate with the gyroscope. These

values are found by fitting the line with corresponding slope. The slopes corresponding to different noise sources are shown in Figure 5.5.

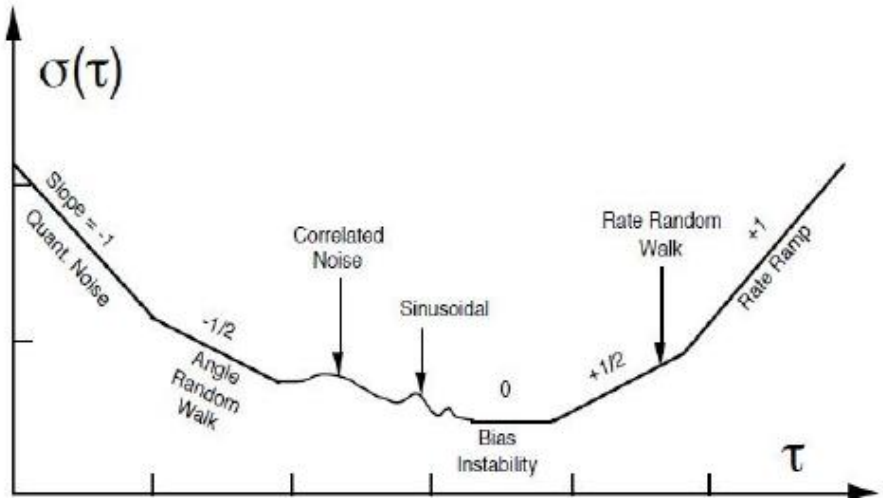

Figure 5.5: A typical Allan Variance graph

5.3 Experimental Verification of Quadrature Error

Modeling of quadrature error was examined in Section 2.7.2, and it was found that

$$n\frac{4V_{PM}\Delta V\varepsilon Xh}{y_0^2} = Yk_{effective} \tag{5.1}$$

All of the variables in Equation 5.1, except quadrature displacement Y are known or measurable. To find quadrature displacement, the preamplifier stage of the sense channel should be known. Under zero rate conditions on open loop, the signal observed at the output of the instrumentation amplifier $V_{SP}$is purely due to quadrature. By knowing the amplitude of quadrature signal, quadrature displacement Y can be found. Assuming capacitive preamplifier,

$$I_{SP} = V_{PM}\frac{\partial C_{SP}}{\partial y}jw_D Y \tag{5.2}$$

$$V_{SP} = \frac{1}{jw_D C}I_{SP}A_{Inst.Amp.} = V_{PM}\frac{\partial C_{SP}}{\partial y}Y\frac{1}{C}A_{Inst.Amp.} \tag{5.3}$$

$V_{SP}$is measured through tests and $\frac{\partial C_{SP}}{\partial y}$ is obtained through resonance tests. The other parameters in Equation 5.3 are known from design and quadrature displacement Y can be calculated. On open loop rate sensing, quadrature cancellation circuit is operated and the applied quadrature potential ΔV is measured. In Equation 5.1, all the parameters on the left and right hand side are known, they can be calculated and checked whether the equality is valid or not. Table 5.3 provides the parameters of SOI gyro N08 to check the equality in Equation 5.1.

Table 5.3: Parameters of the SOI gyroscope N08

Parameter	Value
Drive Resonance Frequency w_D	13.9kHZ
Sense Resonance Frequency w_S	13.634kHz
Quality Factor of the Sense Mode Q_S	3029
Mass of the Sense Mode m_S	8.34E^{-8}kg
Spring Constant of the Sense Mode k_S	612 N/m
Effective Spring Constant $k_{effective}$	636-624=24 N/m
Measured Quadrature Signal V_{SP}	$0.73V_{peak}$
Sensitivity $\partial C_{sp}/\partial y$	1.63E^{-6}F/m
Proof Mass Potential V_{PM}	10V
Measured Quadrature Potential ΔV	1.77V
Preamplifier Capacitance C	3.9pF
Calculated Quadrature Displacement Y	0.87E^{-8}m
Number of Quadrature Electrodes n	11
Drive Displacement X	4.2μm
Gap of Quadrature Fingers y_0	2.3μm
Permittivity of Free Space ε	8.85E^{-12}F/m
Calculated $k_{effective}Y$	2.1E^{-7}N
Calculated Applied Quadrature Force F_Q	1.92E^{-7}N

As seen in Table 5.3 the last two rows are close to each other, there is only 10% mismatch. These results show that analytical result found in Equation 2.54 is correct and this is consistent with the SIMULINK result which is in the order of $2.1*10^{-7}$N given in Figure 3.22. So; simulated, calculated and measured results agree with each other for quadrature cancellation.

5.4 Test Results of the SOI Gyroscopes with and without Quadrature Cancellation

The first step in the gyroscope test is monitoring the drive pick signal. Drive displacement should be kept constant throughout the life of the gyroscope and drive pick signal is the only way to check the amplitude of drive displacement. As mentioned in Section 3.3.1 pole zero cancellation can make the system very fast. Drive displacement settles very fast without overshoot. Figure 5.6 provides test result showing the effect of pole zero cancellation. As seen in Figure 5.6 settle time of the drive pick signal is measured to be 96msec and no overshoot is observed. It was theoretically calculated as 20msec, the difference is due to the current limits on power supplies and the settling of overall circuit.

Drive pick signal is set to $750mV_{peak}$ or $1.5V_{peak}$ in this study. For the specified proof mass potentials these set potentials corresponds to 3.5μm and 7μm drive displacements respectively. Test set up is adjusted so that with an additional resistor drive displacement can be set to 7μm, this is achieved by adding a parallel resistor to the gain resistor of the low pass filter in the drive control module.

Figure 5.7 shows drive pick and drive motor signals, for resistive preamplifier they are expected to be in phase. As seen in Figure 5.7 two signals are in phase with each other.

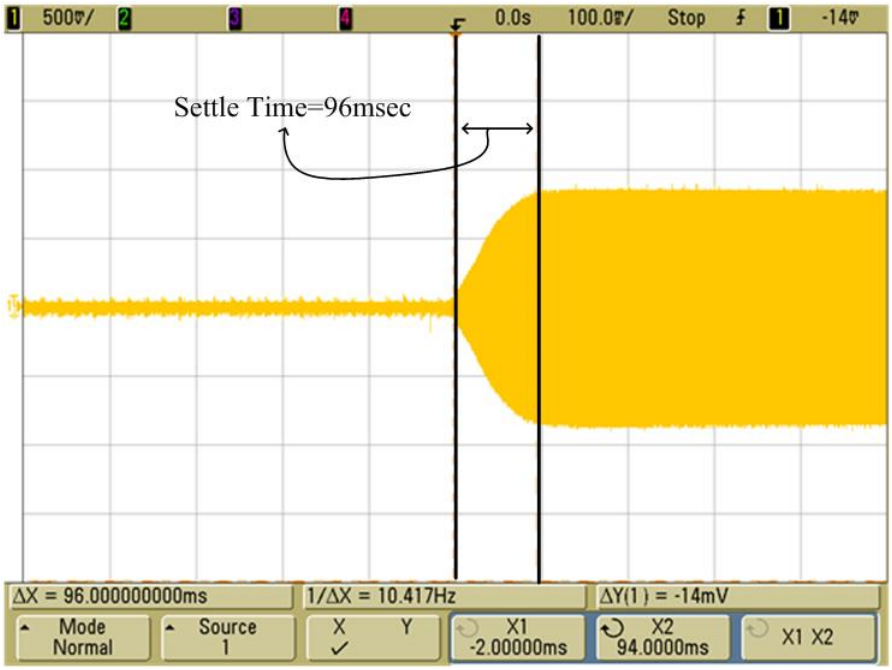

Figure 5.6: Drive pick signal showing the settle time

Figure 5.7: Drive pick signal and square wave drive motor signal

The main purpose of this study is to observe the effect of quadrature cancellation on gyroscope performance. In that sense identification of quadrature signal is important, to

better illustrate the quadrature error, Figure 5.8 shows quadrature signal with drive pick signal before and after quadrature cancellation.

a b

Figure 5.8: Drive pick and zero rate sense pick (Quadrature) signals (a) Before quadrature cancellation (b) After quadrature cancellation

As seen in Figure 5.8 a, under zero rate conditions there exists a signal at the sense pick output of the gyroscope. With resistive drive, capacitive sense and at mismatch conditions rate signal is in phase with drive signal, however there is 90^0 phase difference between the signals shown in Figure 5.8 a. The sense pick signal is purely due to quadrature error. In Figure 5.8 b, the quadrature signal is cancelled by the control electronics.

Normally the operation of force feedback circuit is based on phase sensitive demodulation; since the quadrature and rate signals have 90^0 phase difference quadrature is eliminated up to a certain level at phase sensitive demodulation. But quadrature signal is only eliminated electronically; force feedback electrodes do not apply any potential to stop the unwanted quadrature motion. The sense mode of the gyroscope always moves in an uncontrolled way if quadrature cancellation is not applied. If the quadrature signal's stability (amplitude and phase) over the time is guaranteed then the quadrature signal will only result in an offset at the output due to phase error introduced during phase sensitive demodulation. But the mechanisms that originate the quadrature error are not well defined and during the tests it was found that the quadrature signal is not stable throughout the time. And this signal is very high

compared to Coriolis signal as shown in Section 3.3.2.1, cancellation of this error will eliminate one of the major error sources for gyroscope.

Ideally the quadrature cancellation circuit should only cancel the quadrature motion and should not deteriorate the Coriolis signal. Scale factor test is used to verify that quadrature circuit does not degrade the Coriolis signal. The scale factor at different proof mass potentials and different drive displacements with and without quadrature circuit is measured for SNW#6_F09 and Table 5.4 shows the results.

Table 5.4: Scale factor measurements with and without quadrature circuit

Gyro	Vpm (V)	Drive disp. (μm)	Scale fact. w/quad. (mV/ ^{0}/sec)	Scale factor w/o quad. (mV /^{0}/sec)
SNW#6_F09	14	7	16	15.88
SNW#6_F09	13	7.5	18.66	18.46
SNW#6_F09	14	3.5	7.54	7.5
SNW#6_F09	13	3.75	8.74	8.7

As seen in Table 5.4 there is a slight increase in scale factor with quadrature cancellation. This is due to the fact that with quadrature cancellation unwanted quadrature signal is removed and phase sensitive demodulation becomes more effective. Another point is the effect of drive displacement on the scale factor, direct relation between drive displacement and scale factor can also be observed in Table 5.4. Increasing drive displacement directly increases the scale factor in the same order as expected.

The Allan Variance test results will be reported for the gyroscopes however each Allan Variance graph will not be given instead the procedure will be explained on a sample plot and for the other gyroscopes only the results will be reported. Allan Variance plots will be given wherever a significant performance is obtained. Figure 5.9 shows a sample Allan Variance plot for gyroscope SNW#6_G14 for 12V proof mass potential. Angle random walk (ARW) value is found by fitting a line with slope -1/2 and the angle random walk value is the point where the fitted line intersects 1 second. Bias instability

is found by fitting a line with 0 slope. The y intersect value is the value of bias instability. **In this study bias instability value is not divided by 0.664, depending on specifications [54].** Using Figure 5.9, ARW of SNW#6_G14 is 0.038 $^0/\sqrt{Hz}$ and bias instability is 1.1 ^{0}/hr. Read angle random walk value is divided by 60 to convert the unit $^0/\sqrt{hr}$ from ^{0}/hr/√Hz. In the literature generally the preferred unit of angle random walk is $^0/\sqrt{hr}$. The Allan Variance plot starts to decrease for sampling times (τ) smaller than 0.01sec (100Hz) which is not observed in standard Allan Variance plot given in Figure 5.5. Sampling frequency of 5kHz is used during data acquisition and a 100Hz LPF filter exists in the system. Since the sampling frequency is higher than cutoff frequency of LPF, the effect of LPF is seen. LPF filters the noise also for frequencies higher than 100Hz, so that portion of the graph should not be taken into account.

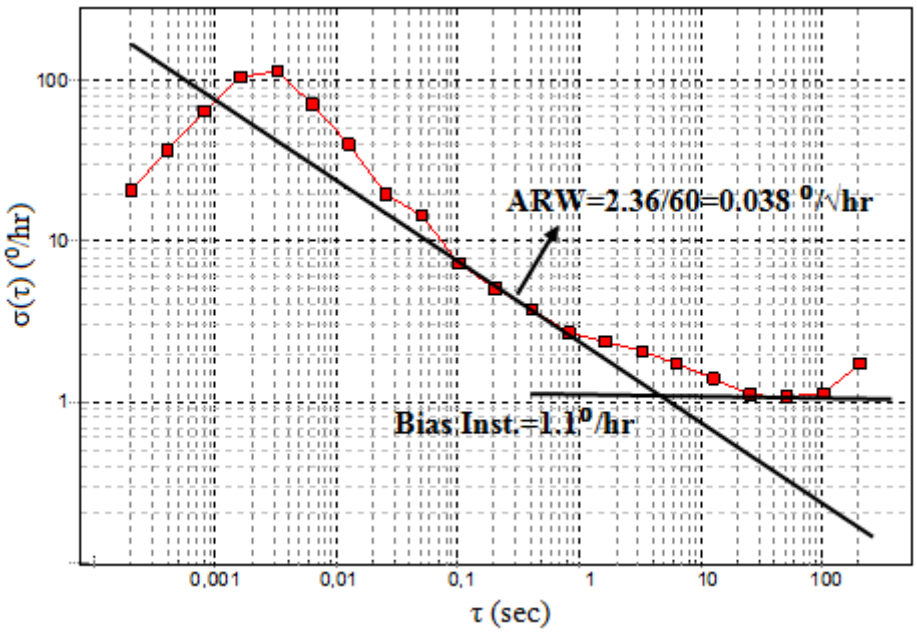

Figure 5.9: Allan Variance plot for SNW#6_G14

Table 5.5 shows gyroscope performance with and without quadrature compensation. When gyroscope SNW#6_F09 is examined direct result of quadrature cancellation cannot be extracted. This is due to the fact that that gyro has almost zero quadrature signal without compensation. There may be little quadrature signal which cannot be noticed and the small performance increase can also be seen. Since the quadrature signal is low the output offset of the sensor is low and quadrature cancellation injects a

little offset to the circuit due to nonidealities in the circuit and gyroscope. But note that gyros with zero quadrature signal without compensation are found rarely, and quadrature cancellation always improves the performance in a small or considerable amount. The empty regions for SNW#6_F09 indicate that tests are not performed.

Table 5.5: Gyroscope performance comparison with and without quadrature cancellation(1)

Gyroscope	V_{PM} (V)	Drive Disp. (μm)	W Quad. Cancellation			W/o Quad. Cancellation		
			Offset (mV)	Bias (^{0}/hr)	ARW ($^0/\sqrt{hr}$)	Offset (mV)	Bias (^{0}/hr)	ARW ($^0/\sqrt{hr}$)
SNW#6_F09	13	3.5	18	2	0.108	5	2.6	0.11
SNW#6_F09	14	3.5	7	1.4	0.063	4.5	1.6	0.058
SNW#6_F09	14	7	10	2.7	0.03	-	-	-
SNW#6_F09	8	5.6	22	2.92	0.062	-	-	-
SNW#6_G14	12	3.5	-1.9	1.1	0.034	-60	>100	0.348
SNW#7_N08	10	4	3	1.49	0.041	high	high	high

Effect of quadrature cancellation can be seen directly when gyroscopes SNW#6_G14 and SNW#7_N08 are examined. The performance is increased 10 times for ARW, 30 times for offset, and above 100 times for bias instability for 12V proof mass potential and 3.5μm drive displacement for SNW#6_G14. The regions written "high" implies that the output of the gyroscope is so unstable that taking Allan Variance data will be meaningless. The quadrature signal is so high that, without quadrature compensation it is not possible to obtain Allan Variance plot for SNW#7_N08. But with quadrature compensation its performance is in the order of 1^0/hr-2^0/hr.

Table 5.6: Gyroscope performance comparison with and without quadrature cancellation(2)

Gyroscope	V_{PM} (V)	Drive Disp. (µm)	W Quad. Cancellation			W/o Quad. Cancellation		
			Offset (mV)	Bias (^{0}/hr)	ARW (^{0}/√hr)	Offset (mV)	Bias (^{0}/hr)	ARW (^{0}/√hr)
SNWQ#1_J13	13	3.5	0.25	0.91	0.034	-207	7.1	0.36
SNWQ#1_J13	13	7	1.5	0.86	0.015	2500	-	-
SNWQ#1_J13	10	4.5	2.5	1.2	0.043	-	-	-
SNWQ#1_L01	13	3.5	2.5	3.1	0.07	223	11.2	0.49
SNWQ#1_N08	13	3.5	2.5	2.3	0.035	-12.5	2.5	0.037
SNWQ#1_N08	13	7	6	1.7	0.018	-23	1.9	0.025
SNWQ#1_O07	13	3.5	2	1.7	0.04	X	X	X
SNWQ#1_O07	13	7	2	0.91	0.018	X	X	X
SNWQ#1_F08	13	3.5	7	5.9	0.07	high	high	high
SNWQ#1_F08	13	7	12.5	4.8	0.046	high	high	high
SNWQ#1_I08	13	3.5	-4	0.72	0.029	2500	-	-
SNWQ#1_I08	13	7	-8	0.39	0.014	2500	-	-
SNWQ#1_K09	13	3.5	13.5	2.3	0.072	37	4.2	0.081

Table 5.6 shows again performance results of another set of gyroscopes with and without quadrature nulling. A broad range of gyroscopes are tested. The proof mass potential is kept generally constant and drive displacement is varied. The regions marked with yellow show the highest performance gyroscopes

The tests are initiated with SNWQ#1_J13, as seen in the first row the performance is increased 7.8 times for bias instability, 10.5 times for ARW and the offset at the output is almost zeroed (-207mV previously). Then the test is repeated by increasing the drive displacement to 7µm and the performance is increased. Increasing drive displacement directly reduces the rate equivalent Brownian and electronics noise as explained in

Chapter 3. So expecting the ARW to improve by an order of drive displacement is normal, but bias instability is expected to worsen without quadrature compensation if there is considerable quadrature error (>50^0/sec). Since drive displacement is increased the drift of the sensor is expected to be higher. Quadrature cancellation suppresses this drift significantly. Bias instability improves but the order of improvement is lower than ARW. Another advantage of quadrature circuit is it enables to operate the sensor in its most sensitive condition. The open loop scale factor of the gyroscope directly depends on Δf (the frequency mismatch between drive and sense modes, Equation 2.21) as Δf decreases the scale factor increases hence the rate equivalent noise decreases. But as the drive and sense modes come closer quadrature signal also increases and after some level electronics is saturated by high quadrature signal, the output is stuck to ±2.5V supplies. Same is valid for increased drive displacement; increasing drive displacement increases the quadrature level and may saturate the electronics. This is the case for SNWQ#1_J13 for 7μm displacement. As seen in the table output is stuck to 2.5V. With the quadrature signal compensated the sensor can be operated at these most sensitive (provides highest performance) regions without any trade off. The limit for decreasing the Δf comes from bandwidth, decreasing the frequency mismatch below 100 Hz will reduce the operation bandwidth.

The effect of quadrature cancellation can also be seen in SNWQ#1_L01, bias instability is improved 3.6 times, ARW is improved 7 times and output offset is improved 89 times.

The performance increase is not much in SNWQ#1_N08, that gyro has similar characteristics with SNW#6_F09, it has almost zero quadrature signal without compensation. There is an improvement but not clear as observed in the other gyroscopes.

The SNWQ#1_O7 was destructed during the tests so the performance tests without quad couldn't performed.

During the tests it is verified that quadrature signal is the main obstacle for a sensor in its path to high performance. Some sensors cannot be operated without quadrature compensation this is the case for SNWQ#1_F08. Without quadrature nulling the

deviation at the output of the sensor is so high that, it is not possible to obtain Allan Variance plot.

The best performance in this study is obtained from SNWQ#1_I08 at 13V proof mass potential and 7µm drive displacement. The quadrature signal is very high resulting in unstable operation without quadrature cancellation. The obtained result is 0.39^0/hr bias instability and $0.014^0/\sqrt{hr}$ ARW, Figure 5.10 shows the Allan Variance plot. This sensor has a theoretical white noise limit of $0.012^0/\sqrt{hr}$. With a properly prepared test setup and quadrature compensation a sensor operating at theoretical ARW limit is obtained.

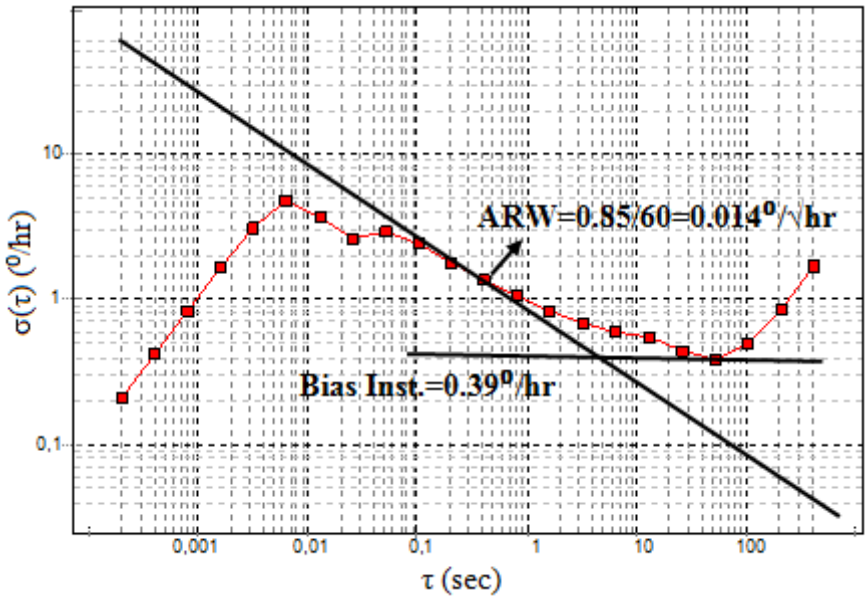

Figure 5.10: Allan Variance plot for SNWQ#1_I08 at 13V proof mass potential and 7µm drive displacement

The improvement with quadrature cancellation can also be seen in SNWQ#1_K09, bias instability and output offset is improved by a factor 2 and ARW improved by a factor of 1.1.

The best performance results in this study are obtained from SNWQ#1_J13 and SNWQ#1_I08, having frequency mismatch of 139Hz and 111Hz respectively. The other sensors have mismatch between 200-500Hz. Decreasing mismatch greatly

suppresses the electronics noise and enables to get highest performance results. The maximum cancelable limit of the quadrature circuit is limited with the controller OPAMP's supply potentials and frequency mismatch as explained in detail in Section 2.7.2. As frequency mismatch is decreased the maximum cancelable quadrature motion increases. The maximum cancelable limit with ±2.5V supplies depends on the sensor, but it is possible to cancel $\pm 800^0$/sec quadrature error with 139Hz mismatch and 13V proof mass potential for SNWQ#1_J13. Increasing the mismatch decreases the maximum cancelable quadrature error, and in that case it will be necessary to increase the supply potentials of the OPAMP.

Linearity and range are also significant performance parameters. Since the quadrature circuit solves the output offset problem, range problems due to offset are solved. Figure 5.11 shows the linearity plot for the gyroscope SNWQ#1_I08 for 13V proof mass potential and 7μm drive displacement. A triangular rate is applied to the gyroscope starting from 0^0/sec to 100^0/sec, 100^0/sec to -100^0/sec and -100^0/sec to 0^0/sec with 10^0/sec steps. And all of these data are plotted on Figure 5.11, as seen it is nearly perfect line, slope being equal to the scale factor. No hysteresis observed and R^2 linearity is nearly 1. R^2 linearity is obtained from "Microsoft Excel" program and actually does not show the actual linearity, the actual linearity is defined as the maximum deviation from the fitted line divided by the whole range. The actual linearity of this sensor is calculated as 99.98%. The gyroscope has a range of $\pm 100^0$/sec (tested) and it can be increased up to $\pm 150^0$/sec (±2.5V supply potentials).

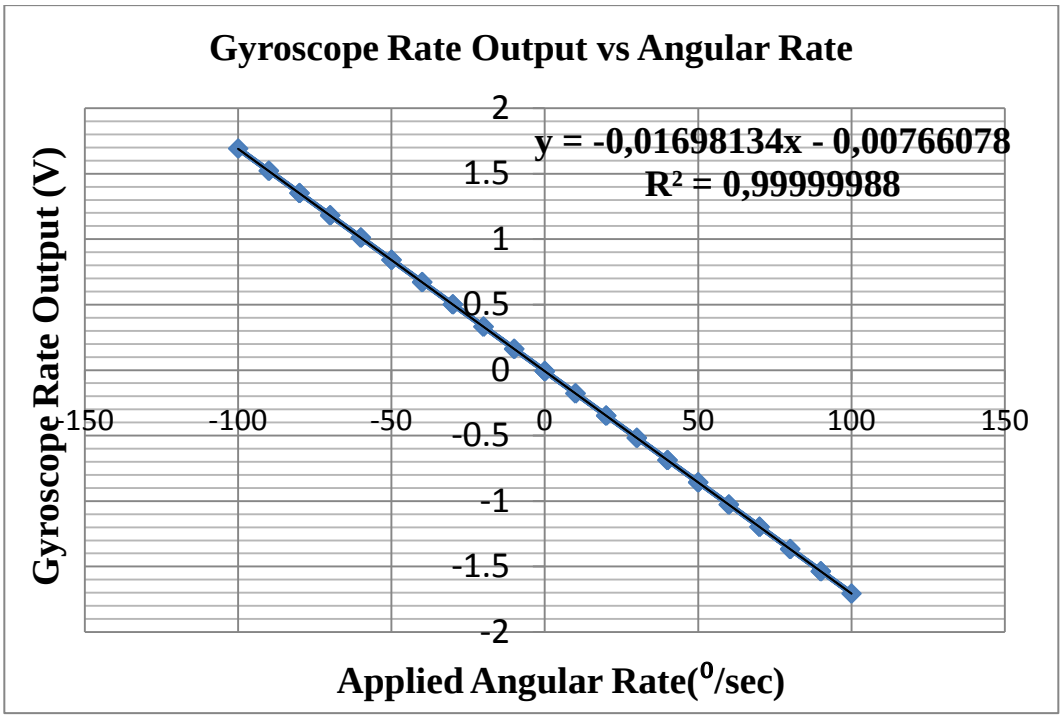

Figure 5.11: Gyroscope output vs angular rate plot for SNWQ#1_I08

To see the effect of quadrature cancellation on linearity, the linearity test is applied with and without quadrature cancellation to SNWQ#1_K09 for 13V proof mass potential and 3.5μm drive displacement. The actual linearity of the sensor with and without quadrature cancellation is 99.98% and 99.97% respectively, the results are close to each other. The linearity with quadrature cancellation is slightly higher and the improvement factor for linearity depends on quadrature level. Since the unwanted quadrature signal is canceled, an increase in the linearity is expected. Direct effect on gyroscopes could not be observed since force feedback increases the linearity also. Gyroscopes are already highly linear; quadrature cancellation cannot show a major improvement.

No bandwidth and settle time verification is performed for the sensors. Settle time can be measured by applying a step through rate table but settle time of the rate table is lower than the circuit's settle time which makes the measurement impossible. Bandwidth is simulated in SIMULINK design environment. The minimum bandwidth is 70Hz and typical bandwidth of the sensors varies between 80Hz to100Hz. Maximum allowed limit is the 100Hz, cut off frequency of the low pass filtered used in sense mode electronics. No bandwidth considerations exist for the quadrature compensation circuit

since its frequency does not vary with the applied rate frequency, the quadrature signal's frequency is always at drive mode frequency.

All the results in Table 5.5 and Table 5.6 verify that quadrature cancellation improves the performance of gyroscope. With current microfabrication tolerances quadrature error is inevitable, so compensating this error will increase the performance.

5.5 Scale factor and Bias Repeatability Tests

To measure the repeatability of scale factor, scale factor test is repeated for 5 times with and without quadrature cancellation circuit. Each scale factor test is done as follows. A triangular wave form is applied to gyroscope, starting from 0^0/sec the input rate is increased to 100^0/sec then decreased to -100^0/sec and finally increased to 0^0/sec with 10^o/sec steps and the output of the gyroscope is recorded. Then a line is fitted and scale factor is extracted.

Between each scale factor test the power supplies are turned off for 5 minutes and then power supplies are turned on and the test is repeated. Table 5.7 shows the scale factor repeatability test results with and without quadrature cancellation.

Table 5.7: Scale factor repeatability test results with and without quadrature cancellation for SNWQ#1_J13

Test	Scale factor without quadrature canc. (mV/^{0}/sec)	Scale factor with quadrature canc. (mV/^{0}/sec)
#1	7.29077	7.46343
#2	7.28814	7.46144
#3	7.28447	7.46189
#4	7.28946	7.4632
#5	7.28209	7.4631
Scale factor repeatability (ppm)	**495 (1σ)**	**119 (1σ)**

To find the scale factor repeatability, the mean of 5 scale factor values is found. Then standard deviation of the 5 number set is calculated and divided by the average scale factor. Finally the result is converted into unit of ppm. Results in Table 5.7 show that with quadrature cancellation applied the scale factor repeatability is improved to 119 ppm from 495 ppm. The slight increase in the scale factor is due to more effective phase sensitive demodulation with quadrature cancellation.

A similar procedure is followed for the bias repeatability tests. The output data of the gyroscope is collected for 30 minutes with any rate applied, and then the mean of the collected data is found. This is repeated for 5 times (between each test power supplies are turned off and waited 5 minutes) and the standard deviation of the 5 values is found and divided by the average scale factor (found using Table 5.7). The bias repeatability test result has the unit of ^{0}/hr. Table 5.8 shows the bias repeatability test results with and without quadrature cancellation.

Table 5.8: Bias repeatability test results with and without quadrature cancellation for SNWQ#1_J13

Test	**Mean of the data without quadrature canc. (mV)**	**Mean of the data with quadrature canc. (mV)**
#1	-197.064	1.94
#2	-197.076	1.957
#3	-197.065	1.965
#4	-197.098	1.972
#5	-197.094	1.976
Bias repeatability (^{0}/hr)	**7.87 (1σ)**	**6.88 (1σ)**

Temperature is significant in bias repeatability tests since the gyroscope parameters such (as resonance frequencies of drive and sense modes) depend on temperature and temperature sensor was not placed in sensor modules. Temperature is also significant in scale factor tests but the scale factor tests (1 hour) do not last as long as bias

repeatability tests (3-4 hours). Table 5.8 does not provide a significant improvement with quadrature cancellation on bias repeatability but gives an idea. With quadrature cancellation bias repeatability is slightly better. Temperature of the environment should be known to extract more solid comments. Note that with quadrature cancellation the offset at the output is greatly suppressed.

5.6 Test Results on the Sources of Quadrature Error

To get experimental data on the sources of quadrature error, gyros with intentionally placed errors are designed as explained in Section 2.8.2. In the simulations the most critical error source is found to be the force transmitting springs from drive to sense mode. Table 5.9 shows the quadrature levels of tested gyroscopes.

Table 5.9: Quadrature error levels of the tested gyroscopes

Width of S_Q	**Quadrature Error (°/sec)**	
	Simulated	**Measured**
3.6µm	438	450
3.8µm	228	391
4µm	0	65

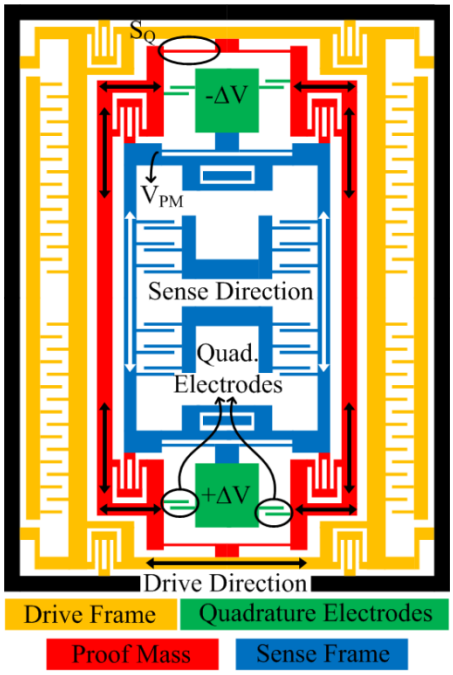

Figure 5.12: Simplified gyroscope figure

Figure 5.12 shows the simplified gyro figure again to visualize the introduced imperfection. S_Q is the spring that transmits drive displacement into proof mass frame and any imbalance at this spring causes quadrature motion. The relation between simulated and measured results can be seen in Table 5.9. They are consistent with each

other but not exactly. The difference between them is due to the already existing imperfections in the process, i.e. ideally drawn gyro has also quadrature error.

It can be concluded that the most significant source of quadrature error is springs. Since the force is transmitted through springs, any imbalance in springs causes quadrature error. Springs more specifically that transmit force between modes needs extreme care during design. Process variations should be taken into account and the layouts should be drawn taking into account the etching characteristics.

5.7 Test Results of the SOG Gyroscopes

Details of the gyroscopes fabricated with SOG process will not be examined in detail here. SOG gyroscopes do not have quadrature cancellation electrodes. Table 5.10 shows the best performance results obtained from SOG gyroscopes. The best ARW and Bias Instability is $0.045^0/\sqrt{hr}$ and $1.74^0/hr$ respectively (from different gyros), however the best results with SOI gyros are $0.014^0/\sqrt{hr}$ and $0.39^0/hr$ respectively (from the same gyro). This shows the importance of quadrature nulling and process improvement.

Table 5.10: Best performance results obtained with SOG gyroscopes

Gyroscope ID	V_{PM} (V)	Angle Random Walk ($^0/\sqrt{hr}$)	Bias Instability ($^0/hr$)
SNW#19_D06	32	0.07	1.74
SNW#19_D03	32	0.088	4.49
SNW#19_G09	30	0.048	4.3
SNW#19_K01	30	0.045	3.2

Table 5.11 shows the performance results of SNW#19_G09 for different proof mass potentials and drive displacements. Increasing drive displacement will decrease the rate equivalent noise and ARW improvement can be seen with increased drive displacement. However note that bias instability performance of the gyroscope worsens with increasing drive displacement. This is due to the fact that drift of the sensor increases with larger

drive displacement. Quadrature compensation solves this problem; in that case drift of the sensor is not changed as shown in SOI gyroscopes.

Table 5.11: Test results for SNW#19_G09 for different proof mass potentials and drive displacements

V_{PM} (V)	Drive Displacement					
	7.5 µm			5 µm		
	Scale Factor (mV/^{0}/sec)	ARW (^{0}/√hr)	Bias Inst. (^{0}/hr)	Scale Factor (mV/^{0}/sec)	ARW (^{0}/√hr)	Bias Inst. (^{0}/hr)
30	23.08	0.049	4.3	15.50	0.073	1.7
32	19.07	0.053	2	13.30	0.07	1.6

To compare SOG and SOI gyroscopes, SOI process with quadrature compensation applied has higher yield than SOG process. Since quadrature compensation increases the performance of the gyroscopes, for a given performance constraint SOI gyroscopes' yield and performance will be better than that of SOG gyroscopes.

5.8 Summary of the Tests and Conclusions

This chapter presents the performance results of SOI gyroscopes with and without quadrature cancellation, the experimental data about the sources of quadrature error and performance results of SOG gyroscopes without quadrature cancellation electrodes. The test results are obtained from a fully closed loop system. It is shown that closed loop drive amplitude control, force feedback and quadrature cancellation system operate as expected.

The effect of pole zero cancellation on drive amplitude control circuit is investigated. Drive pick signal is set to 750mV with no overshoot in 96msec, showing that pole zero cancellation improves the circuit performance.

It is shown that quadrature cancellation operates as expected, it only cancels out the unwanted quadrature motion, and the scale factor of the gyroscope slightly increases due

to more effective phase sensitive demodulation. Then the performance improvement with quadrature cancellation is examined. Table 5.12 shows the improvement factors of performance parameters with quadrature cancellation.

Table 5.12: Improvement factors of performance parameters with quadrature cancellation

Gyroscope	Improvement factor of Bias Instability	Improvement factor of ARW	Improvement factor of offset
SNWQ#1_J13	7.8	10.5	828
SNWQ#1_L01	3.6	7	89.2
SNWQ#1_N08	1.11	1.4	3.8
SNWQ#1_K09	1.8	1.1	2.7

Quadrature cancellation improves the bias instability up to 7.8 times, improves ARW up to 10 times, and improves output offset up to 800 times. These are significant improvements for gyroscope performance. All of the tested gyroscopes are not included in Table 5.12, only the ones that can be operated with and without quadrature cancellation are included. Actual improvement factor of quadrature cancellation is higher since some of the gyroscopes cannot be operated without quadrature nulling due to high quadrature levels. Quadrature cancellation enables the gyro to operate in its most sensitive region (when the mismatch between drive and sense modes is around 100Hz) where quadrature signal saturates the electronics. At its most sensitive region, electronics noise is highly suppressed resulting in a significant performance increase.

The effect of drive displacement on gyro performance with quadrature cancellation is also investigated. Drive displacement directly increases the gyroscope's rate sensitivity and decreases both rate equivalent mechanical Brownian noise and electronics noise. So a direct improvement in ARW is expected. Bias instability on the other hand expected to worsen since the drift will increase with increasing drive displacement. However with quadrature cancellation drift of the sensor is also suppressed and increasing drive displacement improves both bias instability and ARW without any trade off. Increasing

drive displacement also increases the quadrature signal and may saturate electronics. Quadrature cancellation prevents the electronics from saturation also. SNWQ#1_I08 is operated in its sensitive region with maximum drive displacement with the aid of quadrature cancellation. The gyro has an ARW of $0.014^0/\sqrt{hr}$ and bias instability of $0.39^0/hr$, with theoretical ARW limit of $0.012^0/\sqrt{hr}$. This is the highest performance gyroscope in METU up to now and achieved with quadrature cancellation. Without quadrature nulling it is not possible to operate gyro, the output is unstable due to high quadrature.

Sources of quadrature error are examined experimentally. Through simulations springs are found to be the major source of quadrature error and gyros with spring imperfections fabricated and tested. As expected gyros with spring imperfections have absolutely higher quadrature errors than standard gyros. The gyros have measured quadrature errors of 450^0/sec and 391°/sec for 3.6μm and 3.8μm spring (S_Q) widths respectively. The simulated quadrature levels are 438°/sec and 228°/sec, respectively. The highest quadrature error observed in standard gyros was 150^0/sec. Simulations and experimental results are consistent with each other verifying that springs especially force transmitting springs should be designed carefully.

The performances of gyroscopes fabricated with SOG process and SOG based SOI process are compared. SOG gyroscopes do not have quadrature cancellation electrodes and the highest performance obtained is ARW of $0.045^0/\sqrt{hr}$ and bias instability of $1.74^0/hr$. However these values for SOI gyros with quadrature cancellation are $0.014^0/\sqrt{hr}$ and $0.39^0/hr$ showing the importance of quadrature cancellation and process improvement.

The gyros have R^2 linearity of almost 1 and actual linearity of 99.98%, range of measured $\pm100^0$/sec but at least $\pm150^0$/sec is possible. The minimum bandwidth is 70Hz, typically varies with 80-100Hz. 100Hz limit comes from the cutoff of the LPF. The highest quadrature error that can be canceled is $\pm800^0$/sec limited with ±2.5V supply potentials which is more efficient than [16] and [17]. With higher supplies more possible.

Scale factor and bias repeatability tests are done for SNWQ#1_J13. Scale factor and bias tests are performed for 5 times and then the data are processed to find the repeatability values. Scale factor repeatability values without quadrature cancellation and with quadrature cancellation are 495ppm and 119ppm both for 1σ, respectively. The improvement of quadrature cancellation can directly be seen. Bias repeatability values without quadrature cancellation and with quadrature cancellation are 7.87^0/hr and 6.88^0/hr both for 1σ respectively. They are nearly the same the effect of quadrature cancellation cannot directly be seen. But temperature is significant in these tests and the sensor modules do not have temperature sensors. To extract more solid comments temperature of the environment should be known.

Table 5.13 shows the highest performance gyroscopes reported in the literature and this work. As seen there is not a MEMS gyroscope developed satisfying the inertial grade requirements yet but tactical grade requirements are satisfied. The gyroscope performance is improving and inertial grade requirements will be satisfied in the near future.

Table 5.13: Comparison of This Work with the Best Gyroscopes Reported in the Literature

Institution	ARW ($^0/\sqrt{hr}$)	Bias Ins. (^{0}/hr)	Bandwidth (Hz)	Range ($\pm^0$/sec)
Tactical Grade	0.5-0.05	0.1-10	100	>500
Inertial Grade	<0.001	<0.01	100	>400
Honeywell [4]	0.002	0.03	-*	-*
Gatech [16]	0.003	0.16	1-10	-*
Thales [17]	0.01	<0.1	-*	1000
LITEF GmbH [55]	0.3	0.12	<500	1000
This Work	0.014	0.39	70	>100

* not reported

To compare this work with the others in Table 5.13, [4], [16], and [17] have higher bias instability and ARW performance compared to this work. [16] and [17] operate the gyro

at matched mode which decreases their bandwidth. [4] doesn't provide any range or bandwidth information. Only this work and [55] clearly describes all of the performance parameters. The ARW and bias instability obtained in this work is comparable to the highest performance gyroscopes' in the literature and not far away from them and even better in some aspects.

Quadrature cancellation improved the ARW of the gyros to their theoretical limits, verifying that quadrature error is the major performance limiting error source of MEMS gyroscopes. For further performance increase, modifications in mechanical structure are needed.

CHAPTER 6

CONCLUSIONS AND FUTURE WORK

This work presents the effect of quadrature cancellation on the performance of a fully decoupled MEMS gyroscope structure and gives experimental data on the sources of quadrature error for the first time in the literature. In the first step quadrature cancellation electrodes operating with differential DC potentials are designed for the fully decoupled gyroscope structure developed at METU. The equations governing the vibratory gyroscope drive, sense modes and quadrature error are derived. FEM simulations are used to observe higher order effects and to understand the sources of quadrature error. Depending on simulation results gyros with intentionally placed imperfections are placed on the layout. Closed loop drive amplitude control, sense force feedback and quadrature cancellation circuits are designed and verified in SIMULINK design environment. The tested gyroscopes are fabricated with SOG based SOI process which is the improved version of the SOG process. The designed control circuits are implemented in low noise hybrid modules, connected on a printed circuit board (PCB), and tests are performed.

Based on the accomplishments and results of this research following conclusions can be drawn:

1. Design of quadrature cancellation electrodes for the fully decoupled gyroscope structure is investigated. The quadrature fingers are placed on proof mass frame in a special capacitive configuration such that by using drive displacement and applied $\pm\Delta V$ potentials they generate a force to stop the unwanted quadrature

motion. The relation between quadrature force and displacement shows that maximum amount of cancellable quadrature motion depends on the frequency mismatch between drive and sense modes. As the amount of mismatch decreases maximum amount of quadrature motion that can be canceled increases. FEM simulations are used to model the quadrature error and spring imbalances are found to be the major source of quadrature error. Springs that transmit force can lead to quadrature errors of 438^0/sec with only 10% mismatch.

2. Fully closed loop control system consisting of drive amplitude control, sense force feedback and quadrature cancellation is designed. The followed controller design procedure is the same for all. First the open loop transfer function is extracted with the simplified drive or sense model, second the controller parameters are optimized then the closed loop circuit is verified in SIMULINK design environment. The minimum detectable rate mainly depends on the noise performance of sense mode electronics. It is found that the preamplifier stage especially the current noise of the preamplifier OPAMP dominates the overall noise performance of the system. The noise coming from electronics and mechanical structure (Brownian noise) are in the same order. Increasing drive displacement has direct decreasing effect on both rate equivalent mechanical and electronics noise.

3. An improved version of the SOG process is developed. The problems of the SOG process are reviewed. The main problem is performing DRIE on anodically bonded recessed glass wafer which results in over heating of the wafer during process. To solve this problem SOG based SOI process is developed, different from SOG process DRIE is performed prior to anodic bonding. Device layer is formed on SOI wafer and then anodic bonding is done. The mechanism behind the anodic bonding of SOI and glass wafers is understood. When the bonding is performed as standard anodic bonding, two series capacitors are formed during bonding and most of the applied potential occurs on device layer of SOI and glass wafer which is desired. SOG based SOI

and SOG processes are compared and the former is found to be better in terms of DRIE quality, yield and uniformity. Previously the contact resistances up to 100kΩ were measured. The problem is solved by adding BHF step to silicon wafer before anodic bonding. The native oxide on the silicon wafer prevents ohmic contacts between metals and silicon. Another problem is the eutectic formation between metal lines and silicon during anodic bonding which is prevented by decreasing the anodic bonding temperature (350^0C) below eutectic temperature of silicon and gold (363^0C).

4. Fully closed loop system, i.e. sensor, drive amplitude control, sense force feedback and quadrature cancellation modules are connected on a PCB. Each module is formed with discrete, commercial components. The effect of pole zero cancellation on drive mode settle time and overshoot is verified. With pole zero cancellation settle time of 96msec without any overshoot is obtained. The theoretical value is 20 msec, the difference is due to supply current limits and the settle time of the overall circuit. Ideally the quadrature cancellation circuit should only cancel the quadrature signal; the Coriolis signal should be preserved. The scale factor tests on SNWQ#6_F09 are performed with and without quadrature circuit and for different drive displacements. Test results verify that quadrature cancellation circuit slightly increases the scale factor of the system due to more effective phase sensitive demodulation and scale factor directly depends on drive displacement. Allan Variance tests are performed with and without quadrature cancellation. Test results show that quadrature cancellation improves bias instability up to 7.8 times, ARW up to 10 times and output offset up to 800 times. The improvement factor is higher for gyros which cannot be operated without quadrature cancellation. For some gyros quadrature signal is so high that it saturates the electronics. With quadrature cancellation the gyros can be operated at its most sensitive region with maximum drive displacement to get the highest performance without saturating the electronics, normally without quadrature cancellation the electronics is saturated at the stated conditions. With quadrature cancellation drive displacement can be increased without any trade

off, normally increasing drive displacement increases the drift of the sensor and bias instability worsens if there exists considerable quadrature error (>50^0/sec). With quadrature cancellation the gyroscope performance reached to theoretical ARW limit. A gyro operating at theoretical ARW is obtained. The bias instability is 0.39^0/hr and ARW is $0.014^0/\sqrt{}$hr, the theoretical limit of ARW is $0.012^0/\sqrt{}$hr. These results verify that quadrature cancellation is the major performance limiting parameter and with cancellation gyroscope performance reached to its theoretical limits.

5. The R^2 linearity of gyroscopes are very close to 1 (99.9999988%). However the actual linearity is (99.98%) sufficient for tactical grade applications. The range of the gyroscopes is increased since the quadrature cancellation circuit eliminates the output offset. Most of the gyroscopes' output offset is lower than 10mV, $\pm100^0$/sec range measured but at least $\pm150^0$/sec range can be obtained. The minimum bandwidth of the sensors is 70Hz but typically varies between 80Hz-100Hz limited with the cutoff frequency of the low pass filter. Experimental investigation of quadrature error sources shows that gyros with spring imperfections have absolutely higher quadrature errors. The highest quadrature error observed in standard gyros is 150^o/sec. However, fabricated gyroscopes with spring imperfections have measured quadrature errors of 450^0/sec and 391^o/sec for 3.6μm and 3.8μm spring widths, respectively. The simulated quadrature levels are 438^o/sec and 228^o/sec, respectively. Simulated and measured values follow each other and the difference is due to the already imperfections in the fabrication process. Springs are the main sources of quadrature error, at the design stage special attention should be paid to spring design. The constructed quadrature cancellation circuit can cancel $\pm800^0$/sec quadrature error and limited with ±2.5V supply potentials. The performance of SOI and SOG gyroscopes compared, the best ARW is $0.045^0/\sqrt{}$hr and the best bias instability is 1.74^0/hr for SOG. However these are $0.014^0/\sqrt{}$hr and 0.39^0/hr for SOI gyroscopes, thanks to quadrature error cancellation and improved process.

6. Scale factor and bias repeatability tests are performed. With quadrature cancellation scale factor repeatability is found as 119ppm and without quadrature cancellation found as 495ppm, both for 1σ. The improvement with quadrature cancellation can directly be seen. However bias repeatability values without and with quadrature cancellation is found as 7.87^0/hr, 6.88^0/hr respectively both for 1σ. They are nearly the same. The temperature of the environment is critical during bias tests since the tests take 3-4 hours and the sensor module does not have temperature sensor. More exact results can be drawn with a constant temperature test setup and temperature sensor.

The main conclusion of this study can be summarized as, quadrature error is the major parameter limiting gyro performance and in the path to sub degree per hour gyroscopes this error should be cancelled.

This research shows that the gyroscopes developed at METU have come to their theoretical ARW performance limits with current analog control and mechanical structure. To further increase the performance and reliability some of the future research topics can be listed as follows:

1. Wafer level vacuum packaging of gyroscopes should be achieved as soon as possible. With wafer level vacuum packaging the quality factors of the drive and sense modes will significantly increase. The increase in the quality factor of the sense mode will increase gyroscope performance since rate equivalent Brownian noise of the mechanical sensor will decrease. Another advantage, handling of gyro chips will be easier and most of them will survive during integration of electronics and chip. Currently extreme care is required while handling the chips and some gyro chips are lost due to dust during integration.

2. A new mechanical structure with higher "A" ratio (A denotes the ratio of proof mass divided by total mass of the sense mode, determines the rate sensitivity of the gyroscope) can be designed. Currently this ratio is 0.385, increasing this

ratio will have a direct decreasing effect on rate equivalent noise. A mechanical structure with higher proof mass or a new decoupled gyroscope structure can be designed.

3. Converting the preamplifier outputs to digital and implementing the controller in digital domain can simplify and reduce the overall size of the system. With this way controller parameters can be updated instantaneously. An increase in the performance of the gyroscopes can also be obtained.

4. Mode matching can be studied to suppress the rate equivalent electronics noise. In that case, two peaks observed at the sense mode of the gyroscope should be examined carefully. Because the gyroscope can be matched only one of the peaks or another mechanical structure having a single sense peak can be designed.

In conclusion, in the content of this study quadrature cancellation is applied to fully decoupled gyroscope structure, the performance improvement with quadrature error cancellation is experimentally studied and experimental data on the sources of quadrature error is provided. All of these works are successfully studied and presented for the first time in the literature.

REFERENCES

[1] Gary K. Fedder, "MEMS Fabrication," *ITC International Test Conference*, paper 27.3, 2003.

[2] http://www.isuppli.com/MEMS-and-Sensors/News/Pages/MEMS-Market-to-Propel-toward-Double-Digit-Growth-in-2010.aspx.

[3] Jeremie Bouchaud, "Taking the pulse of MEMS industry," *WTC*, April 2007.

[4] Burgess R. Johnson, Eugen Cabuz, Howard B. French, Ryan Supino, "Development of a MEMS Gyroscope for Northfinding Applications," *Position Location and Navigation Symposium (PLANS)*, pp.168-170, 2010.

[5] IEEE Standard for Inertial Sensors Terminology, IEEE Std 528-2001, November 2001.

[6] Navid Yazdi, Farrokh Ayazi, and Khalil Najafi, "Micromachined Inertial Sensors," *Proceedings of the IEEE*, Vol.86, No.8, pp.1640-1659, August 1998.

[7] P. Greiff, B. Boxenhorn, T. King, and L. Niles, "Silicon Monolithic Micromechanical Gyroscope, *6th International Conference of Solid State Sensors and Actuators (Transducers'91)*, pp. 966-968, San Fransisco, USA, June 1991.

[8] J. Bernstein, S. Cho, A. T. King, A. Kourepenis, P. Maciel, and M. Weinberg, " A Micromachined Comb-Drive Tuning Fork Rate Gyroscope," Proceedings of IEEE Micro Mechanical Systems Workshop (MEMS'93), pp. 143-148, Fort Lauderdale, FL, February 1993.

[9] M. W. Putty, K. Najafi, "A Micromachined Vibrating Ring Gyroscope," *Solid State Sensor and Actuator Workshop*, pp.213-220, Hilton Head Island, SC, USA, June 1994.

[10] W. A. Clark, "Micromechined Vibratory Rate Gyroscopes," *Ph.D. Dissertation*, University of California, Berkeley, Fall 1997.

[11] John A. Geen, Steven J. Sherman, John F. Chang, and Stephen R. Lewis, "Single-Chip Surface Micromachined Integrated Gyroscope With 50^0/h Allan Deviation," *IEEE Journal of Solid-State Circuits*, Vol. 37, No. 12, pp. 1860-1866, December 2002.

[12] Huikai Xie, Gary K. Fedder, "Fabrication, Characterization, and Analysis of a DRIE CMOS-MEMS Gyroscope," IEEE Sensors Journal, Vol. 3, No.5, pp. 622-631, October 2003.

[13] Cenk Acar, and Andrei M. Shkel, "Inherently Robust Micromachined Gyroscopes With 2-DOF Sense-Mode Oscillator," *Journal of Microelectromechanical Systems*, Vol. 15, No. 12, April 2006.

[14] R. Neul, U.M. Gomez, K. Kehr, W. Bauer, J. Classen, C. Döring, E. Esch, S. Götz, J. Hauer, B. Kuhlman, C. Lang, M. Veith, and R. Wiling, "Micromachined Angular Rate Sensors for Automative Applications," *IEEE Sensors Journal*, Vol. 7, No.2, pp. 302-309, February 2007.

[15] M.F. Zaman, A. Sharma, Z. Hao, F. Ayazi, "A Mode-Matched Silicon-Yaw Tuning-Fork Gyroscope With Subdegree-Per-Hour Allan Deviation Bias Instability," Journal of Microelectromechanical Systems, Vol. 17, No. 6, pp.1526-1536, December 2008.

[16] Ajit Sharma, Mohammad Faisal Zaman, and Farrokh Ayazi, "A Sub 0.2^0/hr Bias Drift Micromechanical Gyroscope With Automatic CMOS Mode-Matching," *IEEE Journal of Solid State Circuits*, Vol. 44, No. 5, pp.1593-1608, May 2009.

[17] B. Chaumet, B. Leverrier, C. Rougeot, S. Bouyat, "A New Silicon Tuning Fork Gyroscope for Aerospace Applications," *Symposium Gyro Technology*, pp. 1.1-1.13, Karlsruhe, Germany, September 2009.

[18] H. Rödjegard, D. Sadström, P. Pelin, N. Hedenstierna, D. Eckerbert, and G.I. Andersson, "A Digitally Controlled MEMS Gyroscope with 3.2 deg/hr Stability," TRANSDUCERS'05, pp. 535-538, Seoul, Korea, June 2005.

[19] J. Raman, E. Cretu, P. Rombouts, and L. Weyten, "A Closed-Loop Digitally Controlled MEMS Gyroscope With Unconstrained Sigma-Delta Force-Feedback," *IEEE Sensors Journal*, Vol. 9, No. 3, 297-305, March 2009.

[20] S. E. Alper, "Silicon Surface Micromachined Gyroscopes Using MEMS Technology," *M.Sc. Thesis*, Middle East Technical University, September 2000.

[21] S. E. Alper, T. Akin, "A Symmetric Surface Micromachined Gyroscope," Sensors and Actuators, A 97-98, pp. 347-358, 2002.

[22] S. E. Alper, "MEMS Gyroscopes for Tactical-Grade Inertial Measurement Applications," *Ph.D. Dissertation*, Middle East Technical University, September 2005.

[23] S. E. Alper, T. Akin, "Symmetrical and decoupled nickel microgyroscope on insulating substrate," *Sensors and Actuators*, A 115, pp. 336- 350, 2004.

[24] S. E. Alper, T. Akin, "A Single-Crystal Silicon Symmetrical and Decoupled MEMS Gyroscope on an Insulating Substrate," Journal of Microelectromechanical Systems, Vol. 14, No. 4, pp. 707-717, August 2005.

[25] S. E. Alper, K. M. Silay, T. Akin, "A low-cost rate-grade nickel microgyroscope," *Sensors and Actuators*, A 132, pp. 171-181, 2006.

[26] S. E. Alper, K. Azgin, and T. Akin, "High-Performance SOI-MEMS Gyroscope With Decoupled Oscillation Modes," *MEMS 2006*, pp. 70-73, Istanbul, Turkey, January 2006.

[27] S. E. Alper, K. Azgin, T. Akin, "A high-performance silicon-on-insulator MEMS gyroscope operating at atmospheric pressure," *Sensors and Actuators*, A 135, pp.34-42, 2007.

[28] K. Azgin, Y. Temiz, and T. Akin, “An SOI-MEMS Tuning Fork Gyroscope With Linearly Coupled Drive Mechanism,” *MEMS 2007*, pp. 607-610, Kobe, Japan, January 2007.

[29] S. E. Alper, Y. Temiz, and T. Akin, “A Compact Angular Rate Sensor System Using a Fully Decoupled Silicon-on-Glass MEMS Gyroscope,” *Journal of Microelectromechanical Systems*, Vol. 17, No. 6, pp. 1418-1429, December 2008.

[30] K. Sahin, E. Sahin, S. E. Alper, and T. Akin, “A wide-bandwidth and high-sensitivity robust microgyroscope,” *Journal of Micromechanics and Microengineering*, 19 074004, 2009.

[31] Emre Şahin, “High Performance Readout and Control Electronics for MEMS Gyroscopes,” *M.S. Thesis*, Middle East Technical University, February 2009.

[32] John A. Geen, “Micromachined Gyros,” *US Patent*, 6122961, September 26, 2000.

[33] John A. Geen, “Micromachined Sensors With Quadrature Suppression,” *US Patent*, 7032451, April 25, 2006.

[34] Joseph Seeger, Ali Joseph Rastegar, Milton T. Tormey, “Method and Apparatus for Electronic Cancellation of Quadrature Error,” *US Patent*, 0180908 A1, August 9, 2007.

[35] Mikko Saukoski, Lasse Aaltonen, Kari A. I. Halonen, “Zero-Rate Output and Quadrature Compensation in Vibratory MEMS Gyroscopes,” *IEEE Sensors Journal*, Vol. 7, No. 12, pp. 1639-1652, December 2007.

[36] William A. Clark and Roger T. Howe, “Surface Micromachined Z-Axis Vibratory Rate Gyroscope,” *Solid State Sensor and Actuator Workshop*, Hilton Head, USA, June 1996.

[37] Mark W. Weber, Robert B. Smith, “Quadrature Reduction in MEMS Gyro Devices Using Quad Steering Voltages,” *US Patent*, 7213458 B2, May 8, 2007.

[38] Bao Y. Yeh and Yung C. Liang, “Modeling and Compensation of Quadrature Error for Silicon MEMS Microgyroscope,” *IEEE PEDS-2001*, Indonesia.

[39] Ying W. Hsu, “Method of Canceling Quadrature Error in an Angular Rate Sensor,” *US Patent*, 6370937 B2, April 16, 2002.

[40] W. A. Clark, “Micromachined Z-Axis Vibratory Rate Gyroscope,” *US Patent*, 5992233, November 30, 1999.

[41] W. A. Clark, T. Juneau, R. T. Howe, “Micromachined Vibratory Rate Gyroscope,” *US Patent*, 6067858, May 30, 2000.

[42] W. A. Clark, T. N. Juneau, M. A. Lemkin, A. W. Roessig, “Dual-Mass Vibratory Rate Gyroscope With Suppressed Translational Acceleration Response and Quadrature Error Correction Capability,” *US Patent*, 6230563 B1, May 15, 2001.

[43] J. A. Geen, “A Path to Low Cost Gyroscopy,” *Solid State Sensor and Actuator Workshop Tech. Dig.*, Hilton Head, USA, pp. 51-54, June 1998.

[44] S. Niu, S. Gao, “ Analysis of Nonlinearities in Force-to-Voltage Conversion in Vibratory Microgyroscope,” *International Conference on Measuring Technology and Mechatronics Automation (ICMTMA)*, pp. 551-554, 2010.

[45] Kıvanç Azgın, “High Performance MEMS Gyroscopes,” *M.S. Thesis*, Middle East Technical University, February 2007

[46] Ajit Sharma, “CMOS Systems and Circuits for Sub-Degree Per Hour MEMS Gyroscopes,” *Ph.D. Dissertation*, Georgia Institute of Technology, December 2007.

[47] Analog Devices, “AD8608 Precision, Low Noise, CMOS, Rail-to-Rail, Input/Output Operational Amplifiers,” *Datasheet*, 2010.

[48] Analog Devices, “OPAMP Applications Handbook,” 2006.

[49] Analog Devices, “AD8222 Precision, Dual-Channel Instrumentation Amplifier,” *Datasheet*, 2010.

[50] Analog Devices, “AD630 Balanced Modulator/Demodulator,” *Datasheet*, 2004.

[51] Analog Devices, "AD8630 Zero Drift, Single-Supply, Rail-to-Rail Input/Output Operational Amplifier," *Datasheet*, 2010.

[52] S. E. Alper, A. Aydemir, and T. Akın, "Stepped-Etching for Preserving Critical Dimensions in Through-Wafer Deep Reactive Ion Etching of Thick Silicon," *Transducers 2009*, Denver, June 2009.

[53] W. H. Ko, J. T. Suminto, and G. J. Yeh, "Bonding Techniques for microsensors," Elsevier, 1985.

[54] IEEE Standard Specification Format Guide and Test Procedure for Single-Axis Interferometric Fiber Optic Gyros, *IEEE Std 1952-1997*, pp.65, September 1997.

[55] W. Geiger, J. Bartholomeyczik, U. Breng, W. Gutmann, M. Hafen, E. Handrich, M. Huber, A. Jäkle, U. Kempfer, H. Kopmann, J. Kunz, P. Leinfelder, R. Ohmberger, U. Probst, M. Ruf, G. Spahlinger, A. Rasch, J. Straub-Kalthoff, M. Stroda, K. Stumpf, C. Weber, M. Zimmermann, S. Zimmermann, "MEMS IMU for AHRS Applications," *Position Location and Navigation Symposium*, 2008.